LLE Review

UR
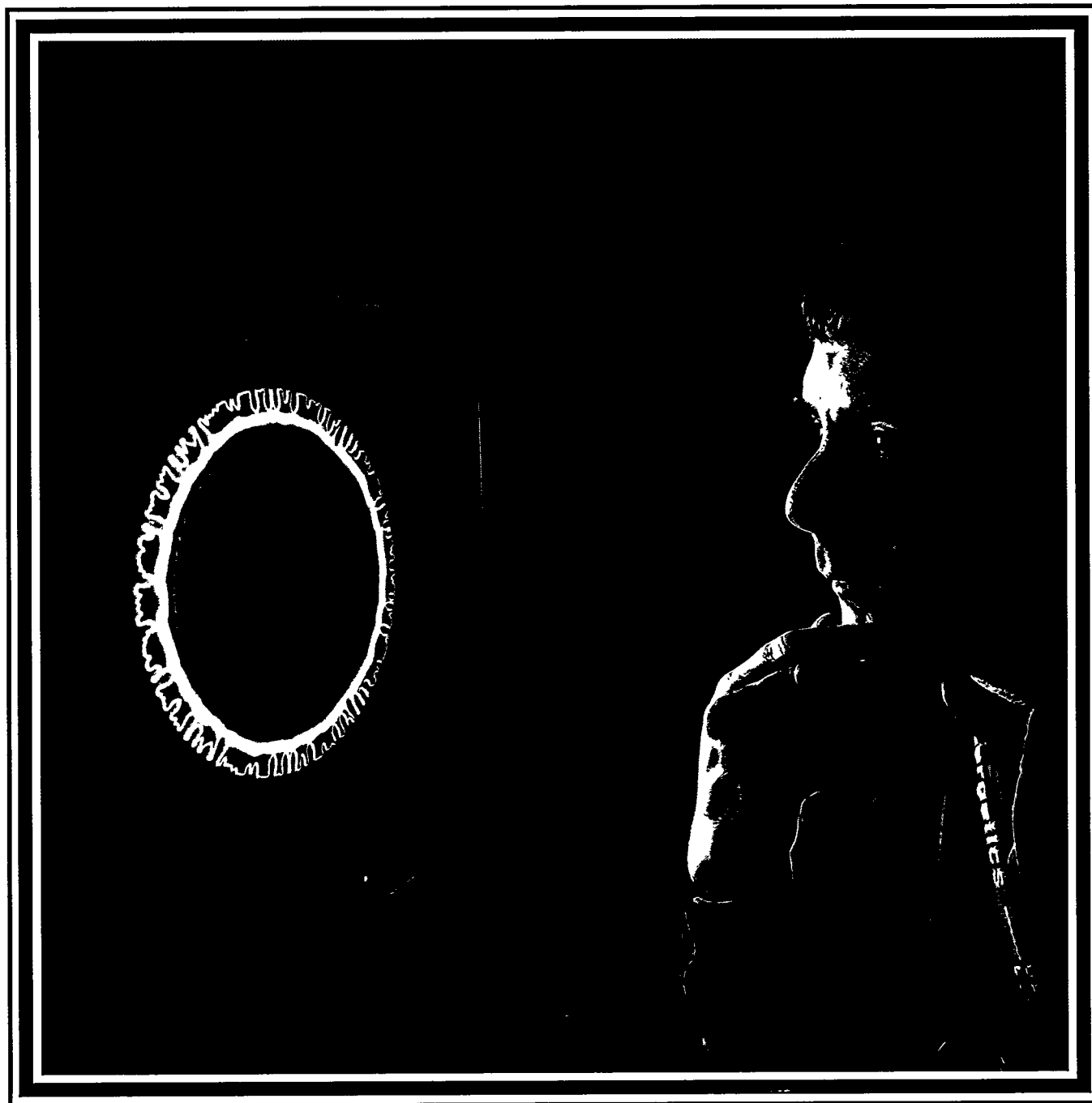LLE

Quarterly Report

About the Cover:

The cover photo shows Patrick McKenty, scientist at the Laboratory for Laser Energetics, viewing an image of the calculated density distribution from a two-dimensional hydrodynamics computer simulation of an imploding laser fusion pellet. Seen in the background is the COMPAQ Alpha multiprocessor computer used to perform the simulations. The article entitled "Analysis of a Direct-Drive Ignition Capsule Designed for the National Ignition Facility" (p. 181) describes the details of these model calculations.
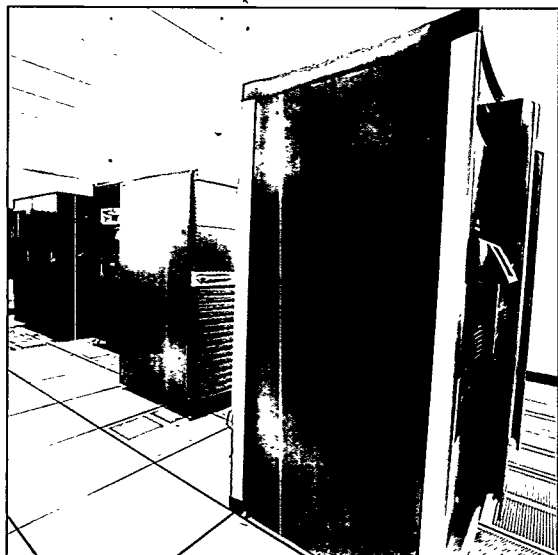
The high-speed computing facilities shown at left are used to accomplish one- and two-dimensional hydrocode simulations at LLE. From foreground (right) to background (left) are an SGI Origin 2000 multiprocessor computer, a COMPAQ Alpha multiprocessor computer, and an IBM tape-backup system.

For questions or comments, contact Frederic J. Marshall, *Editor*, Laboratory for Laser Energetics, 250 East River Road, Rochester, NY 14623-1299, (716) 275-2279.

Worldwide-Web Home Page: http://www.lle.rochester.edu/

DISCLAIMER

DISCLAIMER

Portions of this document may be illegible
in electronic image products. Images are
produced from the best available original
document.

LLE Review

UR
LLE

Quarterly Report

Contents

In Brief

This volume of the LLE Review, covering July–September 2000, begins with an article by T. R. Boehly, V. N. Goncharov, O. Gotchev, J. P. Knauer, D. D. Meyerhofer, D. Oron, S. P. Regan, Y. Srebro, W. Seka, D. Shvarts, S. Skupsky, and V. A. Smalyuk, who describe measurements of the effect of beam smoothing and pulse shape on imprinting. (Imprinting is defined as the imposition of pressure perturbations on the target by spatial variations in the laser intensity.) A principal result is the observation of reduced levels of imprint with the higher beam smoothing afforded by 1-THz smoothing by spectral dispersion (SSD).

Additional highlights of research presented in this issue are

- P. W. McKenty, V. N. Goncharov, R. P. J. Town, S. Skupsky, R. Betti, and R. L. McCrory describe calculations of directly driven ignition capsule performance on the National Ignition Facility (NIF). The authors detail how the various contributors to implosion disruption (laser imprint, power imbalance, and target roughness) affect target performance and final gain. The conclusions are obtained by examining the simulated target evolution with the two-dimensional hydrodynamics computer code *ORCHID*.

- D. D. Meyerhofer, J. A. Delettrez, R. Epstein, V. Yu. Glebov, V. N. Goncharov, R. L. Keck, R. L. McCrory, P. W. McKenty, F. J. Marshall, P. B. Radha, S. P. Regan, S. Roberts, W. Seka, S. Skupsky, V. A. Smalyuk, C. Sorce, C. Stoeckl, J. M. Soures, R. P. J. Town, B. Yaakobi, J. D. Zuegel, J. Frenje, C. K. Li, R. D. Petrasso, F. Séguin, K. Fletcher, S. Padalino, C. Freeman, N. Izumi, R. Lerche, T. W. Phillips, and T. C. Sangster describe the results of a series of direct-drive implosions of gas-fusion-fuel-filled plastic shells performed on the OMEGA laser system. The experiments include those performed with 1-THZ SSD and high-quality power balance.

- V. Yu. Glebov, D. D. Meyerhofer, C. Stoeckl, and J. D. Zuegel describe the technique of measuring secondary neutron yield (DT neutron yield from D_2-filled targets) using current-mode detectors (i.e., many detection events per unit time interval). They show that current-mode detectors can be configured to survey a much larger dynamic range than single-event neutron counters.

- V. A. Smalyuk, T. R. Boehly, L. S. Iwan, T. J. Kessler, J. P. Knauer, F. J. Marshall, D. D. Meyerhofer, C. Stoeckl, B. Yaakobi, and D. K. Bradley detail a method of measuring the positional dependence of x-ray self-absorption with filtered x-ray framing cameras. They show how compressed shell nonuniformities can be measured by carefully modeling the imaging system.

- This volume concludes with the LLE's Summer High School Research Program, the FY00 Laser Facility Report, and the National Laser Users' Facility News.

Frederic J. Marshall
Editor

Optical and Plasma Smoothing of Laser Imprinting in Targets Driven by Lasers with SSD Bandwidths up to 1 THz

Introduction

A key issue for inertial confinement fusion (ICF)[1-3] is the Rayleigh–Taylor (RT) hydrodynamic instability.[4,5] In direct-drive ICF, nonuniformities in the drive laser produce pressure variations that "imprint" perturbations into the target. Unstable RT growth can amplify these perturbations, resulting in sufficient distortion of the target shell to degrade implosion performance. As coronal plasma is formed around the target, a region of thermal conduction is produced where nonuniform energy deposition can be thermally smoothed[6-8] before perturbations reach the ablation surface. A mode of laser nonuniformity couples to (or seeds) a mode of hydrodynamic instability up to the time that sufficient plasma smoothing occurs, and then imprinting ceases.[8] The time to produce this plasma and decouple the laser nonuniformities from the unstable ablation region depends on the perturbation wavelength and the energy deposition rate, i.e., the laser pulse shape. Fast-rising pulses produce plasma more rapidly than slow-rising pulses and therefore cause imprinting over shorter times.[9] During the time that this plasma evolves, nonuniformities in the drive must be minimized. To do so, many ICF target designs employ laser-beam-smoothing techniques,[10] most of which are time dependent. These techniques are quite effective and have produced marked improvements in the performance of direct-drive targets.[11]

As a result of these smoothing effects, the amount of imprint experienced by a target depends on the temporal behavior of both the laser uniformity and the plasma evolution. This article describes measurements of the effect of beam smoothing and pulse shape on imprinting, and the results are used to demonstrate the dependence of imprinting on the plasma formation rate. It extends the measurements described in Ref. 9 to the higher smoothing rates of 1-THz smoothing by spectral dispersion (SSD).[10]

Laser imprinting begins when nonuniformities in the laser produce variations in the initial pressure, launching nonuniform shocks into the target. These shocks produce velocity perturbations in the target that distort the shock and ablation fronts. (Regions of higher intensity produce stronger shocks that propagate faster than those driven at lower intensities.) These distortions create lateral mass flow in the shock-compressed material that in turn creates differential pressures that perturb the acceleration profile at the ablation surface. The RT instability exponentially amplifies these acceleration and velocity perturbations, producing additional mass perturbations in the target. (This redistribution of mass can be responsible for degrading the target performance and is observable in many experiments.) In addition to the above, effects such as dielectric breakdown in the target and laser filamentation[12] may create target perturbations that can seed the RT instability.

As the interaction proceeds, more plasma is formed and the laser light is absorbed at increasing distances from the ablation surface. The nonuniformities in intensity continue to drive acceleration perturbations at the ablation front, but thermal smoothing in the intervening plasma (between the absorption and ablation regions) reduces the magnitude of the pressure variations that reach the ablation surface. Eventually, the size of this conduction zone is sufficient to completely smooth the pressure perturbations, and imprinting stops. The calculated condition for the cessation of imprinting is[8]

$$kd_c \sim 2, \tag{1}$$

where k is the wave number of the imprinted perturbation and d_c is the average distance between the absorption region and the ablation surface.[13] In this article, the effect of the plasma formation rate and beam smoothing on imprinting is experimentally studied and found to be in good agreement with the condition of Eq. (1).

Experiments on the OMEGA laser system[14] measured an equivalent surface roughness of imprinting in planar targets using the growth of preimposed modulations for calibration.[9] This surface roughness is defined as the mass perturbation that produces similar resultant amplitudes after the linear RT growth phase.[15] Using this measure, the imprinting produced by different temporal pulse shapes and beam-smoothing tech-

niques is compared. Rapidly rising (~100 ps/decade) pulses produce less imprint than slowly rising pulses (~2.5-ns rise time) when no temporal beam smoothing is employed. Furthermore, the effect of SSD is less pronounced for these rapid-rise pulses. These are consistent with plasma smoothing[6–8] by thermal conduction and the intensity-dependent rate of plasma production.[9]

Simulations[15,16] that investigated imprinting have indicated that, for a given laser wavelength, the imprint efficiency (equivalent imprint level per fractional laser nonuniformity) depends linearly on the drive nonuniformity (i.e., $\delta m \propto \delta I/I$) for the intensities relevant to direct-drive ICF. The duration of imprinting, however, depends on the time required to produce a sufficiently sized plasma [Eq. (1)] to completely smooth pressure variations created by laser nonuniformities. As the thermal conduction region grows, longer wavelengths can be smoothed; thus, for each wavelength the duration of laser imprinting (and therefore its total magnitude) depends on the time required to develop a sufficiently large conduction zone. The plasma formation rate therefore affects the wavelength dispersion of imprinting. For a given wavelength of interest, imprinting ultimately ceases when the conduction region grows to a sizable fraction of the wavelength, satisfying Eq. (1). Thus, in order to reduce imprinting, it is also important that significant optical beam smoothing occurs while this plasma is forming. The experiments described below demonstrate the interplay between these two effects.

Experiments

In these experiments, six overlapping UV OMEGA beams irradiated 20-μm-thick CH (ρ = 1.05 g/cm^3) targets with preimposed modulations at 30- and 60-μm wavelengths. These wavelengths correspond to ℓ modes of 50 and 100 on millimeter-sized targets, which are important for direct-drive ICF on OMEGA. Experiments were performed with two laser temporal pulse shapes: a 3-ns square pulse and a 2.5-ns ramp pulse. The square pulse had a rise time of 100 ps per decade of intensity and an intensity of 2×10^{14} W/cm^2. The ramp pulse rose linearly from ~10^{13} to 2.5×10^{14} W/cm^2 in 2.5 ns after a 100-ps rise to ~10^{13} W/cm^2. For each pulse shape, experiments were performed with and without single-cycle, 2-D SSD beam smoothing at 0.2- and 1.0-THz bandwidths with modulation frequencies of 3×3 GHz and 1.6×11 GHz, respectively. In some cases, polarization smoothing (PS)[17] was added by using wedged birefringent plates.[18]

The driven targets were radiographed with x rays produced by a uranium backlighter irradiated at 2×10^{14} W/cm^2. X rays

transmitted through the target and a 3-μm-thick Al blast shield were imaged by a framing camera with 8-μm pinholes filtered with 20 μm of Be and 6 μm of Al.[19] This filtration provided highest sensitivity at 1.3 keV and a resolution of at least 12 μm.

Since the initial perturbations produced by the laser are quite small, it is difficult to directly measure laser imprint. Measurements often rely on RT growth to produce detectable modulations in the target areal density. Relying on this non-linear process as an "amplifier" makes it difficult to determine the initial amplitude of the seed, i.e., the amplitude of imprinting. The spectrum of laser nonuniformities is determined by the interference produced by the distributed phase plates (DPP's)[20] and the smoothing produced by SSD. These spectra were measured for a variety of conditions.[18,21] For the DPP-only case, the power spectrum of nonuniformities peaks at about 6 μm. SSD begins smoothing the shortest wavelengths, almost immediately (~25 ps) producing a spectrum that first flattens, then monotonically falls with frequency. These nonuniformities produce target perturbations that evolve due to dispersion in the RT growth and saturation mechanisms. As a result, the perturbation spectra for the various uniformity conditions are similar because the competing effects preferentially amplify the mid-frequencies (i.e., wavelengths from ~20 to 100 μm). The primary difference is the amplitude at a given time. Smoother irradiation profiles eventually produce features similar (albeit at later times) to those with higher irradiation nonuniformities. This evolution was shown for various uniformities in Refs. 18 and 22 and discussed at length in Ref. 23. As the spectra evolve, their peak moves to longer wavelengths. For these measurement times the spectral peak typically reaches 30 μm but seldom reaches 60 μm. These wavelengths are therefore of great interest because they can be most damaging to the target.

Low-amplitude, single-mode, preimposed target perturbations (at 30 and 60 μm) were used as a "control" for calibration, from which the initial amplitude of laser imprinting was determined. The basis of this calibration is that, in the linear regime of RT instability, imprinted perturbations grow at the same rate as preimposed modulations.[9,15,24] Although imprinting also produces velocity and acceleration perturbations, it is useful to assign it an equivalent surface roughness (mass modulation) to imprinting.[15]

Imprint was measured in this work by the method illustrated in Fig. 84.1(a), which shows a plot of the amplitude of single-mode target perturbations predicted by the 2-D code ORCHID.[25] The dotted curve shows the amplitude evolution

in a target having a 60-μm, single-mode mass perturbation and driven with a spatially perfect laser. The solid curve shows a similar evolution in an initially perfect target (no perturbations) driven by a laser having a single-mode intensity modulation (again with 60-μm wavelength). The solid curve starts at zero amplitude and rises as imprinting begins. At ~400 ps, RT growth begins and the evolution of imprint amplitude is parallel to the dotted curve. The RT instability amplifies both perturbations, imposed or imprinted, in the same manner. The equivalent surface roughness of imprinting can be deduced by extrapolating (dashed curve) the temporal evolution of the imprinted amplitudes (solid curve) back to $t = 0$ using the behavior of the preimposed mode (dotted curve). In the linear regime, modes of the same wavelength grow at the same rate, and the ratio of amplitudes for these two modes remains constant. Thus, an equivalent initial amplitude for imprinting can be deduced by comparing (after some RT growth) the amplitude of the imprinted mode to a preimposed mode of known initial value. Figure 84.1(b) shows the result of an experiment[23] where a target with a preimposed 60-μm perturbation was driven by a laser with 0.2-THz SSD without polarization smoothing. The upper two curves show the amplitude of the imposed modulations in two different experiments: one with an initial amplitude of 1250 Å and the other with 500 Å. The lower curve is the amplitude of the imprinted modes (at the same wavelength) for six different experiments. All experiments were performed under similar laser and target conditions.[23,26] The points at the lower left have large error bars because the signal is very near the noise level.

Since the imposed and imprinted perturbations grow at the same rate, the upper two curves in Fig. 84.1(b) are parallel to the lower curve. The ratio of the amplitudes for the two

preimposed modes (initial amplitudes of 1250 Å and 500 Å) is constant and equal to their ratio at $t = 0$, showing that the RT growth is in the linear regime. This method requires that, for the modes of interest, the RT instability remain in the linear regime and that they experience no saturation or nonlinear effects.[27] Saturation of RT growth is discussed at length in Refs. 23 and 26, where it was shown that at $\lambda = 60~\mu$m, both the single-mode and the imprinted perturbations behaved linearly for the experimental conditions and observation times described in this article. For this experiment the 30-μm-wavelength imprinting data was measured before the onset of its saturation as observed in Refs. 23 and 26.

The amplitude of the equivalent surface roughness for a specific wave number is defined as[15]

$$A_{eq}(k,0) = \left[A_{imprint}(k,t)/A_{pre}(k,t)\right]A_{pre}(k,0), \quad (2)$$

where $A_{imprint}(k,t)$ is the measured amplitude of the imprinted features, $A_{pre}(k,t)$ is the measured amplitude of the preimposed modulation, and $A_{pre}(0)$ is the known initial amplitude of the preimposed modulation. A measure of imprint efficiency,[15] which can be readily compared to simulations, is $\eta_i(k) = A_{eq}(k,0)/(\delta I/I)$, where $\delta I/I$ is the measured fractional irradiation nonuniformity at the same wavelength.

The amplitudes of the perturbations are obtained by Fourier analysis of the x-ray radiographed images.[19] The Fourier amplitude of the imprinted features at a given wavelength is the rms of all mode amplitudes at that wavelength, i.e., those modes at a given radius (centered at zero spatial frequency) in spatial-frequency space (the contribution of the preimposed

(a)

(b)
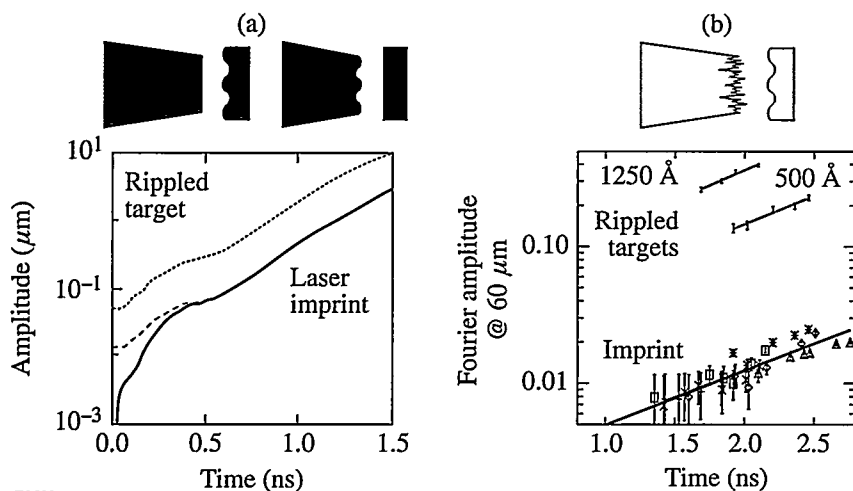
Figure 84.1

Derivation of equivalent surface finish. (a) Simulations of the perturbation amplitude evolution: The dotted curve is a 60-μm, single-mode mass perturbation driven with a spatially perfect laser. The solid curve shows the similar evolution in an initially perfect target (no perturbations) driven by a laser having a 60-μm, single-mode intensity modulation. The equivalent surface finish is defined as the point where the dashed curve intercepts $t = 0$. (b) Experimental results showing the measured amplitudes (optical depth) for imprinted (lower set) and imposed modulations (upper two sets). All are at 60-μm wavelength.

E9502

modulation is not included). The features of interest at 30 μm and 60 μm are easily observed by the camera, which has ~15-μm resolution.

The preimposed single-mode modulations appear as localized features along a single axis in the Fourier plane and at the spatial frequency of their modulation. The time-dependent amplitude of the preimposed mode is obtained by subtracting (in quadrature) the rms amplitude of the imprinted modes at the same time. The analysis box is ~300 μm in the target plane; thus, in Fourier space, the pixel size is ~3.3 mm^{-1}. (The box size is optimized to ensure that all the power in the preimposed mode is contained in a single pixel in each Fourier half-plane.)

For these experiments a variety of beam-smoothing techniques were used. A single-beam laser with a DPP and no SSD provides a static speckle pattern with ~80% to 100% nonuniformity in wavelengths from 2 μm to 250 μm.[21] The speckle results from the interference of many beamlets produced by diffraction in the DPP optic. The speckle pattern is statistical in nature with a sufficiently short correlation length that multiple overlapped beams can be treated as statistically independent patterns. Thus six-beam irradiation reduces this nonuniformity to $\sqrt{6}$ times lower than the single-beam value. Additional beam smoothing is provided by SSD, which, by introducing bandwidth onto the laser, produces a statistically independent speckle pattern every $\Delta t = t_c$, where $t_c \sim 1/\Delta v$ is the correlation time and Δv is the UV laser bandwidth.[10] SSD does not reduce nonuniformities instantaneously, rather the time-averaged rms uniformity is reduced by $\sqrt{t_c/\langle t \rangle}$, where $\langle t \rangle$ is the averaging time. Thus, the drive uniformity is time dependent and varies with the amount of bandwidth applied to the laser. These experiments were performed with one of two laser bandwidths, either $\Delta v = 0.2$ THz$_{UV}$ or 1.0 THz$_{UV}$. (All experiments with SSD used two-dimensional SSD.) In the former case the IR bandwidths were 1.25 Å × 1.75 Å and in the latter case 1.6 Å × 11 Å. In some cases, polarization smoothing (PS) using birefringent wedges[18] was added to the drive beams. Polarization smoothing provides an instantaneous $\sqrt{2}$ reduction in nonuniformity by dividing each beam into two orthogonal polarizations that are separated by 80 μm in the target plane.[18]

Figure 84.2 shows the equivalent surface roughness (in μm) of imprinting measured at 60-μm wavelength for a series of shots that used a 3-ns square pulse with four different smoothing conditions (all with similar drive intensities). The temporal axis is the time at which each measurement was taken. These data separate into distinct sets associated with

each uniformity condition and are constant in time. Both these observations are expected and confirm the utility of this technique. When the growth of the imprinted features is in the linear regime, their amplitude should remain a constant fraction of that of the preimposed mode, leading to a constant inferred surface roughness. This quantity's dependence on the initial uniformity produced by the various beam-smoothing techniques indicates the sensitivity of the method. For example, the addition of polarization smoothing (diamonds) to the 0.2-THz SSD experiments (open squares) reduced the equivalent surface roughness by the expected factor of $\sqrt{2}$. Similarly, the increase in the SSD bandwidth from 0.2 (open squares) to 1.0 (x's) THz without polarization smoothing reduced the equivalent surface roughness by ~0.60. This is the reduction expected from models of the optical smoothing by SSD (see below). The results for all conditions are listed in Table 84.I.

E10031
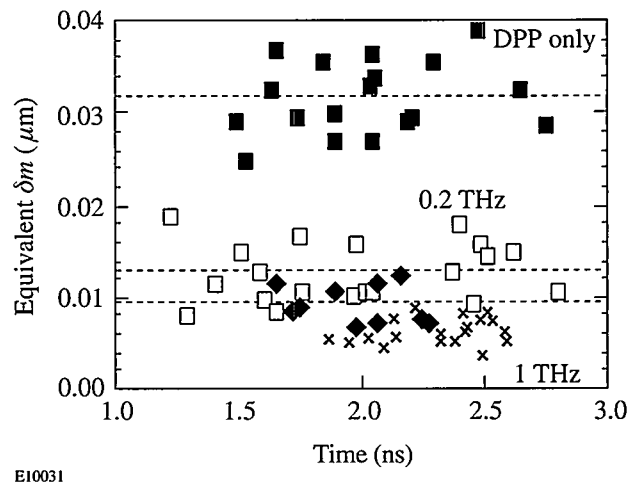
Figure 84.2

The equivalent surface roughness (in μm) at 60-μm wavelength derived from planar targets driven by laser beams having a 3-ns square pulse and four types of beam smoothing applied: DPP only (solid squares), DPP + 0.2-THz SSD (open squares), DPP + 0.2-THz SSD + PS (diamonds), and DPP + 1-THz SSD (x's). The data segregate according to the laser nonuniformity with the total amount of imprinting decreasing with increased beam smoothing.[9]

The effect of pulse shape on imprinting was studied by repeating these measurements with a slowly rising pulse, i.e., with a ~2.5-ns rise to the maximum intensity. Figure 84.3 shows the equivalent surface roughness as a function of time for the two pulse shapes, each with and without 0.2-THz SSD. Again the data group according to laser conditions (pulse shape or SSD) and exhibit an approximately constant value over a considerable time.

These data show that without SSD the ramp pulse (solid triangles) produces about 50% more imprinting (rougher equivalent surface) than the square pulse (solid squares). They also indicate that 0.2-THz SSD produces a greater reduction of imprinting (~2.5×) on the ramp pulse (open triangles) than for the factor of 2.2 observed for the square pulse (open squares). Similar experiments were performed using preimposed modulations with $\lambda = 30 \ \mu$m.

The imprint efficiency was calculated for the experiments without SSD using the single-beam irradiation nonuniformities reported in Ref. 21. The uniformity results were scaled by the

differences in analysis boxes between the x-ray radiography ($L = 300 \ \mu$m; $\Delta k = 0.021 \ \mu$m^{-1}) and the optical experiments ($L = 440 \ \mu$m; $\Delta k = 0.0143 \ \mu$m^{-1}). In addition, the values obtained in Ref. 21 were reduced by $\sqrt{6}$ since these experiments utilized six overlapped beams. Thus, $\delta I/I$ was 0.0068 for 30 μm and 0.0049 for 60 μm. Lastly, a factor of 2 was included to relate the complex amplitude for $\delta I/I$ to the equivalent surface roughness, which was normalized using a real (cosine) function. The measured imprint efficiencies are shown in Table 84.I. Since the SSD produ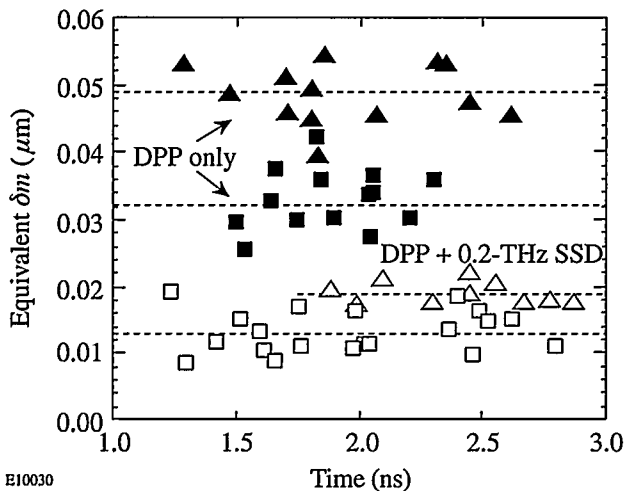ces time-varying uniformity, it is difficult to assign a single number to the uniformity; therefore, the imprint efficiency is not quoted for those cases. The effect of SSD will be discussed below.

As discussed above, the duration of imprinting depends on the time required to produce sufficient plasma atmosphere to enable smoothing. As a result, the ramp pulse imprints for a longer duration than the square pulse because it delivers energy at a slower rate and therefore generates the smoothing plasma more slowly. Thus the ramp pulse will imprint for a longer duration, leading to a higher equivalent roughness. The imprint efficiencies measured here are lower, as expected, than those observed by Glendinning et al.[24,28] using an even slower rise and lower-intensity ramp pulse.

Simulations of Imprint and Plasma Smoothing

The experiments were simulated with the 2-D hydrodynamics code ORCHID to determine the predicted imprint efficiency and the effects of plasma smoothing. The imprint efficiencies were calculated by imposing a single-mode nonuniformity in the laser irradiation. The evolution of the resulting perturbations was compared to that of preimposed mass perturbations at the same wavelength. The experimental temporal pulse shapes were used in the simulations. The simulation results shown in Table 84.I are in reasonable

Figure 84.3
The deduced equivalent surface roughness of the imprinted features (at 60 μm) for two pulse shapes: 3-ns square (squares) and ramp (triangles). These data show that for the same laser nonuniformity, a ramp pulse produces more imprinting. The open and solid symbols correspond, respectively, to each of the pulses with and without 2-D SSD. They indicate that the effect of SSD is greater for the ramp pulse.[9]

Table 84.I: Equivalent surface roughness and imprint efficiency for various conditions.

Pulse-Shape Uniformity	Equivalent Surface Roughness (μm)		Imprint Efficiency: $(\delta m/\rho)/(\delta I/I)$ (μm)			
			Experiment		Simulation	
	60 μm	30 μm	60 μm	30 μm	60 μm	30 μm
Square (no SSD)	0.032±005	0.022±004	3.3±0.4	1.6±0.3	1.7	1.1
Ramp (no SSD)	0.049±008	0.023±005	5.0±0.6	1.7±0.4	3.1	2.3
Square (0.2-THz SSD)	0.013±003	0.010±003				
Ramp (0.2-THz SSD)	0.017±005	0.011±004				
Square (1-THz SSD)	0.009±0.0018	0.0044±0.0015				
Ramp (1-THz SSD)	0.0105±0.0022	0.0054±0.0019				

agreement with the measured values. Similar imprint efficiencies were calculated with the 2-D hydrodynamics code *LEEOR*.[29] The 2-D simulations underestimate the imprint efficiency at 60 μm, similar to the observations of Glendinning *et al.*[24,28] For the 30-μm perturbations, the simulations also underestimate the square-pulse data but overestimate the ramp-pulse data.

The inherent real surface roughness of these foils (transverse to the imposed modulations) was measured to be less than 1% of the imposed mode and, therefore, did not contribute significantly to the error in the measurements of either the imprinted or the imposed modes. The measured signal for the preimposed mode also has a contribution from the imprinted signal at that distinct mode. Since the relative phase of these two signals is arbitrary, the resultant signal can vary significantly when the imprint is a sizable fraction of the preimposed mode. To minimize this effect, the imprinted modes were kept below 30% of the imposed mode by increasing the amplitude of the imposed modes on shots without SSD. Most experiments were performed with the imprint between 0.1 and 0.25 of the imposed mode. This represented a trade-off between the noises from either too low a signal in the imprinted modes or that affecting determination of the imposed mode, while keeping both signals below the saturation limits.

The effect of plasma formation rate on thermal smoothing of nonuniform energy deposition was investigated using *ORCHID*. Figure 84.4 shows the calculated amplitude of pressure pertur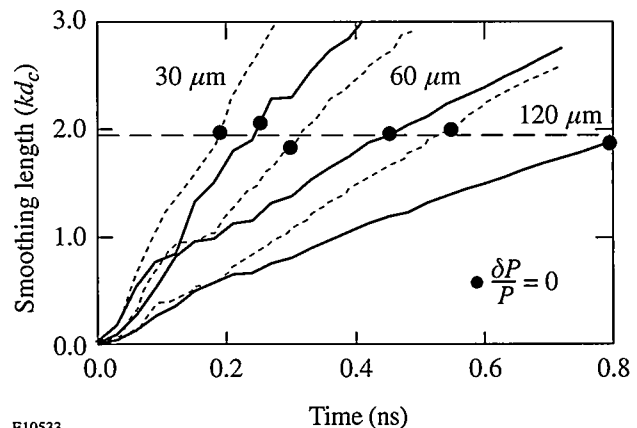bations (solid curves) at the ablation surface as a function of time for two cases: a ramp pulse and a square pulse, both without SSD. In these simulations a static 60-μm-wavelength, 5% spatial-intensity modulation was imposed on the irradiation profile. The pressure perturbations that reach the ablation surface diminish as the plasma expands. Note that for the ramp pulse, the smoothing rate is slower and the perturbations persist for a longer period. The temporal evolution (dashed curves) of the normalized conduction zone (kd_c) for the two pulse shapes is also shown. This is defined as the distance between the ablation surface and the mean of the energy deposition profile as weighted by a diffusion length e^{-kz} and is normalized to the wave number.[13] (The energy deposition profile must also be accounted for since considerable smoothing can take place in the plasma region outside the critical surface.) Imprinting ceases when pressure perturbations at the ablation surface are reduced to negligible levels. Figure 84.4 shows that for both pulse shapes this occurs when $kd_c \sim 2$, providing a measure of the decoupling time for the case of constant uniformity (no SSD). This analysis has also been applied to other wavelengths and both pulse shapes, and found to confirm that $kd_c \sim 2$ is the applicable condition. Figure 84.5 shows the simulations of the normalized smoothing length (kd_c) as a function of time for the square (dashed) and ramp (solid) pulses for three wavelengths: 30, 60, and 120 μm. The solid points indicated the time at which the modulations in ablation pressure diminish to zero for each case. This occurs for $kd_c \sim 2$ for all six cases. As the plasma evolves, shorter wavelengths are smoothed sooner than longer wavelengths; this in part determines the dispersion in wavelength of the imprint efficiency. Thus, for the broad spectrum of laser

Figure 84.4
The calculated amplitude of 60-μm perturbations (solid curves) in the pressure at the ablation surface as a function of time. The size of the conduction zone (dashed curves) as a function of time in CH targets driven by the square and ramp pulses. These graphs show that, for 60-μm perturbations, decoupling occurs at 290 ps for the square pulse and 450 ps for the ramp pulse.[9]

Figure 84.5
Simulations of the normalized smoothing length (kd_c) versus time for square (dashed) and ramp (solid) pulses. The points indicate the time at which the modulations in ablation pressure diminish to zero. Perturbations with wavelengths of 30, 60, and 120 μm are all smoothed when $kd_c \sim 2$.

nonuniformities present in laser speckle, the short-wavelength modes are smoothed first. These modes also have faster growth rates and experience saturation sooner than longer-wavelength modes. In contrast, the longer-wavelength modes are smoothed less, but also grow at slower rates. As a result, intermediate wavelengths (ℓ modes of 50 to 100 on millimeter-sized targets) become dominant and, therefore, are of most concern for target stability. The calculated decoupling times for 60-μm wavelengths were found to be 290 and 450 ps for the square and ramp pulses, respectively. For 30-μm wavelengths, the respective times were 190 and 270 ps.
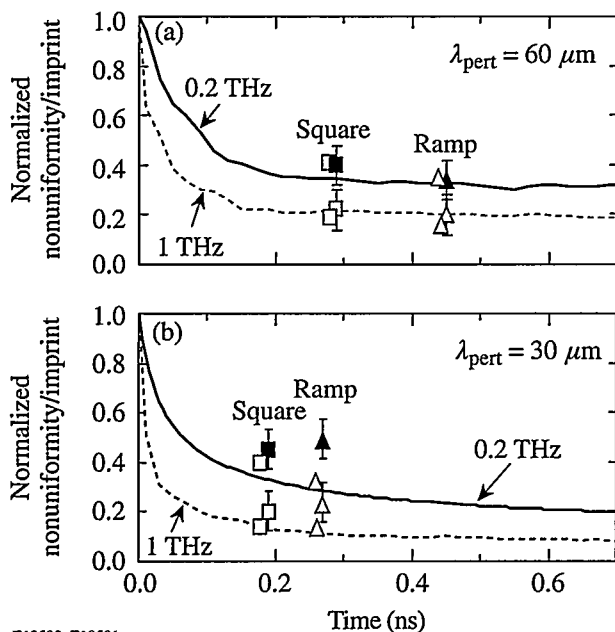
Decoupling and the Dynamics of Smoothing

Plasma smoothing and decoupling of imprinted perturbations are confirmed experimentally by analyzing experiments with time-dependent beam smoothing. By matching the observed reduction of imprinting to the smoothing rate of SSD, the effect of thermal smoothing by the plasma atmosphere is observed. Figure 84.6 shows the imprint reduction [at (a) 60-μm and (b) 30-μm wavelengths] as a function of time for SSD bandwidths of 0.2 (solid points) and 1.0 (shaded points) THz$_{UV}$. In each, the curves are the irradiation nonuniformity

Figure 84.6
The normalized nonuniformity [(a) for 60 μm and (b) for 30 μm] as predicted by the optical model (curves) with the measured reductions in imprint for 0.2 THz (solid points) and 1 THz (shaded points) for square (squares) and ramp (triangles) pulse shapes. The predictions by *ORCHID* are shown as open points (similarly identified).

(normalized to that at $t = 0$) predicted by an optical model[21] (basically a $1/\sqrt{t\Delta\nu}$ dependence). The points are the measurements of the reduction in imprinting due to SSD. This reduction is calculated by normalizing the SSD data to measurements without SSD. Reference 21 demonstrated that the optical model accurately predicts the smoothing rate and the ultimate uniformity achieved with 0.2-THz SSD (solid curve). It is expected that it represents the performance of 1.0 THz (dashed curve) as well. The imprint data are plotted at the calculated decoupling times described above. The square-pulse data (squares) are shown for 0.2 THz (solid points) and 1.0 THz (shaded points). The ramp-pulse data (triangles) are similarly coded for SSD. The predictions (open symbols) are shown slightly displaced in time for clarity. Figure 84.6 shows that (1) for 60 μm the calculated decoupling times are consistent with the optical data and (2) the hydrocode models the effect of SSD and the plasma production rate (pulse shape) quite well. The 30-μm data for the ramp pulse are above both the optical smoothing rate and the hydrocode results, i.e., the reductions are less than expected. This may be caused by the imprinting measurement for the no-SSD, 30-μm case (denominator for reduction calculation) being too low. A possible mechanism for error in the measured imprint is the onset of saturation in the imprinted (3-D) modes that has not yet affected the preimposed (2-D) modes. Reference 23 showed that for these conditions the 30-μm perturbations can experience saturation if the amplitudes are high enough. Furthermore, the ramp pulse, because of its late decoupling time, imprints more readily and therefore would be most susceptible to saturation. Unfortunately, the spread in data does not allow its temporal trend to be discerned with precision and saturation cannot be easily detected.

Conclusion

Using preimposed modulations on planar targets to calibrate imprinting amplitudes, this work has confirmed imprinting's expected dependence on drive-laser nonuniformity, showing the utility of the equivalent-surface technique. It has demonstrated that imprinting depends on the temporal shape of the drive laser. This occurs because thermal smoothing in the coronal plasma ultimately limits the duration of imprinting and therefore its total amplitude. Once there is sufficient plasma, the pressure perturbations no longer reach the unstable ablation surface and imprinting stops. Steeply rising pulses produce plasma more rapidly than slowly rising pulses and therefore produce less imprinting. The simulations of the static cases (DPP's only) show behavior that is consistent with the decoupling times predicted for these conditions. Moreover, using the dynamic case of 2-D SSD, the improvements in uniformity inferred by measuring imprint are consis-

tent with both the measured rate of smoothing by SSD and the decoupling times predicted by the hydrocodes; they also verify the predictions of Eq. (1). The increase in laser bandwidth to 1 THz has produced reductions in the imprint level that agree with expected performance. These results provide confidence in our ability to model and control imprinting in direct-drive ICF targets.

ACKNOWLEDGMENT

REFERENCES

1. J. Nuckolls *et al.*, Nature **239**, 139 (1972).

2. J. D. Lindl, Phys. Plasmas **2**, 3933 (1995).

3. S. E. Bodner, D. G. Colombant, J. H. Gardner, R. H. Lehmberg, S. P. Obenschain, L. Phillips, A. J. Schmitt, J. D. Sethian, R. L. McCrory, W. Seka, C. P. Verdon, J. P. Knauer, B. B. Afeyan, and H. T. Powell, Phys. Plasmas **5**, 1901 (1998).

4. Lord Rayleigh, Proc. London Math Soc. **XIV**, 170 (1883).

5. G. Taylor, Proc. R. Soc. London Ser. A **201**, 192 (1950).

6. K. A. Brueckner and S. Jorna, Rev. Mod. Phys. **46**, 325 (1974).

7. S. E. Bodner, Phys. Rev. Lett. **33**, 761 (1974).

8. V. N. Goncharov, S. Skupsky, T. R. Boehly, J. P. Knauer, P. McKenty, V. A. Smalyuk, R. P. J. Town, O. V. Gotchev, R. Betti, and D. D. Meyerhofer, Phys. Plasmas **7**, 2062 (2000).

9. T. R. Boehly, V. N. Goncharov, O. Gotchev, J. P. Knauer, D. D. Meyerhofer, D. Oron, S. P. Regan, Y. Srebro, W. Seka, D. Shvarts, S. Skupsky, and V. A. Smalyuk, "The Effect of Plasma Formation Rate and Beam Smoothing on Laser Imprinting," submitted to Physical Review Letters.

10. S. Skupsky and R. S. Craxton, Phys. Plasmas **6**, 2157 (1999).

11. D. D. Meyerhofer, J. A. Delettrez, R. Epstein, V. Yu. Glebov, R. L. Keck, R. L. McCrory, P. W. McKenty, F. J. Marshall, P. B. Radha, S. P. Regan, W. Seka, S. Skupsky, V. A. Smalyuk, J. M. Soures, C. Stoeckl, R. P. J. Town, B. Yaakobi, R. D. Petrasso, J. A. Frenje, D. G. Hicks, F. H. Séguin, C. K. Li, S. Haan, S. P. Hatchett, N. Izumi, R. Lerche, T. C. Sangster, and T. W. Phillips, "Core Density and Temperature Conditions and Fuel–Pusher Mix in Direct-Drive ICF Implosions," to be published in Physics of Plasmas.

12. H. A. Rose and D. F. DuBois, Phys. Fluids B **5**, 3337 (1993).

13. H. Azechi *et al.*, Phys. Plasmas **4**, 4079 (1997).

14. T. R. Boehly, D. L. Brown, R. S. Craxton, R. L. Keck, J. P. Knauer, J. H. Kelly, T. J. Kessler, S. A. Kumpan, S. J. Loucks, S. A. Letzring, F. J. Marshall, R. L. McCrory, S. F. B. Morse, W. Seka, J. M. Soures, and C. P. Verdon, Opt. Commun. **133**, 495 (1997).

15. S. V. Weber, S. G. Glendinning, D. H. Kalantar, M. H. Key, B. A. Remington, J. E. Rothenberg, E. Wolfrum, C. P. Verdon, and J. P. Knauer, Phys. Plasmas **4**, 1978 (1997).

16. R. J. Taylor *et al.*, Phys. Rev. Lett. **79**, 1861 (1997).

17. Y. Kato, unpublished notes from work at LLE, 1984.

18. T. R. Boehly, V. A. Smalyuk, D. D. Meyerhofer, J. P. Knauer, D. K. Bradley, R. S. Craxton, M. J. Guardalben, S. Skupsky, and T. J. Kessler, J. Appl. Phys. **85**, 3444 (1999).

19. V. A. Smalyuk, T. R. Boehly, D. K. Bradley, J. P. Knauer, and D. D. Meyerhofer, Rev. Sci. Instrum. **70**, 647 (1999).

20. Y. Lin, T. J. Kessler, and G. N. Lawrence, Opt. Lett. **20**, 764 (1995).

21. S. P. Regan, J. A. Marozas, J. H. Kelly, T. R. Boehly, W. R. Donaldson, P. A. Jaanimagi, R. L. Keck, T. J. Kessler, D. D. Meyerhofer, W. Seka, S. Skupsky, and V. A. Smalyuk, J. Opt. Soc. Am. B **17**, 1483 (2000).

22. T. R. Boehly, R. L. McCrory, C. P. Verdon, W. Seka, S. J. Loucks, A. Babushkin, R. E. Bahr, R. Boni, D. K. Bradley, R. S. Craxton, J. A. Delettrez, W. R. Donaldson, R. Epstein, D. Harding, P. A. Jaanimagi, S. D. Jacobs, K. Kearney, R. L. Keck, J. H. Kelly, T. J. Kessler, R. L. Kremens, J. P. Knauer, D. J. Lonobile, L. D. Lund, F. J. Marshall, P. W. McKenty, D. D. Meyerhofer, S. F. B. Morse, A. Okishev, S. Papernov, G. Pien, T. Safford, J. D. Schnittman, R. Short, M. J. Shoup III, M. Skeldon, S. Skupsky, A. W. Schmid, V. A. Smalyuk, D. J. Smith, J. M. Soures, M. Wittman, and B. Yaakobi, Fusion Eng. Des. **44**, 35 (1999).

23. V. A. Smalyuk, T. R. Boehly, D. K. Bradley, V. N. Goncharov, J. A. Delettrez, J. P. Knauer, D. D. Meyerhofer, D. Oron, D. Shvarts, Y. Srebro, and R. P. J. Town, Phys. Plasmas **6**, 4022 (1999).

24. S. G. Glendinning, S. N. Dixit, B. A. Hammel, D. H. Kalantar, M. H. Key, J. D. Kilkenny, J. P. Knauer, D. M. Pennington, B. A. Remington, R. J. Wallace, and S. V. Weber, Phys. Rev. E **54**, 4473 (1996).

25. R. L. McCrory and C. P. Verdon, in *Inertial Confinement Fusion*, edited by A. Caruso and E. Sindoni (Editrice Compositori, Bologna, Italy, 1989), pp. 83–124.

26. V. A. Smalyuk, T. R. Boehly, D. K. Bradley, V. N. Goncharov, J. A. Delettrez, J. P. Knauer, D. D. Meyerhofer, D. Oron, and D. Shvarts, Phys. Rev. Lett. **81**, 5342 (1998).

27. S. W. Haan, Phys. Rev. A **39**, 5812 (1989).

28. S. G. Glendinning, S. N. Dixit, B. A. Hammel, D. H. Kalantar, M. H. Key, J. D. Kilkenny, J. P. Knauer, D. M. Pennington, B. A. Remington, J. Rothenberg, R. J. Wallace, and S. V. Weber, Phys. Rev. Lett. **80**, 1904 (1998).

29. D. Shvarts, U. Alon, D. Ofer, R. L. McCrory, and C. P. Verdon, Phys. Plasmas **2**, 2465 (1995).

Analysis of a Direct-Drive Ignition Capsule Designed for the National Ignition Facility

Introduction

One of the primary missions of the National Ignition Facility[1] (NIF) is to achieve fusion ignition and moderate gain by means of inertial confinement fusion (ICF). A typical ICF experiment involves the implosion of a small spherical capsule containing deuterium–tritium (DT) fuel using high-power laser light. The energy is absorbed in a thin, outer region of the capsule, which quickly heats and ablates, expanding outward and accelerating the remainder of the capsule inward, compressing the contained DT fuel to ignition conditions. The implosion can be tailored to give a number of assembled fuel configurations of which the most energy efficient[2] is isobaric with a central high-temperature hot spot surrounding a low-temperature main fuel layer. The central hot spot initiates the fusion reaction, which leads to a burn wave propagating into the main fuel layer. For direct-drive target designs two main effects can prevent the correct assembly of the fuel: (1) preheat of the fuel[3] and (2) hydrodynamic instabilities of the imploding shell.[2,4–6]

Hydrodynamic instabilities, and their effects on imploding ICF capsules, have been the subject of extensive studies in the past.[2,6–11] Nonuniformities in the applied drive, coupled with imperfections at the target surface, seed Rayleigh–Taylor (RT) unstable growth at the ablation front. In addition, rarefaction waves generated at the perturbed inner ice surface, due to the breakout of the first shock, return to the ablation region and contribute to the instability there.[12–14] These perturbations feed through the shell and couple with the existing perturbations on the inner ice surface. This combination serves as the seed for RT growth at the ice/vapor interface when the ice layer begins to decelerate around the hot spot.

A good understanding of how the unstable growth of perturbations affects target performance (ignition and gain) is required to guide the development of the laser and target systems' specifications. Of specific importance is the designation of parameters dealing with the allowable levels of roughness at both the outer and inner surfaces of the capsule, the allowable limit on laser power imbalance and beam mistiming, and the amount of bandwidth requirements for single-beam uniformity. A consistent scaling that includes the net effect of all of these mechanisms acting together is developed. Such a "nonuniformity budget" adds flexibility in the design of the laser and target systems, allowing trade-offs to be made among the four sources of nonuniformity.

This article will first examine briefly the current direct-drive point design[3,6,15] for the NIF. Using one-dimensional 1-D *LILAC*[16] results, we show that the capsule design is robust. Next we examine the scaling of target gain in terms of a spectral ensemble of the rms surface roughness of the inner ice surface ($\bar{\sigma}$) at the end of the acceleration phase of the implosion. The scaling of gain with $\bar{\sigma}$, developed using the results of many two-dimensional (2-D) *ORCHID*[17] simulations, allows for the definition of a global nonuniformity budget that can ascertain the relative significance of the different nonuniformity sources in reducing capsule performance. In addition, the modeling of each of the four perturbation mechanisms is discussed. Overall target gain results are evaluated, and the scaling of the physical specification being modeled (e.g., outer-surface roughness) with $\bar{\sigma}$ is established. We also discuss the physical mechanisms that determine why target gain scales with $\bar{\sigma}$. Finally, we construct an overall nonuniformity budget for NIF systems, using the combined effects of each of the four perturbation mechanisms.

Point Direct-Drive Target Design for NIF

The base-line direct-drive designs for NIF employ a solid (cryogenic) DT-shell target with a thin polymer ablator (required to fabricate the cryogenic shell) surrounding the DT-ice shell.[3,15] The designs use shock preheat to control the isentrope of the ablation surface and the fuel. Variation in the isentrope ($\alpha = 1$ to 4, where α is the ratio of the fuel pressure to the Fermi-degenerate pressure) is achieved by varying the incident laser pulse shape. Based on the results of current OMEGA experiments and theoretical calculations of these NIF designs, we have selected the 1.5-MJ, $\alpha = 3$ design to be the point design for further study.

The point design has been shown[3] to be robust to several design uncertainties including control of laser pulse shape, material equation-of-state modeling, operating temperature, and the effects of hot electrons produced by laser–plasma instabilities (LPI). Figure 84.7(a) shows the target specification; Fig. 84.7(b) shows the pulse shape for this design. The DT-ice thickness and adiabat of the implosion determine the intensity and duration of the foot. In this design, the foot is 4.25 ns long at a power of 10 TW. This region launches a 10-Mbar shock through the DT ice. At the time of shock breakout at the rear surface of the DT ice, the pulse ramps up to the drive region, which lasts for 2.5 ns at a power of 450 TW. This rapid rise in intensity generates pressures of approximately 80 Mbar and thus accelerates the DT ice inward. The $\alpha = 3$ design is predicted, by 1-D calculations, to have a gain of 45, a neutron-averaged ion temperature of 30 keV, and a peak fuel $\rho R = 1.3$ g/cm^2. The peak in-flight aspect ratio (IFAR) of this design is 60, and the hot-spot convergence ratio is 29.

(a)

CH
1.69 mm
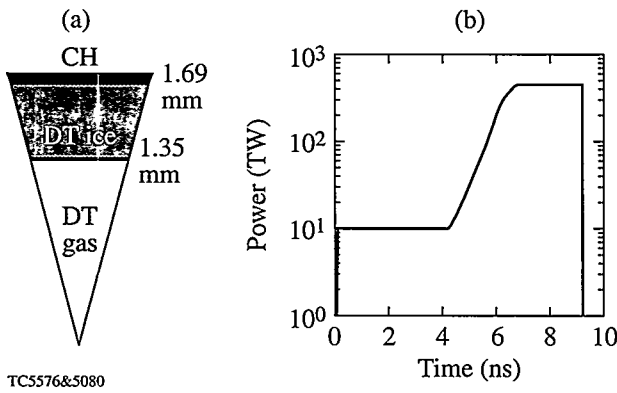DT ice
1.35 mm
DT gas

(b)

TC5576&5080

Figure 84.7
The base-line, $\alpha = 3$, "all-DT," 1.5-MJ target design. (a) The target specification and (b) the pulse shape.

Modeling Sources of Nonuniformities

During the foot pulse, the laser intensity is constant and the ablation front travels at constant velocity. While no RT unstable growth is present during this time, perturbations could still grow due to the presence of power imbalance, outer-surface roughness [Ritchmyer–Meshkov (RM)-like instability][18] and laser nonuniformity (laser imprint).[18–20] Later, when the laser intensity ramps up to drive conditions, the ablation front starts to accelerate, producing conditions for RT growth that amplify the target nonuniformities seeded during the foot pulse. Establishing the relative importance of each source of nonuniformity requires that a time in the implosion at which all sources complete their contribution to the total

nonuniformity be identified. Since perturbations due to power imbalance grow through the whole laser pulse, laser imprint and RM growth occur only during the foot pulse, and the feedout brings perturbation to the unstable ablation front during the main pulse, the best choice is at the end of the acceleration phase. At this time the ice/vapor surface perturbations decouple from the now-stable ablation surface. To construct a scaling of gain versus mode spectrum at the ice/vapor surface ($\bar{\sigma}$), 2-D ORCHID burn calculations were compiled to examine the effects of various, initially applied, ice/vapor-interface perturbation spectra ($\ell = 2$–50) on target gain. It was found that the target gain can be well represented in terms of an effective nonuniformity ($\bar{\sigma}$) that gives a reduced weight to the low-order modes ($\ell < 10$):

$$\bar{\sigma} = \sqrt{0.06\ \sigma_{\ell<10}^2 + \sigma_{\ell>9}^2},\qquad(1)$$

where $\sigma_{\ell<10}^2$ is the sum-in-quadrature of all modes of nonuniformity with $\ell < 10$ and $\sigma_{\ell>9}^2$ is the corresponding sum for $\ell > 9$. Results of this scaling, shown in Fig. 84.8, indicate that the gain threshold for point design occurs at a value of $\bar{\sigma} = 2.5$.

$$\bar{\sigma}^2 = 0.06\sigma_{\ell<10}^2 + \sigma_{\ell\geqslant10}^2$$
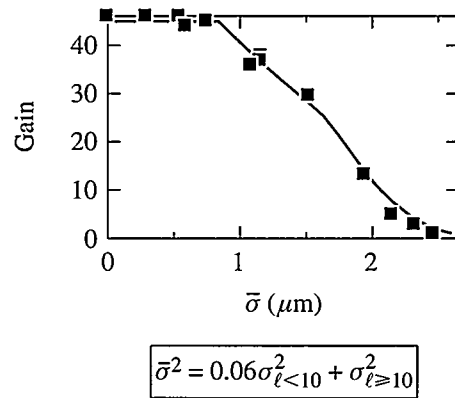
TC5137

Figure 84.8
The reduction in target gain is drawn as a function of an ensemble of modal amplitudes taken at the ice/vapor interface at the end of the acceleration phase of the implosion.

From Eq. (1), it can be seen that the high-order modes can be significantly more damaging to capsule gain than that due to the low-order modes. The small $\bar{\sigma}$ weighting of the low-order modes is just a reflection of two effects. First, as has been shown in several single-mode studies,[21,22] capsule gain is far more tolerant of levels of low-order modes than the high-order modes. Secondly, during the deceleration phase of the implosion, low-order modes experience less growth than the high

ℓ modes.[23,24] During the acceleration phase at the ablation front, the development of the high-order modes, seeded from the laser imprint, feedout from the inner ice surface, and the outer-surface roughness, is critical in determining the integrity and survivability of the shell. Due to lateral smoothing, however, the high-order modes do not feed through efficiently to the inner ice surface. The result is that the low-order modes tend to dominate the inner ice roughness at the end of the acceleration phase.[8]

These results help construct 2-D simulations of the four main perturbation mechanisms: laser imprint, power imbalance, and inner- and outer-target-surface roughness. Each of the four mechanisms was studied independently to evaluate the sensitivity of gain to variations in the laser and target system specifications. Applying the $\bar{\sigma}$ scaling to the results allows a nonuniformity budget for NIF to be determined. By establishing a global budget in terms of $\bar{\sigma}$, it is possible to evaluate the contribution of each source to the problem as a whole, providing insight into the mission-critical nonuniformities, and giving direction for trade-offs between the various sources of nonuniformity. A discussion of the modeling, sample numerical results, and how gain scales with $\bar{\sigma}$ for each perturbation mechanism follows.

1. Power Balance

The term "power balance" can be applied to a wide range of temporal, beam-to-beam intensity differences, arising from laser amplifier saturation, beam mistiming, variations in frequency conversion (angular or polarization tuning), and/or the transport of the UV energy to the target. The effects of power imbalance on the applied irradiation are modeled by determining the on-target power variations between the beams due to their propagation through the laser system. Each beam develops a unique temporal power history, which is used to calculate the irradiation nonuniformity on-target over the entire implosion. Many NIF laser power histories were calculated by Jones[25] and supplied to the authors.

Further modeling uses 1-D *LILAC* density and temperature profiles and a 2-D laser absorption routine from *ORCHID* to determine the absorbed energy at the critical surface for a single beam. This absorption profile is scaled for each beam and, using the orientation of the beam, mapped onto a sphere representing the critical surface of the target. All 192 beamlets of the NIF system are mapped to 48 unique positions on the sphere. The resulting spherical intensity distributions are then decomposed for each time and used as input to 2-D *ORCHID* simulations.

Two series of 2-D *ORCHID* runs were completed using each of the NIF power histories. The first series used the calculated power imbalance as supplied by Jones,[25] while the second series artificially doubled the power imbalance to determine ignition thresholds. In addition, further runs were compiled to assess the effects of beam mistiming for each series. A contour plot of mass density at stagnation from a typical power imbalance *ORCHID* simulation, illustrated in Fig. 84.9, clearly shows the presence of low-order modes distorting the core region. Compiling the results of these simulations, shown in Fig. 84.10, illustrates the degradation of yield with increasing on-target nonuniformities and beam-to-beam mistiming. The target gain is shown plotted against the on-target rms perturbation. The base-line NIF requirements for power balance and beam mistiming have been given as 8% rms beam-to-beam and 30-ps rms beam-to-beam, respectively.[26] The reduction in gain for these requirements is low (~10%). The results are also plotted against their calculated values of $\bar{\sigma}$ in Fig. 84.10(b). A $\bar{\sigma}$ value of ~0.85 corresponds to the NIF requirements for power imbalance.

TC5562
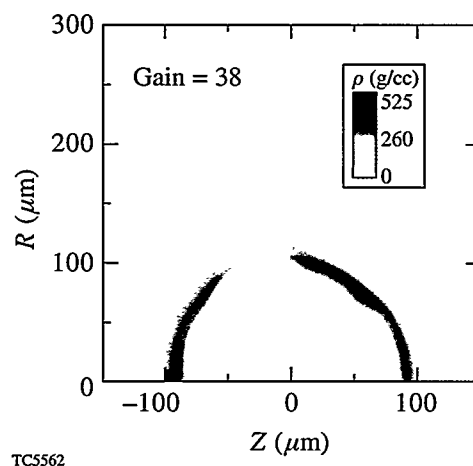
Figure 84.9

Core disruption due to NIF specifications of power imbalance and beam mistiming is dominated by low-order modes but has little effect on target gain.

2. Ice/Vapor Surface Roughness

Since there is uncertainty in the initial ice spectrum, 2-D *ORCHID* simulations were completed assuming an initial prescription for the spectral behavior and amplitude of the roughness of the form $a = a_0/\ell^\beta$. Variations in β and total σ_{rms} were examined from 0 to 1.5 and 0.5 to 12 μm, respectively. These simulations assumed smooth outer surfaces and perfect laser illumination. Figure 84.11 shows an example where the initial surface roughness of the ice/vapor interface was 3.8-μm rms (2.0-μm rms summed over modes 10 to 50) with $\beta = 0.75$.

Figure 84.11(a) illustrates the density contours of the imploding shell at stagnation. Perturbations at the ablation front are clearly visible. Comparing the roughness spectrum ice/vapor interface at the end of the acceleration phase with that of the initial spectrum, illustrated in Fig. 84.11(b), it can be seen to have increased in magnitude and steepened to a higher order of β. These results are typical of the behavior of the inner ice perturbations. They can be attributed to the unique process of feeding out to the ablation surface, undergoing RT growth, and then feeding back into the original surface. The low modes dominate with the high modes being filtered by lateral smoothing while traversing the ice layer.

The results from this series of 2-D *ORCHID* runs are compiled in Fig. 84.12. In Fig. 84.12(a), the behavior of target gain is drawn as a function of the rms of just the low-order modes ($\ell = 2$–10). These curves indicate that while the low-order modes are dominant, the high-order modes, as the applied spectra flatten, cannot be ignored. However, Fig. 84.12(b) shows the gain can be well represented by the behavior of $\bar{\sigma}$, regardless of the applied spectrum.

3. Outer-Surface Roughness

The direct-drive point design has traditionally been called the "all-DT" design, which is a misnomer. The DT-ice capsule
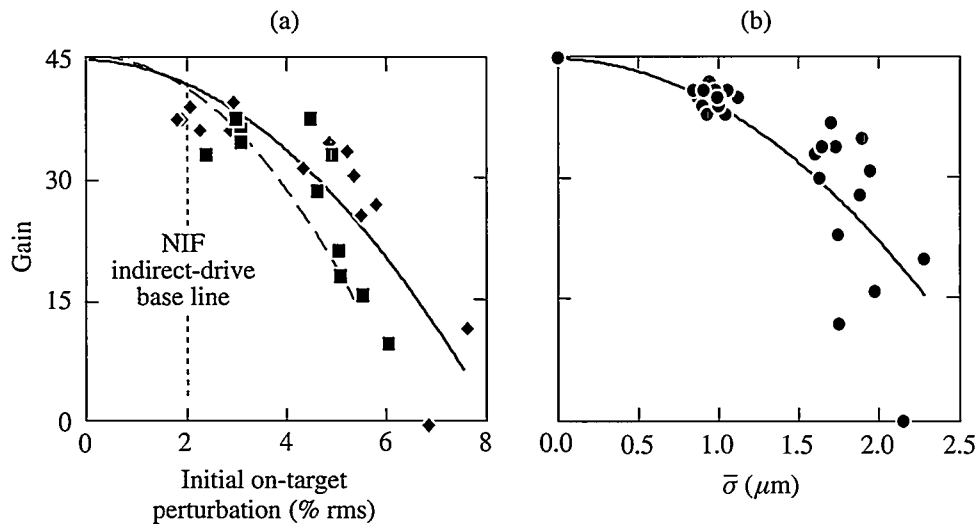
Figure 84.10
NIF laser power histories have been used to validate the NIF base-line power imbalance specifications. (a) Calculated target gain is drawn as a function of the on-target rms perturbation for beams with perfect timing (◆) and beams with a 30-ps rms (beam-to-beam) mistiming (■). (b) Calculated target gain is shown to scale well with $\bar{\sigma}$.

TC5563

TC5211
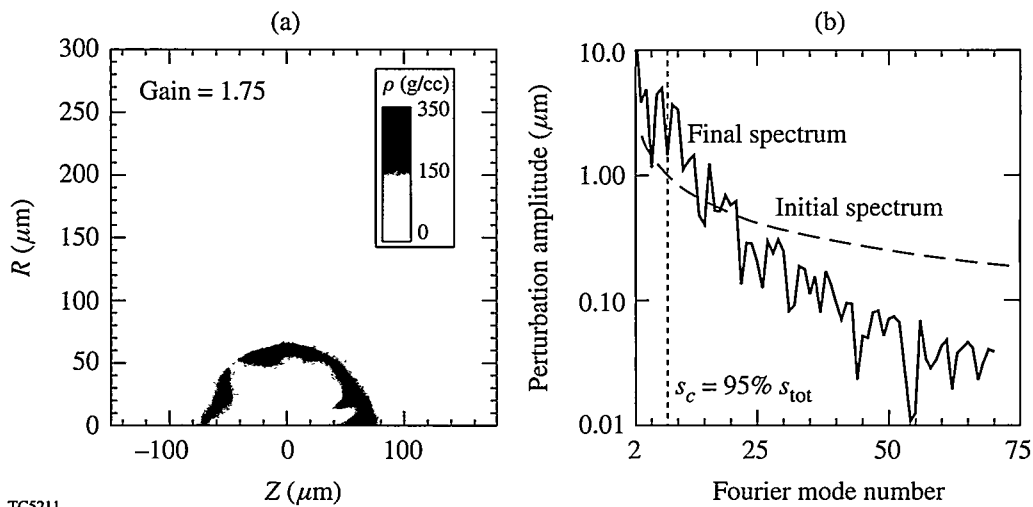
Figure 84.11

Results from *ORCHID* simulation indicate target gain depends strongly on the development of the low-order modes. (a) Density contours drawn at the time of stagnation. Note that the gain for this target was reduced from 45 to ~2. (b) Spectra of ice/vapor interface at the beginning and end of the implosion. Note the concentration of power in the low-order modes at stagnation.

is actually fabricated within a thin (1- to 2-μm) plastic micro-balloon, which serves, albeit for a short time, as an ablator. The density mismatch at the CH/DT interface can lead to additional perturbation growth at the ablation front. Indeed, when the shock reaches the interface, it produces a transmitted shock into the DT and a reflected rarefaction wave that moves back out toward the ablation surface. After the rarefaction wave breaks out at the ablation front, the latter starts to accelerate at $a \sim \left(p^{\mathrm{CH}} - p^{\mathrm{DT}}\right)/(\rho d)$, where ρ and d are initial density and thickness of CH layer, and p^{CH} and p^{DT} are the post-shock pressures in CH and DT, respectively. The acceleration occurs for a time interval $\Delta t_{\mathrm{acc}} \sim d/c_s$ (until the compression wave is generated at the ablation front), where c_s is the sound speed of the compressed ablator material. During the acceleration, the ablation surface is RT unstable, and perturbations in the front grow by a factor $\exp\left(\sqrt{ka\Delta t_{\mathrm{acc}}^2}\right) \sim \exp\left(\varepsilon\sqrt{kd}\right)$, where the coefficient ε depends on the shock strength. Furthermore, since the ablation front is rippled, the rarefaction wave breaks out first at the front's valleys and then at the peaks. Thus, there is a delay Δt_{rw} between accelerating the peaks and valleys of the ablation front. This delay creates an additional velocity perturbation $\delta v = a\Delta t_{\mathrm{rw}}$. The RT growth and δv increase the kinetic energy of the front ripple, leading to a higher perturbation amplitude. Since the RT growth factor increases with the ablator thickness d, minimizing the perturbation growth during the foot pulse requires the minimum thickness of the ablator layer.

Modeling the effects of these perturbations on indirect-drive target performance[7-10] has led to an outer-surface spectrum that is considered by target fabrication groups to be the "NIF standard." A series of 2-D *ORCHID* simulations were compiled using the NIF standard as a base-line level of surface roughness ($\sigma = \sim115$ nm). The power spectrum of the non-uniformity was then doubled and quadrupled to determine the resultant ice/vapor surface distortion at the end of the acceleration phase. As can be seen in Fig. 84.13, the effect of these

(a)   (b)

TC5564
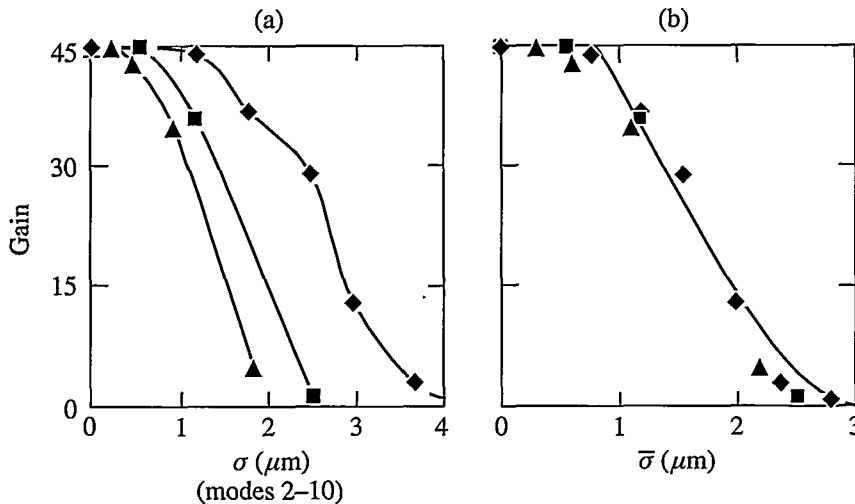
Figure 84.12
Results from *ORCHID* simulation of inner-ice-surface roughness indicate that high-order modes contribute to the reduction of capsule gain. Mode amplitudes obey $a = a_0/\ell^\beta$, $\beta = 0.00$ (▲), 0.75 (■), and 1.50 (◆). (a) Calculated target gain is drawn as a function of the initial rms finish of the ice layer in modes 2–10. (b) Calculated target gain is now drawn as a function of the calculated values of $\bar{\sigma}$.

$\bar{\sigma} = 0.15$ mm

$t = 8.8$ ns
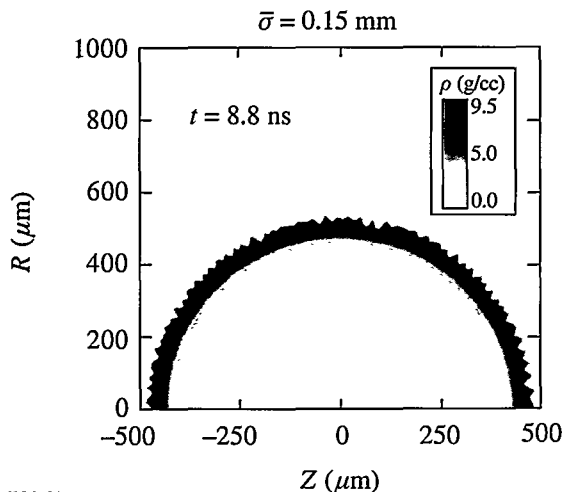
TC5455

Figure 84.13
ORCHID simulations, using twice the NIF standard surface roughness (230 nm), reveal no significant disruption of the ice/vapor interface at the end of the acceleration phase of the implosion.

levels of surface roughness on the ice/vapor interface has been minimal. While the density contours show a ~4-μm perturbation at the ablation surface, the inner-ice-surface layer shows no appreciable disruption. After analysis, the rms value of the resultant spectrum results in a value of $\bar{\sigma} \sim 0.15$. These results are consistent with Goncharov's analytic model[18,27] and indicate that the gain of the direct-drive point design is insensitive to outer-surface roughness below our calculations of ~250 nm. These results indicate that, if given the NIF standard roughness, the outer surface of the direct-drive point design will not contribute significantly to the global nonuniformity budget.

4. Laser Imprint

The last, and possibly most important, source of nonuniformity for the direct-drive point design is the imprinting of variations in the laser-beam profile onto the surface of the capsule. Our understanding of imprint is based on both theory[18,20] and experiment.[19,28] These studies have shown that, without any temporal smoothing of laser profiles, imprinted perturbations will lead to shell failure during the implosion. Smoothing of individual laser profiles is a major issue for direct drive. The direct-drive design for NIF includes the combined application of a distributed phase plate (DPP),[29,30] polarization smoothing,[31] and smoothing by spectral dispersion (SSD)[32] within each of its 192 beams.

In modeling the irradiation nonuniformity, the single-beam DPP spectrum[33] (modes 2 to 200) is modified for the 40-beam overlap and the use of polarization smoothing. The application of SSD produces statistically independent speckle patterns every $\Delta t = t_c$, where $t_c = 1/\left[\Delta v \, \sin\left(kn\delta/2\right)\right]$ is the correlation time (Δv is the laser bandwidth, n is the number of color cycles, and δ is the speckle size, which is 7 μm for NIF). The NIF

specification for smoothing has been given as 1-THz bandwidth and two color cycles. In the case of the constant-intensity foot pulse, this reduces the time-averaged laser nonuniformity by a factor $\sqrt{\left(t_c/\langle t \rangle\right)}$, where $\langle t \rangle$ is the averaging time. The longest wavelength that can be smoothed by SSD is determined by the maximum angular spread $\Delta\theta$ of the light propagating through the laser.[34] Using $\Delta\theta = 100$ μrad and a laser focal length $F = 700$ cm, SSD can smooth spherical-harmonic modes down to $\ell_{cut} = 15$. To model these intensity variations, a series of *ORCHID* simulations were compiled, randomly changing the sign of the individual laser mode amplitudes every $\Delta t = t_c$. The laser power histories for these runs were then averaged giving a smoothing rate similar to that of SSD, which was then applied to a single simulation.

Calculations for the effect of laser imprint have been performed to determine the ice/vapor distortion at the end of the acceleration phase of the implosion. Comparing the density contours of two separate implosions of the same shell, driven under different imprint scenarios, illustrates the need for this level of smoothing. The majority of *ORCHID* simulations below were performed with one color cycle to determine the minimal level of smoothing. Figure 84.14 shows the density contours for two implosions of the same shell using (a) no bandwidth and (b) 1-THz bandwidth (one color cycle). The calculated values of $\bar{\sigma}$, compiled from a series of *ORCHID* simulations, can be used to project the target gain as a function of applied bandwidth as shown in Fig. 84.15. From this graph it can be seen that deploying 1-THz bandwidth at one color cycle results in a 30% reduction in gain. For the same bandwidth higher uniformity can be achieved in the spectral range of interest by increasing the number of color cycles[31,35] (usually achieved by increasing the SSD modulator frequency). An additional *ORCHID* simulation, employing 1 THz and two
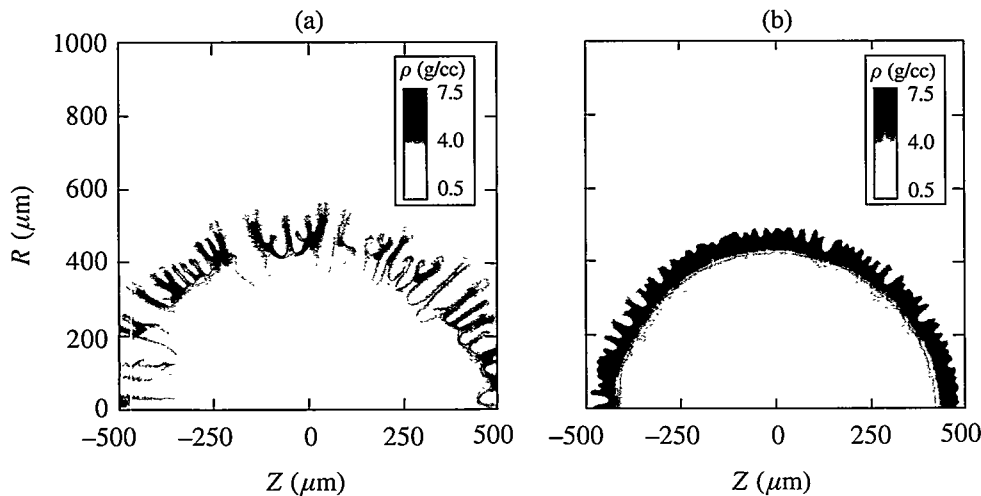

(a) (b)

Figure 84.14
The need for high levels of bandwidth and multiple color cycles is evident when comparing density contours for two implosions of the same shell, applying (a) no bandwidth or (b) 1-THz bandwidth (one color cycle).

TC5587

color cycles, was analyzed, and the result is plotted as the single annotated point in Fig. 84.15. It can be seen that either doubling the bandwidth or deploying two color cycles would recover almost the full design gain for the capsule. The NIF specifications, 1-THz bandwidth with two color cycles, correspond to a $\bar{\sigma}$ value of 1.0.
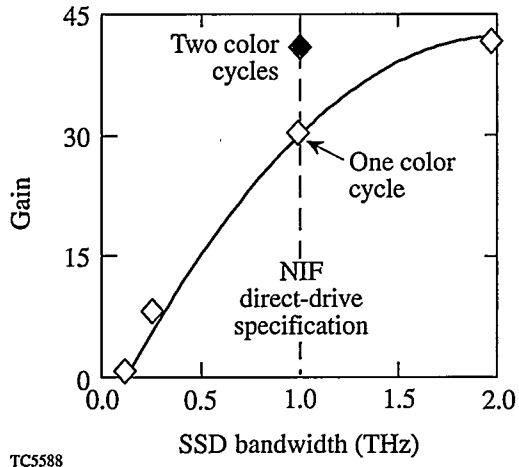

TC5588

Figure 84.15
Projected target gain, using $\bar{\sigma}$ scaling, drawn as a function of the applied laser bandwidth for the direct-drive NIF point design capsule

Gain Reduction

There are three distinct regions in the behavior of the gain as a function of $\bar{\sigma}$. The first extends from $\bar{\sigma}$ equal to zero out to about to 1, the second from 1 out to about 2.5, and the third for $\bar{\sigma}$ above 2.5. While the first and third regions are easily explained by minimal effect of small perturbations on gain in the first region and total ignition failure in the third, a consistent argument to connect the two regions while explaining the middle ground can be found by examining the sequence of events leading to high gain in an unperturbed implosion.

It is well known that the main precursor to ignition is the incoming shell motion providing PdV work to the hot spot. As the shell moves in and heats the hot spot, it also provides the necessary ρR, enabling efficient absorption of α-particle energy.[2] The combination of these two must exceed any losses due to thermal conduction and radiation transport out of the hot spot. If done correctly, ignition occurs and a burn wave begins to move out into the cold fuel shell. It is at this point, however, that the disposition of the shell re-enters the problem. As the burn wave moves out into the ice layer, it exerts a tremendous pressure on the shell. In ICF targets it is typically the hydrodynamic expansion of the ignited fuel that quenches the burn.[23] If, however, the shell still retains some of its original radial

kinetic energy, the inward momentum of the shell acts as a tamper to increase the ρR of the fuel while preventing the burn wave from decompressing the shell prematurely.

Levedahl and Lindl[36] have shown how excess kinetic energy in the shell, above that required for ignition, leads to a higher burn-up fraction. Their results show that the burn-up fraction can be drawn as a function of a dimensionless parameter that equals 1 for NIF capsules that marginally achieve ignition. As the retained kinetic energy in the shell is increased, the burn-up fraction climbs sharply until leveling off for kinetic energies in excess of 2 to 4 times the ignition energy. The sharp increase in burn-up fraction is referred to as the "ignition cliff" and indicates that NIF capsules need 1 to 2 times the kinetic energy above that which is required for ignition to achieve high gain. The ratio of excess radial kinetic energy to the maximum in-flight radial kinetic energy of the shell is referred to as "implosion margin" or simply "margin." To achieve burn-up fractions above 10% requires margins above 30%. The margin for the direct-drive point design is 40%, which results in a burn-up fraction of ~15%. The point design delivers a gain of 45, which is directly related to the burn-up fraction. The gain threshold $(G = 1)$ for this target is roughly 1.1 times the ignition energy or a margin of roughly 10%.

Margin is directly related to the hydrodynamic stagnation of the incoming shell, and typically only the pressure associated with an ignited burn wave can force the shell off its normal trajectory. If, for a moment, we examine the point design with thermonuclear burn turned off, we can see, as shown in Fig. 84.16, that the stagnating shell can lose almost half of its radial kinetic energy or margin for every 100 ps traveled. As a result, there exists a critical timing involving the onset of ignition and the decreasing margin in the shell. If ignition is delayed beyond the time at which the point design would normally ignite $(t = 0$ in Fig. 84.16), the shell's margin drops and the final gain is diminished. If ignition is delayed too long, the shell will stagnate, the PdV work will cease, and the implosion will fail. Recalling that the margin for the gain threshold is roughly 10%, the high-gain window for this target, as shown in Fig. 84.16, is ~120 ps.

One of the roles of increasing perturbations at the ice/vapor interface is to delay the onset of ignition. As was pointed out by Levedahl and Lindl[37] and Kishony,[22] one can view increasing perturbation amplitudes as being an equivalent reduction in implosion velocity. The increased surface area and perturbed volume of the hot spot allow for an increase in the thermal

conduction losses and a decrease in the absorbed energy density of α particles within the hot spot. To reach ignition requires that the hot spot be driven to a higher ρR to recoup these losses. A high-gain shell, by our definition, still has excess kinetic energy to complete the task; however, this delays ignition and depletes the shell of valuable margin. The results of ORCHID simulations clearly show, as displayed in Fig. 84.17(a), how increasing $\overline{\sigma}$ affects ignition timing and the margin of the implosion. The point design resides in a linear, albeit steep, region of the ignition cliff. One should then expect a linear response of the burn-up fraction (i.e., gain) to changes
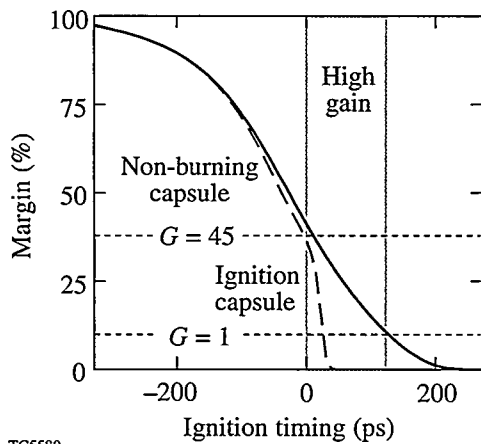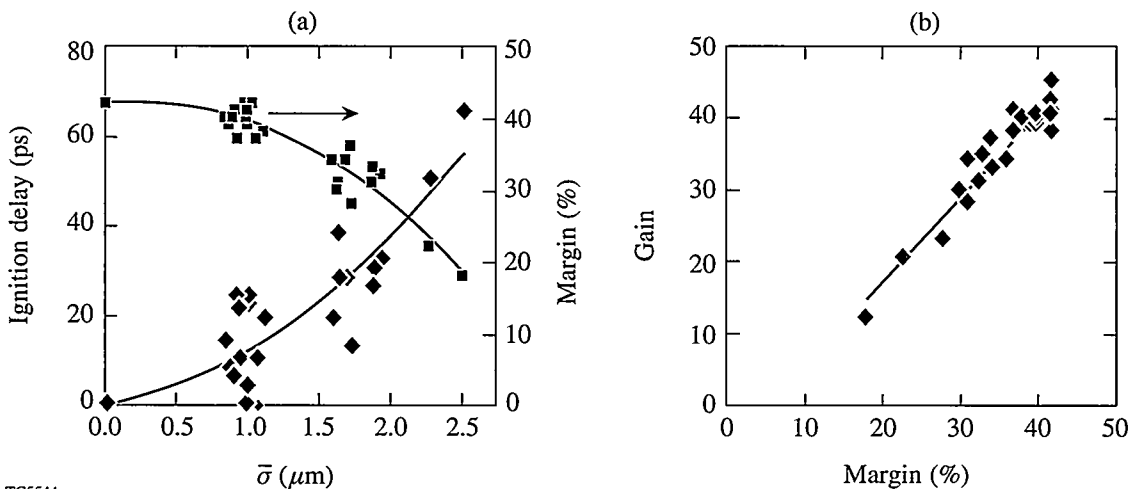
in implosion margin. Such a linear behavior is clearly indicated in Fig. 84.17(b), where the calculated gains from the ORCHID simulations are drawn as a function of their calculated margin. The argument of increasing shell nonuniformities effectively depleting the shell margin explains the performance of targets giving intermediate gains for intermediate values of $\overline{\sigma}$.

Uniformity Budget for NIF

A global nonuniformity budget for the direct-drive point design on NIF can now be constructed in terms of $\overline{\sigma}$. If each of the four sources of nonuniformity acts independently, then the total effect can be measured by adding the individual $\overline{\sigma}$'s in quadrature $\overline{\sigma}_t$. Figure 84.18 displays the dependence of $\overline{\sigma}$ for each of the four main sources as a function of their individual laser and target specifications. Specification values have been scaled to reflect a universal multiplier that serves as the y axis. The sum-in-quadrature value $\overline{\sigma}_t = 1.4$ for this system (using current NIF specifications with two color cycles) is plotted as the solid dot on the inset graph of gain versus $\overline{\sigma}_t$ and represents a capsule gain of slightly greater than 30. The largest contributor can be seen to be the effects of laser non-uniformity. While the on-target power imbalance also makes a strong contribution, the effects due to the roughness of the ice/vapor interface are manageable and those due to outer-surface roughness are of no real consequence. If the NIF specifications of two color cycles are not achieved and only one color cycle is used, then the combined $\overline{\sigma}_t$ increases from 1.4 to 1.75, as seen in Fig. 84.10. The resultant target gain drops from 30 to 20. At one color cycle, the gain could be brought back to 30 by

Figure 84.16

Shell stagnation determines the margin trajectory, which, in turn, defines the window for high gain.

TC5580

TC5544

Figure 84.17

ORCHID simulations indicate that hot-spot ignition is delayed as ice/vapor interface perturbations increase. (a) Increasing shell perturbations ($\overline{\sigma}$) act to increase ignition delay (♦). This delay causes the burn wave to sample a shell with decreased margin (■). (b) Capsule gain depends strongly on the shell margin at ignition.

doubling the bandwidth, but this has been precluded by the efficiency of the frequency-tripling crystals. The achievement of two color cycles is consistent with current-day technology, but propagation issues through the laser chain must still be examined. At the two-color-cycle level, even higher gains can be achieved with improvements in power-balance technology.
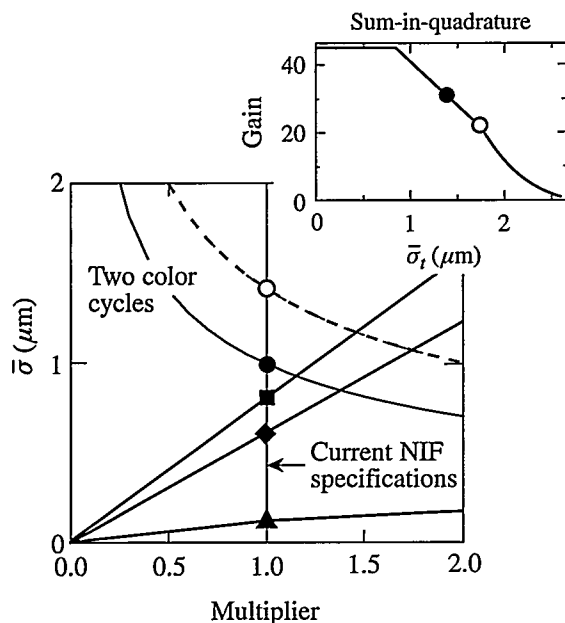
TC5577

Figure 84.18
ORCHID results can be used to scale the target gain with $\bar{\sigma}$ to form a global nonuniformity budget for the direct-design point design. The *y* axis scales to the parameters: SSD bandwidth, one color cycle (o, × 1 THz); SSD bandwidth, two color cycles (●, × 1 THz); on-target power imbalance (■, × 2% rms); inner ice roughness (♦, × 1 μm rms); and outer-surface roughness (▲, × 80 nm).

Conclusions

Capsule gain can be directly related to the kinetic energy of the incoming shell that is in excess of the energy required to achieve ignition. When related to the peak kinetic energy of the implosion, this excess kinetic energy can be cast in terms of an implosion margin. Shell margin, prior to ignition, depends only on the temporal stagnation of the shell. As such, high gain requires the onset of ignition to coincide with significant (~40%) retained shell margin. Our analysis indicates that increasing perturbations in the incoming shell delay the onset of ignition within the hot spot. During this delay, the shell continues to stagnate and lose valuable margin. When ignition does occur, the burn wave samples the depleted shell margin allowing the high ignition pressure to decompress the main fuel layer prematurely, which leads to reduced gain. If the

perturbations of the incoming shell delay ignition too long, the shell will stagnate, the PdV work will cease, and the implosion will fail.

The two-dimensional hydrodynamics code *ORCHID* has been used to examine the target performance of the NIF direct-drive point design driven under the influence of the four main sources of nonuniformity: laser imprint, power imbalance, and inner- and outer-target-surface roughness. Results from these studies indicate that capsule gain can be scaled to the rms spectrum of the ice/vapor surface deformation at the end of the acceleration stage of the implosion. Applying this scaling shows that NIF direct-drive point design performance is most sensitive to the effects of SSD smoothing, followed by power imbalance, inner-ice-surface roughness, and outer-surface roughness. A global nonuniformity budget was constructed using the scaling of a varied set of *ORCHID* simulations to evaluate the net effect of all nonuniformities acting together. This budget indicates that, if laser smoothing, power imbalance, and both inner- and outer-surface roughness stay within the limits specified by NIF direct-drive requirements, the capsule shell remains intact during the implosion and the implosion results in $G \sim 30$.

REFERENCES

1. M. D. Campbell and W. J. Hogan, Plasma Phys. Control. Fusion **41**, B39 (1999).

2. J. D. Lindl, Phys. Plasmas **2**, 3933 (1995).

3. Laboratory for Laser Energetics LLE Review **79**, 121, NTIS document No. DOE/SF/19460-317 (1999). Copies may be obtained from the National Technical Information Service, Springfield, VA 22161.

4. Lord Rayleigh, in *Scientific Papers* (Cambridge University Press, Cambridge, England, 1900), Vol. II, pp. 200–207.

5. M. S. Plesset, J. Appl. Phys. **25**, 96 (1954); G. I. Bell, Los Alamos National Laboratory, Report No. LA-1321 (1951).

6. S. E. Bodner, D. G. Colombant, J. H. Gardner, R. H. Lehmberg, S. P. Obenschain, L. Phillips, A. J. Schmitt, J. D. Sethian, R. L. McCrory, W. Seka, C. P. Verdon, J. P. Knauer, B. B. Afeyan, and H. T. Powell, Phys. Plasmas **5**, 1901 (1998).

7. S. W. Haan *et al.*, Phys. Plasmas **2**, 2480 (1995).

8. M. M. Marinak *et al.*, Phys. Plasmas **5**, 1125 (1998).

9. T. R. Dittrich *et al.*, Phys. Plasmas **5**, 3708 (1998).

10. S. V. Weber, S. G. Glendinning, D. H. Kalantar, M. H. Key, B. A. Remington, J. E. Rothenberg, E. Wolfrum, C. P. Verdon, and J. P. Knauer, Phys. Plasmas **4**, 1978 (1997).

11. V. N. Goncharov, S. Skupsky, P. W. McKenty, J. A. Delettrez, R. P. J. Town, and C. Cherfils-Clérouin, in *Inertial Fusion Sciences and Applications 99*, edited by C. Labaune, W. J. Hogan, and K. A. Tanaka (Elsevier, Paris, 2000), pp. 214–219.

12. R. Betti, V. Lobatchev, and R. L. McCrory, Phys. Rev. Lett. **81**, 5560 (1998).

13. D. P. Smitherman *et al.*, Phys. Plasmas **6**, 932 (1999).

14. K. Shigemori *et al.*, Phys. Rev. Lett. **84**, 5331 (2000).

15. C. P. Verdon, Bull. Am. Phys. Soc. **38**, 2010 (1993).

16. M. C. Richardson, P. W. McKenty, F. J. Marshall, C. P. Verdon, J. M. Soures, R. L. McCrory, O. Barnouin, R. S. Craxton, J. Delettrez, R. L. Hutchison, P. A. Jaanimagi, R. Keck, T. Kessler, H. Kim, S. A. Letzring, D. M. Roback, W. Seka, S. Skupsky, B. Yaakobi, S. M. Lane, and S. Prussin, in *Laser Interaction and Related Plasma Phenomena*, edited by H. Hora and G. H. Miley (Plenum Publishing, New York, 1986), Vol. 7, pp. 421–448.

17. R. L. McCrory and C. P. Verdon, in *Inertial Confinement Fusion*, edited by A. Caruso and E. Sindoni (Editrice Compositori, Bologna, Italy, 1989), pp. 83–124.

18. V. N. Goncharov, Phys. Rev. Lett. **82**, 2091 (1999); R. Ishizaki and K. Nishihara, Phys. Rev. Lett. **78**, 1920 (1997); R. J. Taylor *et al.*, Phys. Rev. Lett. **79**, 1861 (1997); A. L. Velikovich *et al.*, Phys. Plasmas **5**, 1491 (1998).

19. S. P. Obenschain *et al.*, Phys. Rev. Lett. **46**, 1402 (1981); S. G. Glendinning, S. N. Dixit, B. A. Hammel, D. H. Kalantar, M. H. Key, J. D. Kilkenny, J. P. Knauer, D. M. Pennington, B. A. Remington, R. J. Wallace, and S. V. Weber, Phys. Rev. E **54**, 4473 (1996); R. J. Taylor *et al.*, Phys. Rev. Lett. **76**, 1643 (1996); C. J. Pawley *et al.*, Phys. Plasmas **4**, 1969 (1997); V. A. Smalyuk, T. R. Boehly, D. K. Bradley, V. N. Goncharov, J. A. Delettrez, J. P. Knauer, D. D. Meyerhofer, D. Oron, D. Shvarts, Y. Srebro, and R. P. J. Town, Phys. Plasmas **6**, 4022 (1999).

20. V. N. Goncharov, S. Skupsky, T. R. Boehly, J. P. Knauer, P. McKenty, V. A. Smalyuk, R. P. J. Town, O. V. Gotchev, R. Betti, and D. D. Meyerhofer, Phys. Plasmas **7**, 2062 (2000).

21. Laboratory for Laser Energetics LLE Review 23, 125, NTIS document No. DOE/SP40200-03 (1985). Copies may be obtained from the National Technical Information Service, Springfield, VA 22161.

22. R. Kishony, "Ignition Criterion in Inertial Confinement Fusion Using Self-Similar Solutions, and the Effect of Perturbations on Ignition," Ph.D. thesis, Tel Aviv University, 1999.

23. J. D. Lindl, *Inertial Confinement Fusion: The Quest for Ignition and Energy Gain Using Indirect Drive* (Springer-Verlag, New York, 1998), p. 3.

24. V. Lobatchev and R. Betti, "Ablative Stabilization of the Deceleration-Phase Rayleigh-Taylor Instability," to be published in Physical Review Letters.

25. O. S. Jones, Lawrence Livermore National Laboratory, private communication (2000).

26. O. S. Jones *et al.*, in *NIF Laser System Performance Ratings*, Supplement to Third Annual International Conference on Solid State Lasers for Application to Inertial Confinement Fusion (SPIE, Bellingham, WA, 1998), Vol. 3492, pp. 49–54.

27. V. N. Goncharov, P. McKenty, S. Skupsky, R. Betti, R. L. McCrory, and C. Cherfils-Clérouin, "Modeling Hydrodynamic Instabilities in Inertial Confinement Fusion Targets," to be published in Physics of Plasmas.

28. T. R. Boehly, V. N. Goncharov, O. Gotchev, J. P. Knauer, D. D. Meyerhofer, D. Oron, S. P. Regan, Y. Srebro, W. Seka, D. Shvarts, S. Skupsky, and V. A. Smalyuk, "Optical and Plasma Smoothing of Laser Imprinting in Targets Driven by Lasers with SSD Bandwidths Up to 1 THz," to be published in Physics of Plasmas.

29. Y. Kato *et al.*, Phys. Rev. Lett. **53**, 1057 (1984).

30. Laboratory for Laser Energetics LLE Review 33, 1, NTIS document No. DOE/DP/40200-65 (1987). Copies may be obtained from the National Technical Information Service, Springfield, VA 22161.

31. T. R. Boehly, V. A. Smalyuk, D. D. Meyerhofer, J. P. Knauer, D. K. Bradley, R. S. Craxton, M. J. Guardalben, S. Skupsky, and T. J. Kessler, J. Appl. Phys. **85**, 3444 (1999).

32. Laboratory for Laser Energetics LLE Review 36, 158, NTIS document No. DOE/DP/40200-79 (1988). Copies may be obtained from the National Technical Information Service, Springfield, VA 22161.

33. R. Epstein, J. Appl. Phys. **82**, 2123 (1997).

34. S. Skupsky and R. S. Craxton, Phys. Plasmas **6**, 2157 (1999).

35. R. H. Lehmberg, A. J. Schmitt, and S. E. Bodner, J. Appl. Phys. **62**, 2680 (1987).

36. W. K. Levedahl and J. D. Lindl, Nucl. Fusion **37**, 165 (1997).

37. *ibid.*, p. 171.

Core Performance and Mix in Direct-Drive Spherical Implosions with High Uniformity

Introduction

In the direct-drive approach to laser-driven inertial confinement fusion (ICF)[1] a spherical target is symmetrically illuminated by a number of individual laser beams. One of the primary determinants of target performance is illumination uniformity, both individual-beam uniformity and on-target beam-to-beam power history differences (power balance). Illumination nonuniformities lead to distortions in the compressed core due to secular growth of low-order ($\ell \leq 10$) modes and shell breakup and mix due to the Rayleigh–Taylor (RT)[2,3] growth of perturbations imprinted by high-order ($\ell > 10$) nonuniformities. To reduce the effect of imprinting, a number of beam-smoothing techniques have been employed, including distributed phase plates (DPP's),[4] polarization smoothing (PS) with birefringent wedges,[5,6] smoothing by spectral dispersion (SSD),[7] and induced spatial incoherence (ISI).[8] Ultimately to ignite a direct-drive cryogenic pellet, the on-target beam nonuniformity must be less than 1%.[3,9,10]

An ICF target is RT unstable during two phases of the implosion: During the acceleration phase, surface nonuniformities seeded by laser nonuniformities, outer-target-surface roughness, and feedout of inner-target-surface roughness grow at the ablation front. Under extreme conditions, the perturbations can grow to be comparable to the in-flight shell thickness disrupting the shell or by feeding perturbations through the remaining shell material, seeding the deceleration-phase RT instability. During the deceleration and core assembly phases the boundary between the high-temperature, low-density hot spot and the colder, high-density pusher (shell) is RT unstable.

Beam uniformity's effect on target performance is studied in direct-drive implosions of gas-filled plastic shells on the OMEGA laser system.[11] These targets are surrogates[12,13] for cryogenic implosions that have recently commenced on OMEGA. These cryogenic implosions are energy-scaled surrogates for direct-drive ignition targets on the National Ignition Facility.[3,9,10,14] Implosions of 20-μm-thick, gas-filled plastic shells driven with a 1-ns square laser pulse have ratios

of the thickness of the ablation-surface mix region due to RT growth to the in-flight shell thickness that are similar to those predicted for OMEGA cryogenic implosions (see Fig. 84.19). The in-flight shell thickness was calculated using the 1-D hydrodynamic code $LILAC$,[15] and the mix width was calculated using a postprocessor that includes the effects of mass ablation, finite shell thickness, and spherical convergence.[16] Three different CH-shell-implosion conditions were calculated. Plastic shell implosions are useful because a wide variety
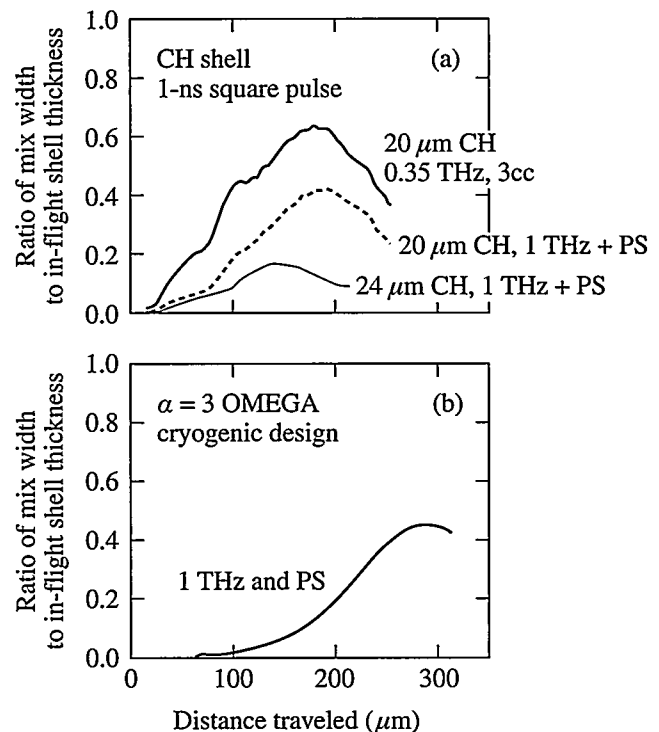
Figure 84.19
(a) Ratio of the calculated acceleration phase "mix" width to the in-flight shell thickness for 20-μm-thick CH shells illuminated by 1-ns square pulses with 1-THz SSD and PS (dashed line); 0.35-THz, three-color-cycle SSD without PS (thick solid line); and for a 24-μm-thick CH shell illuminated with 1-THz SSD and PS (thin solid line). For full smoothing, the width of the mix region is significantly smaller than the in-flight shell thickness. (b) A similar comparison for NIF-scaled cryogenic targets planned for OMEGA is shown.

E10705

of shell/gas conditions and diagnostics can be applied to study the details of the implosion.[17–19]

This article describes a series of OMEGA direct-drive plastic shell implosions with high-quality beam smoothing and power balance. These experiments suggest that the shell remains reasonably integral during the acceleration phase and that single-beam nonuniformity is no longer the primary limitation on target performance. A wide variety of target types and fill gasses are used to build a model of core conditions and fuel–shell mixing.

The sections that follow describe the targets and diagnostics applied to the spherical implosions, the laser conditions for the implosions, the target performance, and a static mix model. This work is summarized in the last section.

Targets and Diagnostics

The philosophy of the experiments reported here is to first choose a laser pulse shape, smoothing conditions, target-shell thickness, and gas-fill pressure, and then vary the make-up of the fill gas or details of the shell layers so that many diagnostics can be applied to the nearly identical implosions. OMEGA produces very reproducible implosions suggesting that the implosion hydrodynamics is unchanged for different target types and fill-gas make-up.

1. Core Diagnostics

The primary (N_p) and secondary neutron (N_s) yields were measured using scintillator counters coupled to fast photomultipliers.[20] Indium and copper activation provided additional yield measurements.[21] For the range of yields recorded, the typical uncertainty in these measurements was 10%. The fast scintillator counters also measured the neutron-averaged ion temperature with an uncertainty ~0.5 keV.

The secondary proton and knock-on particle yields were measured with range filters[22] and charged-particle spectrometers (CPS's).[23] CR-39 nuclear emulsion was used in both detectors to determine the yield and the energy spectrum.

For DT-filled implosions, the fuel areal density is determined from the number of elastically scattered knock-on fuel particles:[24,25]
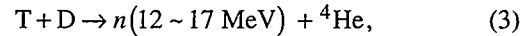
$$n + T(D) \rightarrow n' + T'(D').$$

(1)

The yield of knock-on particles is insensitive to the electron temperature profile.[24,25]

Limits on fuel areal density (ρR_f) in D_2-filled implosions can be inferred from the secondary neutron (N_s) production[22,26]
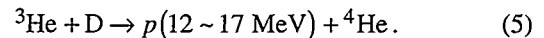
$$D + D \rightarrow T + p,$$

(2)

followed by

$$T + D \rightarrow n(12 \sim 17 \text{ MeV}) + {}^4\text{He},$$

(3)

and secondary proton production (p_s)[22,26]

$$D + D \rightarrow {}^3\text{He} + n,$$

(4)

followed by

$${}^3\text{He} + D \rightarrow p(12 \sim 17 \text{ MeV}) + {}^4\text{He}.$$

(5)

The secondary proton and neutron yields depend on the electron temperature profile in the core and typically provide limits on the ρR_f and the core electron temperature.[22,26]

The inferred value of ρR_f depends on whether a hot spot (point-like source surrounded by uniform fuel) or uniform (uniform fuel and source) "ice-block" model is used. The ρR_f inferred with the uniform model is ~34% larger than with the hot-spot model.[22,26] Simulations using *LILAC*[15] suggest that the uniform model is more appropriate for inferring ρR_f under the experimental conditions described in this work.

2. Shell Diagnostics

The areal density of the plastic shell, ρR_s, during stagnation was measured with charged-particle spectroscopy. Secondary protons from D_2 implosions (produced with 12- to 17-MeV energies) are slowed down predominantly in the shell by an amount proportional to ρR_s.[22] For CH shells with DT fill, the number of knock-on protons determines ρR_s.[25] In addition, knock-on deuterons and tritons are slowed in the shell, providing another measure of ρR_s and, coupled with the knock-on proton yield, provide an estimate of the shell electron temperature.[25]

3. Mix Diagnostics

The core–fuel mix characteristics are inferred in a number of ways. CD layers in D_2-filled CH targets are probed with tritons and ${}^3\text{He}$ particles produced in the D_2 reaction in the fuel region [Eqs. (2)–(5)].[27] The measured secondary yields from the shell regions are compared to 1-D simulations. When the yields are significantly different than those predicted, they

provide information about fuel–shell mix. The secondary DT neutrons and D-^{3}He protons produced directly in the shell can be subtracted using H_2-filled implosions with the same shell conditions. An implosion of a plastic shell with a CD layer and a pure-^{3}He fill provides a primary D-^{3}He proton signal only if the shell and fuel regions are microscopically mixed. This yield depends on the characteristics of the mix, either microscopic (diffusive) or macroscopic, where islands of shell material penetrate the core.

Laser Conditions

An ~23-kJ, 1-ns square pulse delivered by the 60-beam OMEGA laser system[11] was used to drive the implosions described in this work. Figure 84.20 shows the measured pulse shapes for 50 of the 60 beams. The beam-to-beam UV energy balance (thick line in Fig. 84.20) is typically ≤ 5% rms. When beam overlap on target is included, the on-target nonuniformity due to beam-to-beam power imbalance is <2% ($\ell \leq 12$). Individual-beam smoothing was accomplished by combining DPP's, SSD, and PS (in most cases). The DPP's produce a third-order supergaussian profile with 95% of the energy enclosed in an ~936-μm diameter. When 2-D SSD and PS are added, the spot diameter increases somewhat due to the angular divergence associated with these techniques. Two different, two-dimensional (2-D) SSD configurations were used: a single color cycle with 1-THz bandwidth at 3- and 10-GHz modulation frequencies or a three-color-cycle configuration with 0.35-THz bandwidth with 3- and 3.3-GHz

Shot 20705 power balance
smoothed, timebase corrected

Figure 84.20
The measured 1-ns square pulse from 50 of the 60 OMEGA beams for shot 20705 (thin lines). The thick line shows the rms beam-to-beam power imbalance inferred for the same shot. For most of the pulse, the power imbalance is ~5%.

modulation frequencies. Polarization smoothing with birefringent wedges was employed on the implosions with 1-THz SSD.

The calculated time-dependent, on-target nonuniformity ($\ell = 1 \sim 500$) due to single-beam nonuniformity assuming perfect beam-to-beam power balance for 1-THz SSD with PS is less than 1% after 300 ps.[28] Additional on-target nonuniformities are due to beam-to-beam power imbalance and differences in DPP spot sizes.

Implosion Results

This section describes a series of gas-filled plastic (CH) shell implosions driven with a ~23 kJ, 1-ns square pulse. Most of the implosions were driven with full beam uniformity (1-THz SSD and PS), while 0.35-THz SSD (three color cycles without PS) was used for the others. The ~940-μm-diam plastic targets had 18~24-μm wall thicknesses and were filled with fuel pressures of 3~15 atm. The targets were predicted to have gas convergence ratios of ~35 and ~14, respectively, from 1-D hydrodynamic simulations.[15]

The ratio of the measured primary neutron yield to that predicted by 1-D simulations ["yield over clean" (YOC)] for CH shells with D_2 fills as a function of the calculated convergence ratio (initial to final radius of the fuel–shell boundary) for 1-THz SSD and PS is shown in Fig. 84.21. The 20- and 24-μm-thick shells were filled with either 3 or 15 atm of D_2. The OMEGA laser system provides highly reproducible implosions, as can be seen by the small spread in the YOC's for each condition. The implosions with 15-atm-filled, 20-μm-thick shells were taken over three experimental campaigns spanning two months and show an ~10% standard deviation of YOC's. The implosions with convergence ratio ~35 have YOC's of ~20%. The most-stable implosions (24-μm-thick shells with 15-atm fills) have YOC's ≈ 40%.

The measured and calculated neutron-production rates for a 20-μm-thick CH shell filled with 15 atm of D_2 are compared in Fig. 84.22. The two temporal histories are in good agreement except that the measured neutron-production rate is ~35% of the calculated one. There is no evidence that the measured neutron burn rate decreases before the time predicted by 1-D simulations (i.e., no early burn termination). Over many target implosions, the measured time of peak neutron emission (bang time) is within 50 ps of that predicted.

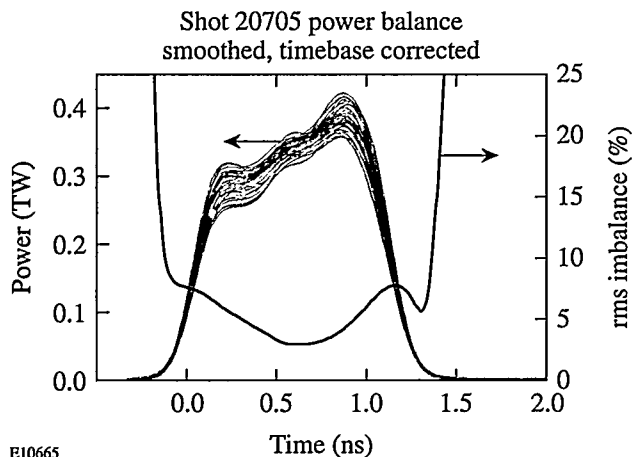For 20-μm-thick CH shells with 15-atm-D_2 or DT fill pressures, the predicted ρR_f is 16 mg/cm^2 and ρR_s is 60 mg/cm^2.

The measured charged-particle spectra used to determine the fuel, shell, and total areal densities of these implosions are shown in Figs. 84.23–84.25. Figures 84.23 and 84.24 show the measured knock-on D and p spectra for CH shells filled with DT. The ρR_f inferred from D knock-on yield is 16 mg/cm^2, while $\rho R_s \sim 61$ mg/cm^2 from the knock-on protons. The total ρR can also be determined from the slowing down of D-^{3}He secondary protons from D$_2$-filled shells (Fig. 84.25), and it is found to be 76 mg/cm^2. These measurements show that the sum of fuel and shell areal densities for DT implosions is in good agreement with the total areal density independently inferred from D$_2$ implosions. The measured fuel and shell areal densities are close to those predicted from 1-D simulations.

These results were compared with target implosions driven with similar laser pulse shapes and with larger single-beam nonuniformities (0.35-THz, three-color-cycle SSD without PS). *LILAC* simulations predicted identical target performance. Table 84.II compares the measured implosion parameters for 20-μm-thick CH shells with 15-atm-gas fills of D$_2$ and DT driven under identical conditions, except for the single-beam nonuniformity. In all aspects, the implosions driven with more-uniform beams performed significantly better. In particular both the primary neutron yield and fuel areal density increased by ~70%.
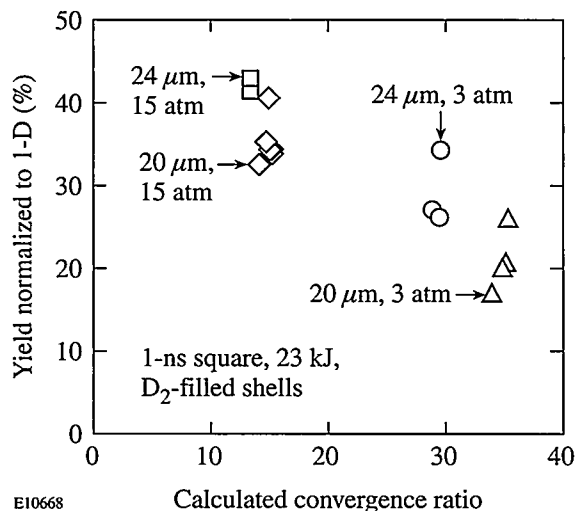

Figure 84.21
Ratio of the measured to calculated primary neutron yield (YOC) for D$_2$-filled CH capsule implosions as a function of calculated convergence ratio for 1-THz SSD and PS. This shows both the high reproducibility of the OMEGA laser system and good performance at convergence ratios of ~35.

Figure 84.23
The measured "knock-on" deuteron spectrum for a 15-atm-DT fill in a 20-μm-thick CH shell. The estimated fuel areal density is 16 mg/cm^2 (Ref. 25).
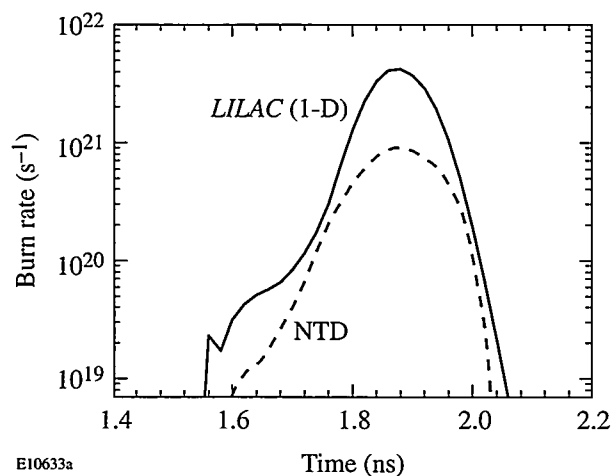

Figure 84.22
The time-dependent, measured (dashed) and predicted (solid) neutron-production rates for a 15-atm-DT fill in a 20-μm-thick CH shell are overlaid.
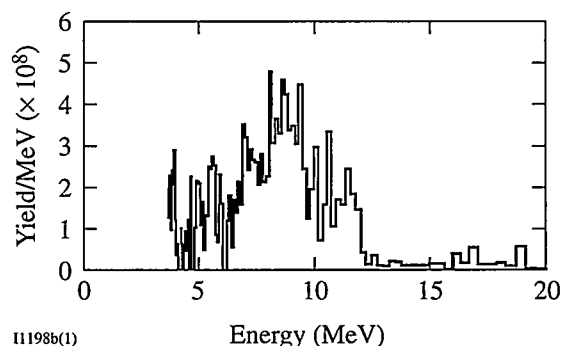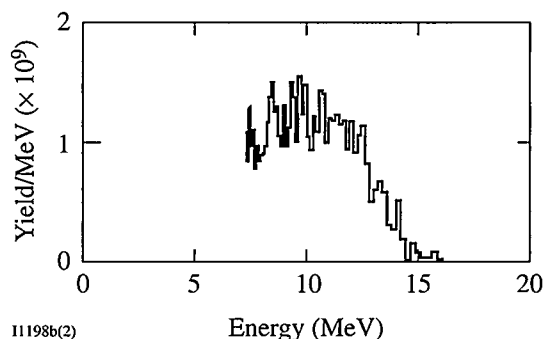

Figure 84.24
The measured knock-on proton spectrum for a 15-atm-DT fill in a 20-μm-thick CH shell. The estimated shell areal density is 61 mg/cm^2 (Ref. 25).

In summary, high-uniformity, moderate-convergence-ratio implosions with 15-atm-gas-fill pressure have YOC's of ~40% and compressed fuel and shell areal densities close to those predicted. Figure 84.19(a) shows the predicted ratio of the imprint-induced mix width to the shell thickness for three implosions. When full smoothing (1-THz SSD and PS) is applied to 20-μm-thick shells, the mix width is predicted to be ~42% of the in-flight shell thickness compared with 65% for 0.35-THz SSD without PS. The primary yields and fuel areal densities increased by ~70% for the 1-THz and PS implosion, indicating that the reduction of mix width and corresponding improvement in shell stability significantly affected the target performance. The 24-μm-thick CH shells with 15-atm fills show a further 25% improvement in YOC compared to 20-μm-thick shells using full beam smoothing. If the imprint-induced shell stability were still the dominant determinant of target performance, reducing the ratio of the mix width to in-flight shell thickness from 42% to 17% might have been expected to

I1198b(3)

Figure 84.25
The measured secondary D-^{3}He proton spectrum for a 15-atm-D$_2$ fill in a 20-μm-thick CH shell. The estimated total areal density is 76 mg/cm^2 (Ref. 22).

improve target performance significantly further. While shell stability still plays a role in target performance, it appears that other effects, such as power imbalance, play a comparable role.

Core Mix Model

In the preceding sections, the experimental results have been compared with the predictions of 1-D hydrodynamic simulations. While some observations are close to those predicted, others, such as the primary yield, are lower, while still others, such as the ratio of the secondary neutron yield to the primary neutron yield, are larger. The variation in observables provides constraints on the possible core conditions and fuel–pusher mix during stagnation. In this section, the experimental results are compared to a static model of the core to gain additional insight about target performance.[29]

The predictions of this static model are compared to neutron-burn-averaged observations. This model assumes that the compressed core can be divided into two regions: a "clean" region with only fuel material and a "mixed" region where some of the shell material is mixed with the fuel material. The clean region is characterized by a single temperature (electron and ion are assumed to be the same), fuel density, and radius. In the mix region, the fuel density decreases linearly from the edge of the clean region to the edge of the mix region, the shell material density decreases linearly from the edge of the mix region to the boundary of the clean region, and the temperature decreases linearly from the edge of the clean region to the edge of the mix region. Thus, the model has six parameters: the temperature, density, and radius of the clean region; the radius of the mix region; and the shell material density and temperature at the edge of the mix region. The total fuel mass is
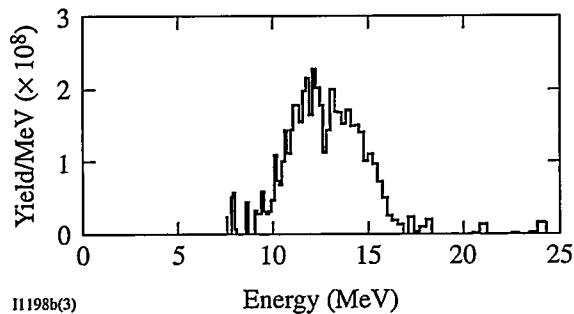
Table 84.II: Comparison of implosion performance of ~19-μm-thick CH shells filled with 15 atm of D$_2$ or DT fill with 1-THz SSD and PS or 0.35-THz SSD (three color cycles) without PS.

Diagnostic	0.35-THz SSD	1-THz SSD and PS
D$_2$ primary yield (10^{10})	9±1	16±1
T_{ion} (D$_2$) (keV)	3.2±0.5	3.7±0.5
Secondary neutron ratio (Y_{2n}/Y_n 10^{-3})	1.5±0.4	2.5±0.2
Secondary proton ratio (Y_{2p}/Y_n 10^{-3})	1.4±0.2	1.9±0.2
DT primary yield (10^{12})	6±1	11±1
T_{ion} (DT) (keV)	3.7	4.4 keV
Knock-on fuel ρR (mg/cm^2)	9±2	15±2

assumed to be conserved. The nuclear and particle emission from the compressed core in the model must match the measured values of primary neutron burn rate, average neutron ion temperature, secondary neutron, proton, and knock-on yields (both for CH shells and CH shells with inner CD layers). CH shells with inner CD layers filled with ^{3}He fuel provide additional experimental observations. Approximately ten experimental observables are used to constrain the model's parameters. The core temperature and density profiles inferred from this model for 15-atm-filled, 20-μm-thick plastic shells are shown in Fig. 84.26. The range of allowable parameters is shown in the figure as the width of parameter estimates. The measured values of various parameters and their fraction (in percent) predicted by the model are shown in Table 84.III. The model predicts that the total compressed radius is 50 μm with approximately 1 μm (20% of the compressed shell areal density) of the original shell material mixed into the outer 50% of the fuel region. This model provides a picture of the stagnation conditions for the implosion. In the future it will be applied to other implosions to further understand the mix characteristics.

Conclusions

In summary, the implementation of full beam smoothing (1-THz SSD and PS) on OMEGA has produced moderate-convergence-ratio (CR~15) implosions that perform close to 1-D predictions. The primary neutron yield is ~35%–45% of that predicted, while the fuel and shell areal densities are close to their predicted values. When the shell is thickened to reduce the effect of the acceleration-phase RT instability, the perfor-
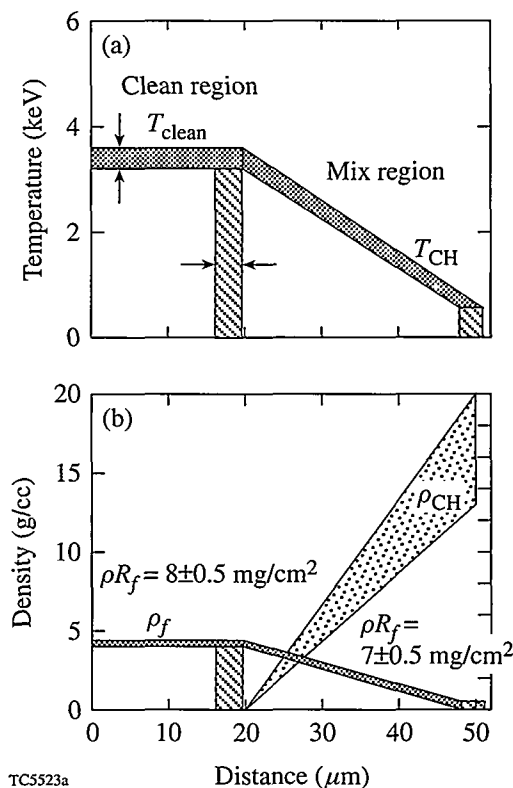

TC5523a

Figure 84.26
Inferred core and fuel–shell mix profiles from the mix model described in the text. The temperature profiles are shown in (a) and the density profiles in (b). The range of the parameters, which are consistent with the experimental observations, is shown by the width of the various parameter bands.

Table 84.III: Comparison of measured and mix-model–predicted implosion parameters for a ~19-μm-thick CH shell (with or without CD layers) filled with 15 atm of D_2 or DT, or ^{3}He for implosions with 1-THz SSD and PS.

Parameter	Measurement	Model (% of expt)
Fuel ρR (mg/cm^2)	15±2	100
T_{ion} (DT) (keV)	4.4±0.4±0.5 (sys)	86
Max. neutron burn rate (n/s)	(9±1) × 10^{20}	110
T_{ion} (D$_2$) (keV)	3.7±0.2±0.5 (sys)	89
Secondary neutron ratio	(2.4±0.4) × 10^{-3}	100
Secondary proton ratio	(1.8±0.3) × 10^{-3}	78
Secondary neutron ratio (D$_2$)	(3.1±0.5) × 10^{-3}	94
D-^{3}He proton yield (^{3}He fill)	(1.3±0.2) × 10^7	66
D$_2$ neutron yield (^{3}He fill)	(8.5±0.4) × 10^8	97

mance improves only slightly, suggesting that single-beam nonuniformities are no longer the dominant determinant of target performance. The stagnation conditions are reproduced by a tightly constrained static mix model.

Future research will address the effect of residual beam-to-beam power imbalances and target-manufacturing nonuniformities as limitations of target performance. Implosions that are less stable during the acceleration phase (e.g., more slowly rising pulses) will be used to further understand the fuel–shell mixing. In addition, x-ray diagnostics will be utilized and their results compared to the static mix model.

Cryogenic-target implosions have begun on the OMEGA laser system. An ignition target on a MJ-class laser system such as the National Ignition Facility will require a shell composed primarily of a frozen DT layer. The OMEGA experiments are energy-scaled versions of ignition implosions with ~100-μm-thick ice layers. The stability properties of these targets due to imprinting are similar to those described in this article. The results described here lead to confidence in the ability to obtain direct-drive ignition on the National Ignition Facility.[9]

ACKNOWLEDGMENT

REFERENCES

1. J. Nuckolls et al., Nature 239, 139 (1972).

2. J. D. Kilkenny, S. G. Glendinning, S. W. Haan, B. A. Hammel, J. D. Lindl, D. Munro, B. A. Remington, S. V. Weber, J. P. Knauer, and C. P. Verdon, Phys. Plasmas 1, 1379 (1994).

3. S. E. Bodner, D. G. Colombant, J. H. Gardner, R. H. Lehmberg, S. P. Obenschain, L. Phillips, A. J. Schmitt, J. D. Sethian, R. L. McCrory, W. Seka, C. P. Verdon, J. P. Knauer, B. B. Afeyan, and H. T. Powell, Phys. Plasmas 5, 1901 (1998).

4. T. J. Kessler, Y. Lin, J. J. Armstrong, and B. Velazquez, in Laser Coherence Control: Technology and Applications, edited by H. T. Powell and T. J. Kessler (SPIE, Bellingham, WA, 1993), Vol. 1870, pp. 95–104.

5. Y. Kato, unpublished notes from work at LLE, 1984.

6. T. R. Boehly, V. A. Smalyuk, D. D. Meyerhofer, J. P. Knauer, D. K. Bradley, R. S. Craxton, M. J. Guardalben, S. Skupsky, and T. J. Kessler, J. Appl. Phys. 85, 3444 (1999).

7. S. Skupsky, R. W. Short, T. Kessler, R. S. Craxton, S. Letzring, and J. M. Soures, J. Appl. Phys. 66, 3456 (1989).

8. R. H. Lehmberg and S. P. Obenschain, Opt. Commun. 46, 27 (1983).

9. P. W. McKenty, V. N. Goncharov, R. P. J. Town, S. Skupsky, R. Betti, and R. L. McCrory, "Analysis of a Direct-Drive Ignition Capsule Designed for the NIF," to be published in Physics of Plasmas.

10. S. V. Weber et al., ICF Quarterly Report, 7, 43, Lawrence Livermore National Laboratory, Livermore, CA, UCRL-LR-105821-97-2 (1997).

11. T. R. Boehly, D. L. Brown, R. S. Craxton, R. L. Keck, J. P. Knauer, J. H. Kelly, T. J. Kessler, S. A. Kumpan, S. J. Loucks, S. A. Letzring, F. J. Marshall, R. L. McCrory, S. F. B. Morse, W. Seka, J. M. Soures, and C. P. Verdon, Opt. Commun. 133, 495 (1997).

12. F. J. Marshall, J. A. Delettrez, V. Yu. Glebov, R. P. J. Town, B. Yaakobi, R. L. Kremens, and M. Cable, Phys. Plasmas 7, 1006 (2000).

13. J. A. Delettrez, V. Yu. Glebov, F. J. Marshall, C. Stoeckl, B. Yaakobi, and D. D. Meyerhofer, Bull. Am. Phys. Soc. 44, 192 (1999).

14. C. P. Verdon, Bull. Am. Phys. Soc. 38, 2010 (1993).

15. M. C. Richardson, P. W. McKenty, F. J. Marshall, C. P. Verdon, J. M. Soures, R. L. McCrory, O. Barnouin, R. S. Craxton, J. Delettrez, R. L. Hutchison, P. A. Jaanimagi, R. Keck, T. Kessler, H. Kim, S. A. Letzring, D. M. Roback, W. Seka, S. Skupsky, B. Yaakobi, S. M. Lane, and S. Prussin, in Laser Interaction and Related Plasma Phenomena, edited by H. Hora and G. H. Miley (Plenum Publishing, New York, 1986), Vol. 7, pp. 421–448.

16. V. N. Goncharov, P. McKenty, S. Skupsky, R. Betti, R. L. McCrory, and C. Cherfils-Clérouin, Phys. Plasmas 7, 5118 (2000).

17. M. D. Cable et al., Phys. Rev. Lett. 73, 2316 (1994).

18. D. K. Bradley, J. A. Delettrez, R. Epstein, R. P. J. Town, C. P. Verdon, B. Yaakobi, S. Regan, F. J. Marshall, T. R. Boehly, J. P. Knauer, D. D. Meyerhofer, V. A. Smalyuk, W. Seka, D. A. Haynes, Jr., M. Gunderson, G. Junkel, C. F. Hooper, Jr., P. M. Bell, T. J. Ognibene, and R. A. Lerche, Phys. Plasmas 5, 1870 (1998).

19. F. J. Marshall, J. A. Delettrez, R. Epstein, V. Yu. Glebov, D. R. Harding, P. W. McKenty, D. D. Meyerhofer, P. B. Radha, W. Seka, S. Skupsky, V. A. Smalyuk, J. M. Soures, C. Stoeckl, R. P. J. Town, B. Yaakobi, C. K. Li, F. H. Séguin, D. G. Hicks, and R. D. Petrasso, Phys. Plasmas 7, 2108 (2000).

20. V. Yu. Glebov, D. D. Meyerhofer, C. Stoeckl, and J. D. Zuegel, "Secondary-Neutron-Yield Measurements by Current-Mode Detectors," to be published in the Review of Scientific Instruments.

21. S. M. Lane et al., Laser Program Annual Report 1986, Lawrence Livermore National Laboratory, Livermore, CA, UCRL-50021-86, 3-100 (1987).

22. F. H. Séguin, C. K. Li, D. G. Hicks, J. A. Frenje, K. M. Green, R. D. Petrasso, J. M. Soures, D. D. Meyerhofer, V. Yu. Glebov, C. Stoeckl, P. B. Radha, S. Roberts, C. Sorce, T. C. Sangster, M. D. Cable, S. Padalino, and K. Fletcher, "Using Secondary Proton Spectra to Study Imploded D$_2$-Filled Capsules at the OMEGA Laser Facility," submitted to Physics of Plasmas.

23. D. G. Hicks, "Charged Particle Spectroscopy: A New Window on Inertial Confinement Fusion," Ph.D. thesis, Massachusetts Institute of Technology, 1999.

24. S. Skupsky and S. Kacenjar, J. Appl. Phys. **52**, 2608 (1981).

25. C. K. Li, D. G. Hicks, F. H. Séguin, J. A. Frenje, K. Green, R. D. Petrasso, D. D. Meyerhofer, J. M. Soures, V. Yu. Glebov, P. B. Radha, S. Skupsky, C. Stoeckl, S. Roberts, and T. C. Sangster, "Study of Direct-Drive, DT-Gas-Filled-Plastic-Capsule Implosions Using Nuclear Diagnostics on OMEGA," submitted to Physics of Plasmas.

26. H. Azechi, M. D. Cable, and R. O. Stapf, Laser Part. Beams **9**, 119 (1991).

27. V. Yu. Glebov, J. A. Delettrez, R. Epstein, P. W. McKenty, F. J. Marshall, D. D. Meyerhofer, P. B. Radha, V. A. Smalyuk, and C. Stoeckl, Bull. Am. Phys. Soc. **44**, 194 (1999).

28. S. Skupsky and R. S. Craxton, Phys. Plasmas **6**, 2157 (1999).

29. P. B. Radha, V. Yu. Glebov, F. J. Marshall, D. D. Meyerhofer, S. P. Regan, W. Seka, S. Skupsky, V. A. Smalyuk, J. M. Soures, C. Stoeckl, B. Yaakobi, and R. D. Petrasso, Bull. Am. Phys. Soc. **45**, 164 (2000).

Secondary-Neutron-Yield Measurements by Current-Mode Detectors

Introduction

The measurement of secondary deuterium–tritium (DT) neutrons from pure-deuterium targets in inertial confinement fusion (ICF) experiments was proposed more than two decades ago[1-3] as a method for determining fuel areal density and demonstrated experimentally more than a decade ago.[4,5]

The secondary neutron yield is typically several orders of magnitude less than the primary yield, necessitating the use of a very sensitive neutron detector. For this application several single-hit detectors consisting of an array of individual scintillator detectors and electronics for detecting the time of flight of the first neutron (single hit) were developed at major laser facilities: LaNSA[6] at Nova, MEDUSA[7] at OMEGA, and MANDALA[8] at GEKKO. MEDUSA saturates on high-yield, direct-drive implosion experiments currently carried out on the 30-kJ, 60-beam OMEGA laser system and is not suitable for future cryogenic capsules experiments on OMEGA. At LLE we have developed several current-mode detectors (e.g., a single scintillator and a photomultiplier tube) for secondary-neutron-yield measurements on current and future OMEGA experiments. This article describes the status of these detectors, including detector design and calibration.

Comparison of Two Mode Detectors

For ICF experiments, single-hit detectors have many advantages (i.e., they are very sensitive and they can measure secondary neutron spectra and ion temperature in addition to secondary yield) but they also have two major disadvantages: First, single-hit detectors are very expensive because of the large number of individual detectors (~1000) and associated electronics. Second, they have a very limited dynamic range, which stems from the principle that an individual detector registers only the first hit. At low yield the single-hit detector is limited by statistical error simply from the number of fired individual detectors. To obtain less than 20% statistical error, 30 or more hits are necessary. If the number of fired individual detectors exceeds 50% of the array elements (500 detectors) at high yield, the single-hit detector is limited by a high number of double hits on a single detector. This effect can be compen-

sated for to a certain extent by statistical analysis, but this so-called "busy correction" can extend the dynamic range by only a factor of 2. Consequently the dynamic range of the single-hit detector is 15 to 30 (with busy correction).

Current-mode detectors, e.g., a single scintillator and a photomultiplier tube connected with a digital oscilloscope, are much cheaper than single-hit detectors. The dynamic range of the current-mode detector is restricted by the linear dynamic range of the photomultiplier and can exceed 1000 for many photomultipliers. The operational range of the current-mode detector can be adjusted by changing location, the high voltage on the photomultiplier, or the scintillator. Since current-mode detectors are relatively cheap, it is possible to create several such detectors—each designed for a different secondary-yield range—and, thus, cover a large range of secondary yields without any change in setup. A disadvantage of the current-mode detectors is the fact that a very high secondary yield is required to measure energy spectra of secondary neutrons.

The dynamic range limitations of the single-hit detectors can be compensated for by modifying the targets—for example, by diluting the D_2 with H_2 or ^3He in the gas mixture to suppress the primary yield. We use such modifications for direct-drive ICF experiments with MEDUSA; however, this reduces the yield of secondary protons, which provide additional ρR information. A proton yield of 5×10^7 or higher, which is well beyond the MEDUSA range, is required to measure secondary proton spectra with a charged-particle spectrometer (CPS).[9] Target modifications are not possible for the cryogenic-target experiments planned on OMEGA, necessitating the development of current-mode detectors for secondary-yield measurements at LLE.

Background for Secondary Neutrons

Several background processes complicate the measurement of secondary neutrons:

1. *Hard x rays.* The hard-x-ray signal from laser–plasma interaction and from the peak compression can be very large

on OMEGA: x-ray energies can reach 500 keV.[10] As a result, the secondary neutron signal appears on the tail of the hard-x-ray signal. This complicates background subtraction for the secondary neutron signal. The hard-x-ray signal can be suppressed by lead shielding the scintillator counter.

2. *Neutron-induced gamma rays from the target chamber wall.* The primary neutrons interact with the target chamber wall and produce gamma rays, which are detected in the scintillator. This gamma-ray signal is several order of magnitudes smaller than the primary neutron signal but larger than the secondary neutron signal. It is practically impossible to suppress this gamma-ray signal by shielding because of its high energy. The timing of the gamma-ray signal depends on the size of the target chamber and the location of the scintillator counter and can be chosen to be before or after the secondary neutron signal.

3. *Neutron-induced gamma rays from the target and other structures.* The interaction of the primary neutrons with the target and other structures (target positioner, other diagnostics, etc.) within the target chamber creates gamma rays. For the current-mode detectors within the target chamber or close to it, these gamma rays may create background for the secondary neutron signal. The amount of background and its arrival time can be measured in ICF experiments that produce high yields with very low areal densities. There is no shielding against these gamma rays, but the location of the detector can be adjusted to move the gamma-ray signal away from the secondary neutron peak. For the current-mode detectors located far from the target chamber these gamma rays are not an issue since they fall between the hard x rays and the gamma rays from the target chamber wall.

Current-Mode Detectors at LLE

At the present time LLE has five current-mode detectors plus MEDUSA to measure secondary neutron yield. Historically, LLE's neutron bang time (NBT) detector was the first current-mode detector used to measure secondary neutron yield. The NBT detector is located inside the OMEGA target chamber in a 1.5-in. reentrant tube. The first NBT channel has a BC-422Q scintillator with 4826-mm^3 volume located 55 cm from the target chamber center (TCC) and a Hamamatsu H5783 photomultiplier connected to a 1.5-GHz LeCroy 9362 scope. The NBT detector is shielded from hard x rays by 1.5 in. of lead in front and 0.5 in. of lead surrounding it. LLE's NBT detector was not originally designed for secondary-yield measurements but has been calibrated against MEDUSA on several low-yield DT shots. An example of a scope trace of the

NBT detector for an indirect-drive DT shot with 3.4×10^7 yield is shown in Fig. 84.27. The DT peak on this scope trace was fit with a Gaussian function and is used for calibration. A scope trace of the NBT detector for a direct-drive DD shot with 8.0×10^{10} primary yield and 1.5×10^8 secondary yield is shown in Fig. 84.28. Figures 84.27 and 84.28 show that a lead thickness of 1.5 in. is not enough to shield from hard x rays on OMEGA. There are a few gamma-ray signals between the secondary-DT-neutron signal and the primary-DD-neutron signal. Because of the uncertainty in the gamma-ray background under the DT peak, the NBT error in the secondary neutron yield is estimated to be 20%. The NBT detector becomes nonlinear for secondary yields above 1.5×10^8, which was observed in comparison with other secondary-yield detectors described below. The NBT detector extends our measurable secondary yield beyond the MEDUSA range; it was used in comparison with the CPS diagnostic to measure secondary yield in direct-drive experiments. But recently another more
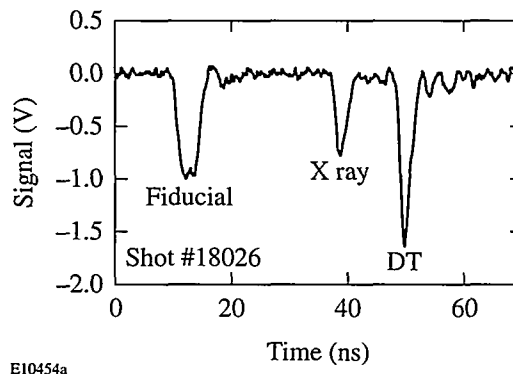

E10454a

Figure 84.27
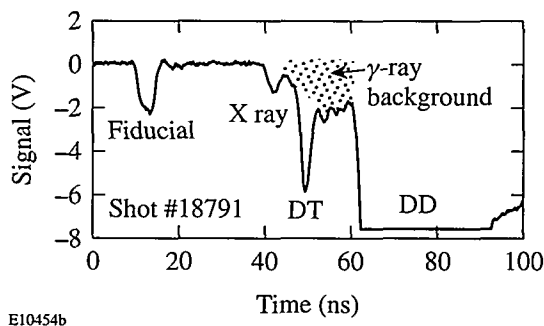Scope trace of the NBT detector signal on a DT shot with a 3.4×10^7 yield.

E10454b

Figure 84.28
Scope trace of the NBT detector signal on a DD shot with a primary DD yield of 8.0×10^{10} and a secondary DT yield of 1.5×10^8.

precise and specially designed current-mode detector, 1.7MNTOF, replaced the NBT detector in secondary-neutron-yield measurements.

The other already existing scintillation counter that can be used as a current-mode detector to measure secondary neutron yield is the 3MLARD detector. It consists of a 17.78-cm-diam, 10-cm-thick scintillator coupled with an XP2020 photomultiplier connected to two channels of the Tektronix 684 scope. The 3MLARD detector is located 285 cm from the TCC and is shielded by a 0.75-in.-thick lead plate in front of the scintillator. An example of a scope trace for the direct-drive DD shot with 6.0×10^9 primary yield and 6.0×10^6 secondary yield is shown in Fig. 84.29. The signals from hard x rays, secondary DT neutrons, gamma rays from the target chamber wall, and primary DD neutrons (saturating the scope) are clearly seen. To measure secondary neutrons from the 3MLARD detector, the secondary neutron signal is integrated. We use in this detector a relatively low signal well below XP2020 saturation. The linearity of the 3MLARD was checked by comparison with other detectors. The 3MLARD detector was calibrated against MEDUSA for the secondary neutron yields; it does not extend MEDUSA's range but instead provides a second, independent measurement of the secondary neutron yield.

The 1.7MNTOF detector was designed specifically for measuring secondary neutron yield. It consists of a 40-mm-diam, 10-mm-thick fast BC 422Q scintillator coupled with a fast (250 ps) Photeck PMT240 microchannel-plate photomultiplier connected to two channels of a Tektronix 684 scope.
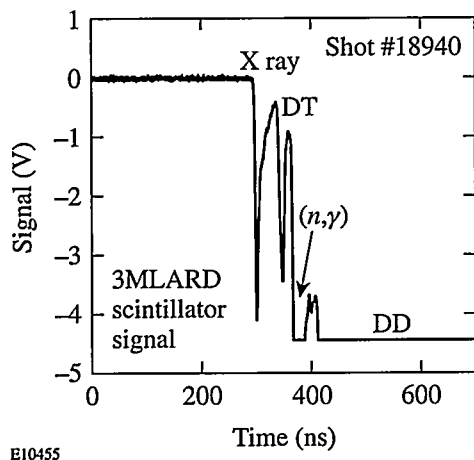
This detector is heavily shielded from hard x rays by 2 in. of lead in front and 1 in. of lead surrounding it. The 1.7MNTOF detector is located on the target chamber wall, 170 cm from the TCC. Because of its location, the 1.7MNTOF has no background from neutron-induced gamma rays from the target chamber wall. A scope trace of the 1.7MNTOF detector for a direct-drive DD shot with 8.5×10^{10} primary yield and 1.5×10^8 secondary yield is shown in Fig. 84.30. The signals from secondary DT neutrons and primary DD neutrons (saturating the scope) can be seen in Fig. 84.30. The hard-x-ray signal is completely eliminated by the lead shielding. From Fig. 84.30 one can estimate a gamma-ray background of a few percent. To measure secondary neutrons from the 1.7MNTOF detector we integrated the signal in the appropriate time window. The 1.7MNTOF detector was calibrated using ride-along copper activation on pure-DD shots; the result of this calibration is shown in Fig. 84.31. The copper activation is a standard diagnostic[11] for 14.1-MeV neutrons in ICF experiments with DT-filled targets. The ^{63}Cu $(n,2n)$ ^{62}Cu reaction cross section has a threshold at 10.9 MeV, and, therefore, copper activation is insensitive to the primary DD neutrons and registers only secondary DT neutrons. The secondary DT neutrons have an energy spectrum from 11.8 MeV to 17.1 MeV. The ^{63}Cu $(n, 2n)$ ^{62}Cu reaction cross section increases as the neutron energy increases.[12] We estimate the error from the uncertainty in the energy spectrum of the secondary neutrons to be less than 10%. This 1.7MNTOF calibration error can be improved if necessary by special low-yield DT calibration shots. The PMT240 photomultiplier is linear up to 25 V into a 50 Ω load. This level of signal has not yet been reached, and one can see from Fig. 84.31 that the 1.7MNTOF detector is linear over the range of yields measured. The PMT240 gain is 6×10^5 and the sensitivity of the 1.7MNTOF detector is about 0.3 pC/neutron.

Figure 84.29

Scope trace of the 3MLARD detector signal on a DD shot with a primary DD yield of 6.0×10^9 and a secondary DT yield 6.0×10^6.
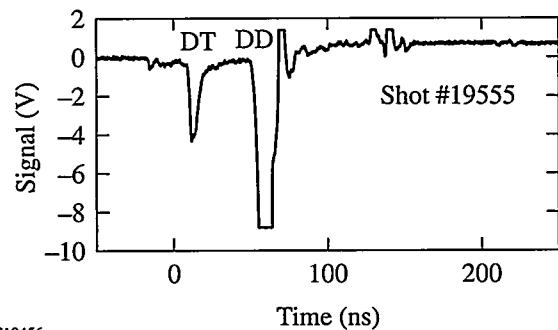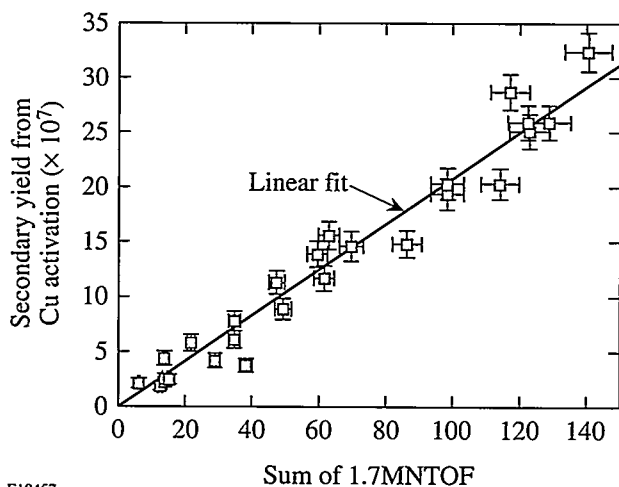
Figure 84.30

Scope trace of the 1.7MNTOF detector signal on a DD shot with a primary DD yield of 8.5×10^{10} and a secondary DT yield of 1.5×10^8.

The 20MLARD and 20M3×3 current-mode detectors are designed to extend the secondary-yield measurements to 5×10^{10}. The 20MLARD counter is identical to the 3MLARD counter. The 20M3×3 detector has a 3-in.-diam, 3-in.-thick scintillator and an XP2020 photomultiplier. Both detectors are located 20 m from the TCC behind the MEDUSA array and are shielded from hard x rays by 1.5-in. MEDUSA lead shielding and MEDUSA itself. Each of the detectors uses two channels of the Tektronix 2440 scope. A scope trace from the 20MLARD detector for the direct-drive DD shot with 1.0×10^{11} primary yield and 3.2×10^{8} secondary yield is shown in Fig. 84.32. The signals from hard x rays, gamma rays from the target chamber wall, secondary DT neutrons, and primary DD neutrons (saturating scope) along with small signals from the scattered neutrons can be seen in Fig. 84.32. A scope trace for the

20M3×3 detector looks very similar, but with lower signals. At this level of the secondary neutron yield there are just a few neutron hits in the 20MLARD and 20M3×3 current-mode detectors. We need higher yield for more precise calibration of these detectors. They can be calibrated with ride-along copper activation on moderate-yield DT shots. These two detectors will be used for the OMEGA cryogenic D_2 shots.[13]

The operating range of secondary yields of MEDUSA and all current-mode detectors at LLE together with the current status of the detectors is summarized in Table 84.IV. The lower limit of the yield range is determined by the neutron hit statistics, and the upper level is set by the measured or expected linearity threshold of the photomultiplier.

E10457

Figure 84.31
Calibration of the 1.7MNTOF detector against copper activation.
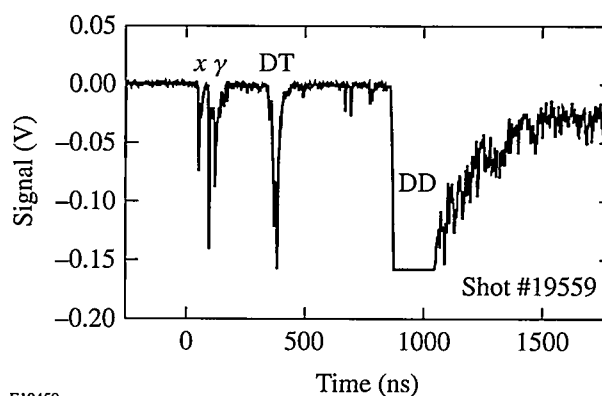
E10458

Figure 84.32
Scope trace of the 20MLARD detector signal on a DD shot with a primary DD yield of 1.0×10^{11} and a secondary DT yield of 3.2×10^8.

Table 84.IV: Detectors for secondary-yield measurements at LLE.

Detector	Yield Range	Current Status
MEDUSA	5.0×10^5 to 1.5×10^7	Calibrated
3MLARD	5.0×10^5 to 1.5×10^7	Calibrated
NBT	1.0×10^7 to 1.5×10^8	Calibrated
1.7MNTOF	1.0×10^7 to 1.0×10^9	Calibrated
20MLARD	2.0×10^8 to 5.0×10^9	Future calibration
20M3×3	5.0×10^8 to 5.0×10^{10}	Future calibration

Conclusions

Single-hit detectors like MEDUSA or LaNSA have a low dynamic range, which is inappropriate for the wide range of secondary yields obtained on OMEGA target shots. Current-mode detectors are an inexpensive alternative to single-hit detectors for measuring secondary neutrons over a wide range of yields. For the current direct-drive ICF experiments and future cryogenic experiments on OMEGA we have developed a set of current-mode detectors to measure secondary neutron yield from 5.0×10^5 to 5.0×10^{10} with an accuracy of 10%. The current-mode detectors have been used in several OMEGA direct-drive implosion experiments to measure secondary yield and will be used on future OMEGA cryogenic D_2 target shots.

REFERENCES

1. E. G. Gamalii *et al.*, JETP Lett. **21**, 70 (1975).

2. T. E. Blue and D. B. Harris, Nucl. Sci. Eng. **77**, 463 (1981).

3. T. E. Blue *et al.*, J. Appl. Phys. **54**, 615 (1983).

4. H. Azechi *et al.*, Appl. Phys. Lett. **49**, 555 (1986).

5. M. D. Cable *et al.*, Bull. Am. Phys. Soc. **31**, 1461 (1986).

6. M. B. Nelson and M. D. Cable, Rev. Sci. Instrum. **63**, 4874 (1992).

7. J. P. Knauer, R. L. Kremens, M. A. Russotto, and S. Tudman, Rev. Sci. Instrum. **66**, 926 (1995).

8. N. Izumi *et al.*, Rev. Sci. Instrum. **70**, 1221 (1999).

9. Laboratory for Laser Energetics LLE Review **83**, 130, NTIS document No. DOE/SF/19460-357 (2000). Copies may be obtained from the National Technical Information Service, Springfield, VA 22161.

10. C. Stoeckl, V. Yu. Glebov, D. D. Meyerhofer, W. Seka, B. Yaakobi, R. P. J. Town, and J. D. Zuegel, "Hard X-Ray Detectors for OMEGA and NIF," to be published in the Review of Scientific Instruments.

11. R. A. Lerche, W. R. McLerran, and G. R. Tripp, *Laser Program Annual Report-1976*, Lawrence Livermore National Laboratory, Livermore, CA, UCRL 50021-76, 3-105 (1976).

12. H. Liskien and A. Paulsen, J. Nucl. Energy **19**, 73 (1965).

13. R. L. McCrory, R. E. Bahr, T. R. Boehly, T. J. B. Collins, R. S. Craxton, J. A. Delettrez, W. R. Donaldson, R. Epstein, V. N. Goncharov, R. Q. Gram, D. R. Harding, P. A. Jaanimagi, R. L. Keck, J. P. Knauer, S. J. Loucks, F. J. Marshall, P. W. McKenty, D. D. Meyerhofer, S. F. B. Morse, O. V. Gotchev, P. B. Radha, S. P. Regan, W. Seka, S. Skupsky, V. A. Smalyuk, J. M. Soures, C. Stoeckl, R. P. J. Town, M. D. Wittman, B. Yaakobi, J. D. Zuegel, R. D. Petrasso, D. G. Hicks, and C. K. Li, in *Inertial Fusion Sciences and Applications 99*, edited by C. Labaune, W. J. Hogan, and K. A. Tanaka (Elsevier, Paris, 2000), pp. 43–53.

Fourier-Space Image Processing for Spherical Experiments on OMEGA

Introduction

Measurements of shell integrity are very important for understanding and quantifying the performance degradation of spherical implosions in inertial confinement fusion (ICF).[1] Such measurements are performed at the peak of compression of the implosion, when maximum density and temperature are achieved. At this time, the hot core and the inner surface of the shell produce strong x-ray emission.[1] This radiation acts to backlight the rest of the shell. Imaging this emission at x-ray energies not absorbed by the shell provides measurements of the shape of this backlighter. Spatial modulations in the image taken at x-ray energies highly absorbed by the shell depend on modulations in both the backlighter emission and the shell's areal density.

The first measurements of shell-areal-density modulations were time integrated over the duration of the peak compression phase (~300 to 400 ps).[2–4] Core images were taken with either a monochromatic pinhole-array x-ray spectrometer[2,3] or a narrow-band filtered pinhole array[4] in targets with Ti-doped layers. The modulations in the cold, or absorbing, part of the shell's areal density $\delta[\rho R](\mathbf{r})$ are related to the modulation in the logarithm of the intensity ratio of two images taken at x-ray energies above (highly absorbing by the shell) and below (weakly absorbing by the shell) the Ti K edge:

$$\delta[\rho R](\mathbf{r}) = \delta\left\{\frac{\ln\left[I_{<K}(\mathbf{r})\right]/I_{>K}(\mathbf{r})}{\left(\mu_{>K} - \mu_{<K}\right)}\right\}, \qquad (1)$$

where $I(\mathbf{r})$ is the intensity in the image, μ is the mass absorption coefficient of Ti, and subscripts $<K$ and $>K$ designate energies just above and just below the Ti K edge, respectively.

The shell opacity and core size can vary significantly during the time of the stagnation phase, therefore time-resolved measurements of shell modulations are important. In this work, images above and below the Ti K edge are captured with a framing camera and recorded on film. The imaging system, composed of the pinhole array, the framing camera, the film, and the digitization process, is fully characterized. Image processing techniques are accomplished in spatial-frequency, or Fourier, space. In the sections that follow: (1) The image formation at all four stages of the imaging system is described along with approximations that enable the modulations in captured images to be related to shell-areal-density non-uniformities. (2) The pinhole camera and framing camera resolution are described. (3) The most important sources of experimental noise are investigated: the statistical x-ray photon noise from the core emission, the framing camera noise, the film noise, and the digitization noise. Methods of noise reduction are discussed. (4) A noise filtering and resolution deconvolution method based on Wiener filtering is formulated, and the experimental uncertainties along with the approximations are discussed. Conclusions are presented in the final section.

Experimental Configuration

The shell-areal-density modulation has been measured for shot 19669 in which a spherical target with an initial diameter of 921 μm, a 19.8-μm-thick shell, and 15-atm-D_2 fill was imploded by 351-nm laser light using the 60-beam OMEGA laser system.[5] A 1-ns square pulse shape with total on-target energy of about 23 kJ was used in this experiment. The target shell had a 2.4-μm-thick, Ti-doped (7.4% by atom) CH layer, which was separated from the inner surface by a 1.1-μm-thick pure-CH layer. The 15.3-μm outer layer was pure CH. Beam-smoothing techniques used during these experiments included distributed phase plates (DPP's)[6] and 0.2-THz smoothing by spectral dispersion (SSD).[7]

The target emission during the peak of compression was imaged by a 6-μm pinhole array (protected by a 203.2-μm Be filter) on a framing camera. The upper two strips of the framing camera were filtered by a 75-μm-thick Ti filter and the lower two strips by a 50-μm-thick Fe filter to image core radiation above (~6.5 keV) and below (~4.9 keV) the Ti K edge, simultaneously. The spectral bandwidth of these two x-ray energy channels was about $\Delta E/E \approx 0.2$ and similar to the time-

integrated measurements.[4] The distance between the target and the pinhole array was 3 cm, and the distance between the pinhole array and the framing camera was 36 cm, resulting in a magnification of 12 (Fig. 84.33). Each image taken with a framing camera had a temporal resolution of ~40 ps.[8] The use of optical fiducial pulses coupled with an electronic monitor of the framing camera produced a frame-timing precision of ~70 ps. The framing-camera output was captured on Kodak T-Max 3200 film, which was then digitized with a Perkin-Elmer microdensitometer (PDS) equipped with a 20-μm-square scanning aperture.

Target at peak of compression   6-μm pinhole array   X-ray framing camera

X rays
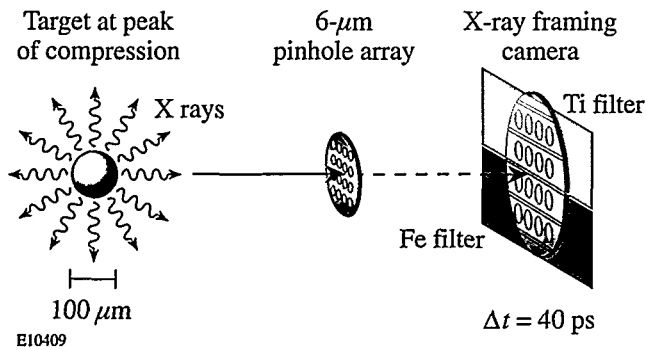
Ti filter

Fe filter

100 μm

E10409

Figure 84.33
Schematic of the framing camera.

Figure 84.34 shows "raw" core images at the peak of compression below [(a), (b)] and above [(c), (d)] the Ti K edge, taken at 2.25 ns [(a), (c)] and at 2.30 ns [(b), (d)]. Notice that the two images within a particular energy channel have similar features that are different from the features in the other energy channel. This indicates that the features seen in the images are not noise and that the difference between the images at different energies is due to modulations in the absorbing shell. The main purpose of this article is to characterize the resolution and noise of all parts of the imaging system in order to distinguish signal from noise and relate detected modulations in the images to modulations in the shell. Figure 84.35 shows a block diagram of the entire detection system, which comprises four major parts: the 6-μm pinhole, the framing camera with a microchannel plate (MCP) and a phosphor plate, the film, and the digitization process. At each stage of the measurement, noise is added to the signal, and the signal with noise is convolved with the point-spread function (PSF) of each component of the system. In the spatial-frequency domain, the spectra of both the signal and the noise are multiplied by a modulation transfer function (MTF, defined here as the Fourier transform of the PSF) of that component of the imaging system.

The x-ray intensity leaving the target at time t and energy E is defined as

$$I_0(E,r,t) = I^{\text{core}}(E,r,t)\,\exp\left[-D_0(r,t)\right], \qquad (2)$$

where r is the spatial coordinate, I_{core} (E,r,t) is the core emission intensity integrated over the core size in the direction of light propagation from the target to the detector, and $D_0(E,r,t) = \mu(E)[\rho R](r,t)$ is the optical depth of the Ti in the shell. The absorption in CH is negligible compared to Ti in this experiment at an energy range from 5 to 7 keV.[4] The light intensity leaving the framing camera and incident on the film is

$$I_{i2}(r,t)$$

$$\sim \int dE \int dr' R_{1,2}(E, r-r', t)\, f_1(E)\mu_{\text{Au}}(E) I_{i0}(E, r', t)$$

$$+ I_{i\text{back}}(r,t), \qquad (3)$$

where the subscript i ($i = a$ or b) corresponds to images taken above and below the Ti K edge, respectively, $R_{1,2}(E,r,t)$ is the

(a)   (b)

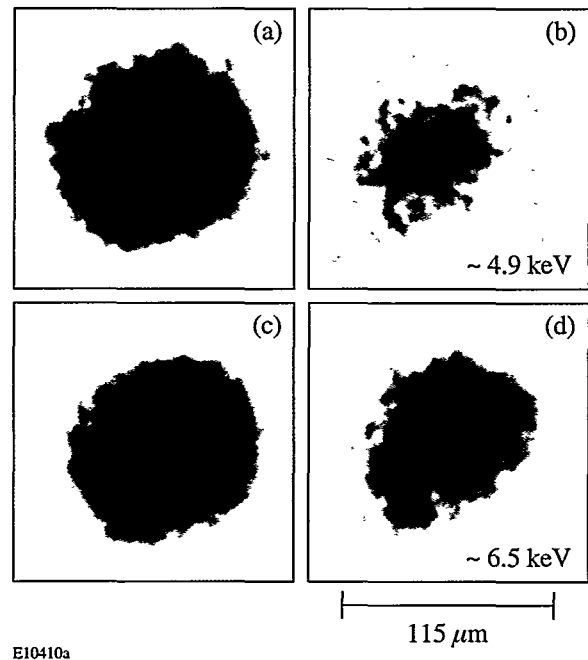~ 4.9 keV

(c)   (d)

~ 6.5 keV

115 μm

E10410a

Figure 84.34
"Raw" core images at the peak of compression below [(a), (b)] and above [(c), (d)] the Ti K edge, taken at 2.25 ns [(a), (c)] and 2.30 ns [(b), (d)].

PSF of the pinhole and framing cameras that is in general a function of the x-ray energy E, $f_i(E)$ is the filter function of the ith energy channel, $\mu_{Au}(E)$ is the mass absorption rate of the gold photocathode (in the MCP), and $I_{iback}(E,\mathbf{r},t)$ is the background intensity for the ith channel. The background intensity is normally slowly varying and comes from hard x rays penetrating directly through the 25-μm-thick Ta substrate in which the pinholes are contained.

The film converts the incident light intensity $I_{i2}(\mathbf{r},t)$ into the film optical density $O_{i3}(\mathbf{r},t)$ according to its sensitivity [or $D\log(H)$] curve W. Convolved with the PSF of the film $R_3(\mathbf{r},t)$, $O_{i3}(\mathbf{r},t)$ is given by

$$O_{i3}(\mathbf{r},t) = \int d\mathbf{r}' R_3(\mathbf{r}-\mathbf{r}') \, W\left\{\log_{10}\left[\int_{t-\tau/2}^{t+\tau/2} dt' I_{i2}(\mathbf{r}',t')\right]\right\}, \quad (4)$$

where $\tau = 40$ ps is the temporal resolution of the framing camera. During film digitization, the optical density $O_{i3}(\mathbf{r},t)$ is convolved with the PSF $R_4(\mathbf{r})$ of the 20-μm-square aperture in the PDS to give the digitized or measured optical density

$$O_{i4}(\mathbf{r},t) = \int d\mathbf{r}' R_4(\mathbf{r}-\mathbf{r}') O_{i3}(\mathbf{r}',t). \quad (5)$$

The optical density of the film, $O_{i4}(\mathbf{r},t)$, is converted to intensity using the inverse film sensitivity W^{-1}; simultaneously the flat background intensity $I_{iback}(\mathbf{r},t)$ can be subtracted from the image because the constant $I_{iback}(\mathbf{r},t)$ is not affected by the convolutions in Eqs. (4) and (5). The measured optical depth $D_{i5}(\mathbf{r},t)$ of the target at a particular energy channel is obtained by taking the natural logarithm of that intensity-converted image,

$$D_{i5}(\mathbf{r},t) = \ln\left\{10^{W^{-1}[O_{i4}(\mathbf{r},t)]} - I_{iback}(\mathbf{r},t)\right\}. \quad (6)$$

Measured shell modulations $d_5(\mathbf{r},t)$ in optical depth are the differences in modulation optical depth of images above and below the Ti K edge,

$$d_5(\mathbf{r},t) = \delta\left[D_{a5}(\mathbf{r},t) - D_{b5}(\mathbf{r},t)\right]. \quad (7)$$

The thin solid line in Fig. 84.36 shows the measured shell modulation spectrum as a function of spatial frequency. This spectrum was obtained by azimuthally averaging the Fourier amplitude of the measured optical-depth-difference images above [$D_{a5}(\mathbf{r},t)$] and below [$D_{b5}(\mathbf{r},t)$] the Ti K edge. Each image was obtained by averaging two images below the K edge [shown in Figs. 84.34(a) and 84.34(b)] $D_{b5}(\mathbf{r},t) = [D_{b5}(\mathbf{r},t_1) + D_{b5}(\mathbf{r},t_2)]/2$, and two images above the K edge [shown in Figs. 84.34(c) and 84.34(d)] $D_{a5}(\mathbf{r},t) = [D_{a5}(\mathbf{r},t_1) + D_{a5}(\mathbf{r},t_2)]/2$. The noise level, shown by a thick solid line in Fig. 84.36, was obtained by analyzing in Fourier space the differences in the two images above [$N_{a5}(\mathbf{r},t)$] and below [$N_{b5}(\mathbf{r},t)$] the K edge, respectively. It was assumed that there was little difference between images taken 50 ps apart. The dotted line represents the film noise, which was obtained by analyzing the same-size area as in the above images (1.4 mm × 1.4 mm) of uniformly exposed (optical density ~1) film.
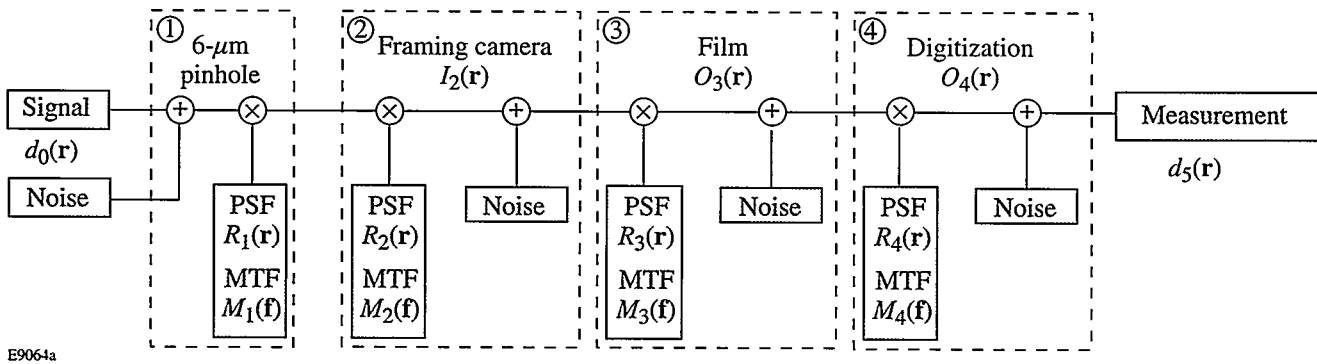

E9064a

Figure 84.35

Block diagram of the experimental detection system, which comprises four major parts: a 6-μm pinhole, the framing camera, the film, and the digitization. At each stage of measurement, noise is added to the signal, and the signal with noise is convolved with the PSF. Variables $d_0^{sh}(\mathbf{r},t)$ and $d_5(\mathbf{r},t)$ are the optical-depth modulations in the shell and measured on a film, respectively. $I_2(\mathbf{r},t)$ is the light intensity in the framing camera's output. $O_3(\mathbf{r},t)$ and $O_4(\mathbf{r},t)$ are the optical density of the film, before and after digitization, respectively.
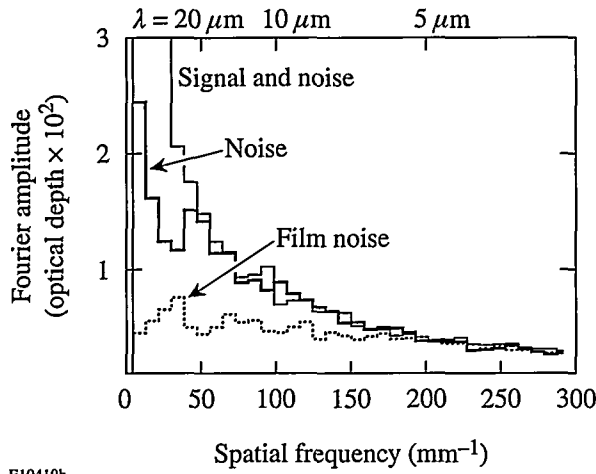
E10410b

Figure 84.36
Azimuthally averaged Fourier amplitude as a function of spatial frequency for the signal with noise (thin solid line), the noise (thick solid line) of the measured optical-depth modulations from the images in Fig. 84.34, and the film noise (dotted line).

One advantage of performing noise analysis in spatial-frequency space is the possibility of determining the origin of the noise from the shape of the noise spectrum. At each stage of the imaging system, the spectra of both the signal and the noise are multiplied by the MTF of that particular part of the system. Therefore, an initially flat noise spectrum—for example, the statistical x-ray photon noise from the core emission—will follow the shape of the pinhole camera's MTF after being imaged by the pinhole camera. Figure 84.36 shows that the film noise dominates at high spatial frequencies (>200 mm^{-1}), which slowly falls as a function of spatial frequency following the MTF of the 20-μm-square scanning aperture. At lower spatial frequencies (<200 mm^{-1}), the noise falls more steeply and, as will be shown later, is dominated by photon statistics from the core emission in this spectral region.

To recover the target optical depth $D_0(E,\mathbf{r},t)$ from the measured optical depth $d_5(\mathbf{r},t)$ it is, in general, necessary to work backward through all four stages of the imaging system, compensating for noise and system response (PSF). Additional complications arise during signal conversions from optical density to intensity and finally to the shell's optical depth. These conversions are nonlinear [see Eqs. (2), (4), and (6)]; therefore, additional noise is generated from the coupling of signal and noise during each conversion. However, if the modulations in the target's optical depth are small (which is the case in our experiment), the entire imaging system may be considered linear. This greatly simplifies the relation between the measured and target optical depths and enables a direct

linear relationship between them. This method is justified when all of the nonlinear effects are small and may not be detected within system noise.

If the shell's optical-depth modulations are small for the energy channels above and below the Ti K edge, the core intensity consists of the smooth envelope and small modulations and has the same spatial and temporal structure for both the above- and below-K-edge energy channels, then can be summarized as

$$D_{i0}^{sh}(\mathbf{r},t) = D_i^{sh}(t) + d_{i0}^{sh}(\mathbf{r},t), \tag{8}$$

$$I^{core}(\mathbf{r},t) \sim I^{env}(\mathbf{r},t)\exp\left[-d_0^{core}(\mathbf{r},t)\right], \tag{9}$$

where $D_{i0}^{sh}(\mathbf{r},t)$ is the total shell optical depth;

$$d_{i0}^{sh}(\mathbf{r},t) = \mu_i \delta[\rho R](\mathbf{r},t) < 1$$

and $d_0^{core}(\mathbf{r},t) < 1$ are the optical-depth modulations of the shell and the core, respectively; $I^{env}(\mathbf{r},t)$ is the slowly varying envelope of the core emission; and μ_i is the spectrally weighed mass absorption rate of cold Ti at a particular energy channel [it is determined by the filter function $f_i(E)$ and core emission spectrum $I^{core}(E,\mathbf{r},t)$]. The modulation in the shell's optical depth is simply the difference in optical-depth modulations above and below the K edge:

$$d_0^{sh}(\mathbf{r},t) = d_{a0}^{sh}(\mathbf{r},t) - d_{b0}^{sh}(\mathbf{r},t). \tag{10}$$

Since the shell and core modulations are small, it is possible to expand the exponential functions in Eqs. (2) and (9) into Taylor series; retaining only zeroth and first orders in these expansions, we have the following expression for Eq. (3):

$$I_{i2}(\mathbf{r},t) \sim I^{env}(\mathbf{r},t)\left\{2C - \left[\int d\mathbf{r}' R_{1,2}(\mathbf{r}-\mathbf{r}',t) d_{i0}^{sh}(\mathbf{r}',t)\right.\right.$$

$$\left.\left. + \int d\mathbf{r}' R_{1,2}(\mathbf{r}-\mathbf{r}',t) d_0^{core}(\mathbf{r}',t)\right]\right\}, \tag{11}$$

where $C = \int d\mathbf{r} R_{1,2}(\mathbf{r},t)$ is a normalization constant and the background intensity is assumed to be zero, $I_{iback}(\mathbf{r},t) = 0$. T-MAX 3200 film has a constant MTF at least up to a spatial frequency of ~50 mm^{-1}, the highest spatial frequency considered in the experiment, so the PSF of the film is set to the delta function $\delta(\mathbf{r})$. Since only the "linear" part of the film sensitivity [$D\log(H)$] curve is used, the modulations in measured optical

depth are linearly related to the optical-depth modulations in the target:

$$d_{i5}(\mathbf{r},t) = \int d\mathbf{r}' R_{\text{sys}}(\mathbf{r}-\mathbf{r}',t) d_0^{\text{sh}}(\mathbf{r}',t)$$

$$+ \int d\mathbf{r}' R_{\text{sys}}(\mathbf{r}-\mathbf{r}',t) d_0^{\text{core}}(\mathbf{r},t), \qquad (12)$$

where $R_{\text{sys}}(\mathbf{r},t)$ is the PSF of the entire system. It is normalized, $\int d\mathbf{r} R_{\text{sys}}(\mathbf{r},t) = 1$, and proportional to the convolution of PSF's of the pinhole camera, the framing camera, and the digitizing aperture of the densitometer. In frequency space, the system MTF is the product of the MTF's of each of these components. Equation (12) was obtained by substituting Eq. (11) into Eqs. (4)–(6) and retaining only the zeroth-order and first-order terms of the Taylor series expansion of the logarithm function. Subtracting the optical-depth images above and below the K edge, the measured modulation in the cold-shell optical depth is given by

$$d_5(\mathbf{r},t) = d_{a5}(\mathbf{r},t) - d_{b5}(\mathbf{r},t)$$

$$= \int d\mathbf{r}' R_{\text{sys}}(\mathbf{r}-\mathbf{r}',t) d_0^{\text{sh}}(\mathbf{r}',t). \qquad (13)$$

The measured optical-depth modulations calculated from images above and below the Ti K edge are linearly related to the shell optical-depth modulations if these modulations are small. As mentioned earlier in this section, the core intensity $I^{\text{core}}(\mathbf{r},t)$ has the same spatial and temporal structure for both the above- and below-K-edge energy channels. This assumption was experimentally confirmed in time-integrated experiments with pure-CH shells[4] and was used to derive Eq. (13) for time-resolved imaging.

In summary, approximations of the system performance have been used to find a straightforward relationship between the measured optical-depth modulations and the cold-shell areal-density modulations. Equation (13) has been derived by assuming that the shell's optical-depth modulations are small compared to unity. Since Eq. (13) is a linear approximation, it does not treat the generation of harmonics and coupling of modes produced by system nonlinearities. These nonlinearities have been simulated for amplitudes of modulations similar to that in data shown in Fig. 84.34, and the nonlinear effects were found to be negligible compared to the system noise.

System Resolution

The system resolution is determined from the point-spread function (PSF) in real space or the modulation transfer function (MTF) in spatial-frequency space, which is defined in this article as the Fourier transform of the PSF. The system MTF is the product of the MTF's of each of these components: the pinhole camera, the 20-μm-square scanning aperture, and the framing camera. The first two are determined from calculations based on geometry and spectral energy.

The digitizing PSF is proportional to $\Delta x = 20$-μm-square aperture; therefore, the MTF, which is the Fourier transform of the aperture, is given by[9]

$$M_{\text{dig}}(f_x, f_y) = \left[\frac{\sin(\pi \Delta x f_x)}{\pi \Delta x f_x} \right]\left[\frac{\sin(\pi \Delta x f_y)}{\pi \Delta x f_y} \right], \qquad (14)$$

where f_x, f_y are the spatial-frequency components of the vector $\mathbf{f}$.

The MTF of the framing camera was determined by measuring the camera response to an edge placed ~ 1 mm in front of the camera and backlit by x rays. This output of the framing camera was measured with a charge-coupled-device (CCD) camera[10] with 9-μm-square pixel size. The edge was close enough to the framing camera so that diffraction effects can be neglected. The dashed line in Fig. 84.37(a) represents the light intensity incident on the edge. The thin solid line is the measured light intensity propagated through the system (and averaged in the direction parallel to the edge), and the thick solid line is the fit to experimental data assuming the framing camera MTF as a two-Gaussian function,[11]

$$M_{\text{fc}}(f) = \alpha_1 \exp\left[-(\sigma_1 f)^2\right] + \alpha_2 \exp\left[-(\sigma_2 f)^2\right], \qquad (15)$$

where $\alpha_1 = 0.89 \pm 0.01$, $\alpha_2 = 0.22 \pm 0.01$, $\sigma_1 = 105.4 \pm 0.4\,\mu$m, and $\sigma_2 = 2356.8 \pm 0.4\,\mu$m. The measured MTF of the framing camera is shown in Fig. 84.37(b). This MTF is similar to that measured in the earlier experiments.[12] The only difference is that CCD measurements are more sensitive than film measurements, and it was possible to detect the long-scale-length scattering of photons and electrons between the phosphor and microchannel plates.[13] This scatter is given by the second term in Eq. (15), and it reduces the MCP resolution by about 10% at low spatial frequencies <5 mm^{-1}.

The resolution of the pinhole camera was calculated using the Fresnel approximation (which should work well for the parameters of our imaging system) for the light propagation.[9] The pinhole PSF is given by the following equation:[9]

$$P_{\mathrm{ph}}\left(x, y, z_2\right) \sim \frac{1}{\left(\lambda^4 z_1^2 z_2^2\right)}$$

$$\bullet \left| \iint dx' dy' \mathrm{circ}\left(\frac{x', y'}{d}\right) \exp\left[-\frac{i\pi}{\lambda}\left(x'^2 + y'^2\right)\left(\frac{1}{z_1} + \frac{1}{z_2}\right)\right] \right.$$

$$\left. \exp\left[\frac{2i\pi}{(\lambda z_2)}(xx' + yy')\right]\right|^2, \tag{16}$$

where circ$(x, y/d)$ is the circular aperture function with diameter d, λ is the x-ray wavelength, and z_1, z_2 are the distances from the object to the pinhole and the pinhole to the image, respectively. Because the pinhole size d in the pinhole array was varying typically within a specification of 0.5 μm, $d =$ 6±0.5 μm, it was important that the pinhole-size variation not affect the pinhole resolution. Figure 84.38(a) shows the calcu-

lated pinhole MTF's of 5-, 6-, and 7-μm-diam pinholes at an x-ray energy of 5 keV. Even though the MTF's are different at high spatial frequencies, there is little difference (<5%) for all three MTF's at low spatial frequencies (<50 mm^{-1}), where all detected above the noise signal are located (see Fig. 84.36). Figure 84.38(b) shows that calculated MTF's of 6-μm pinholes at 5 and 7 keV are very close (with differences also <5%) at low spatial frequencies (<50 mm^{-1}). The pinhole depth's effect on the resolution was found to be negligible for the experimental conditions. This confirms the assumption made in the previous section that the system resolution is the same for images above and below the K edge.

System Noise

To determine the origin of noise shown by the dotted line in Fig. 84.36, the noise of the entire imaging system and in its individual parts was characterized by Fourier space analysis of uniformly exposed areas with the same box size (1.4 mm × 1.4 mm in image plane) as the data in Fig. 84.36. To measure noise in the entire system, images of a large area (~1 mm in diameter) of a uranium backlighter were used. The backlighter target was illuminated by 12 overlapping beams at an intensity of ~10^{14} W/cm^2, in a configuration similar to the noise measurements for planar-foil experiments.[12] Since the backlighter
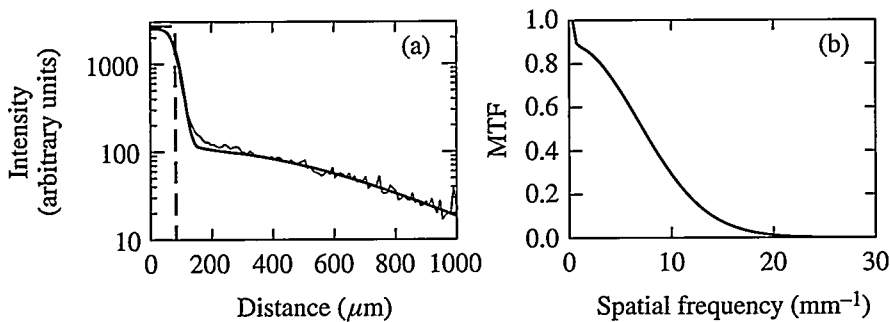

E10416

Figure 84.37

The framing camera resolution. The dashed line in (a) represents the light intensity incident on the edge. The thin solid line is the measured light intensity propagated through the system (and averaged in the direction parallel to the edge). The thick solid line is the fit to experimental data assuming the framing camera MTF shown in (b).
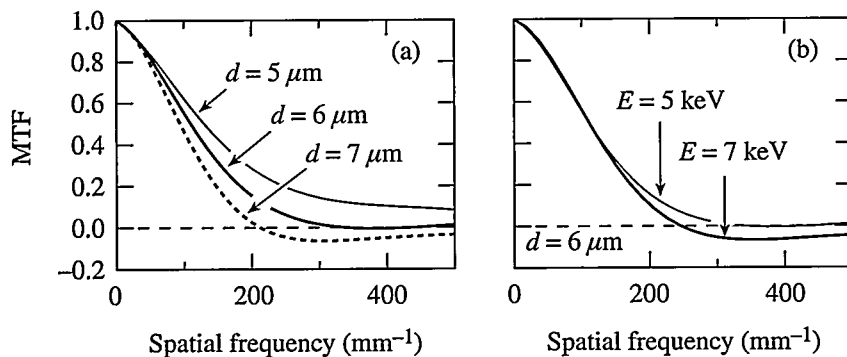

E10415

Figure 84.38

The resolution of the pinhole camera. (a) The calculated pinhole MTF's of 5-, 6-, and 7-μm-diam pinholes at an x-ray energy of 5 keV. (b) The calculated 6-μm pinhole MTF's at x-ray energies of 5 and 7 keV.

emission was smooth, the nonuniformities in the images were considered to be caused by noise. A 25-μm "strip" of CH_2 was placed between the backlighter and the pinhole to attenuate the backlighter emission by a factor of ~8 at 1.3 keV (see Fig. 84.39). The filters in front of the framing camera were also varied to change the exposure levels by a predetermined amount.
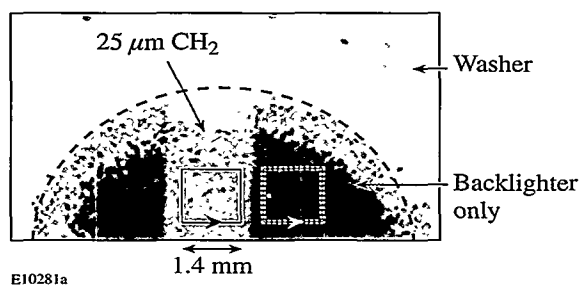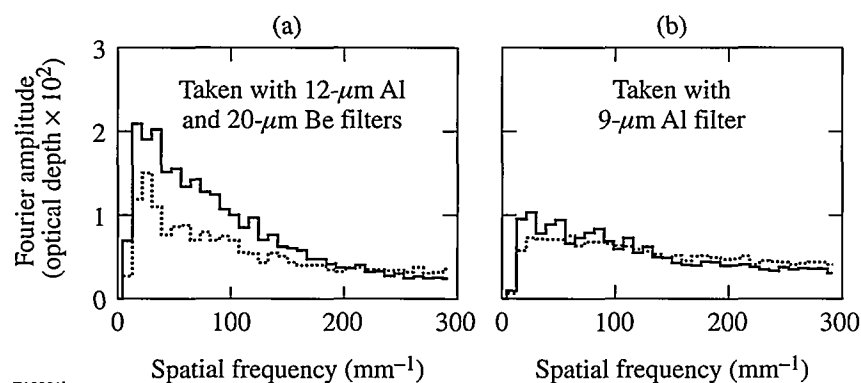

E10281a

Figure 84.39
The image of the 25-μm CH_2 "strip" target taken with a U backlighter. Two boxes in the strip and backlighter-only regions represent image areas taken for analysis.

Figure 84.40 shows the azimuthally averaged Fourier amplitudes of the optical depth for two square regions with 1.4 mm in image plane, through (dotted lines) and around (solid lines) the strip. The total filtration in front of the framing camera included 20 μm of Be and 12 μm of Al for the data shown in Fig. 84.40(a) and 9 μm of Al for the data in Fig. 84.40(b). As a result of the filters, a relatively narrow band ($\Delta E/E \approx 0.2$) of x rays around 1.3 keV is used for radiography. At high spatial frequencies ($f > 200$ mm^{-1}), the noise spectrum is nearly constant, indicative of the noise from film and digitization. At lower spatial frequencies the noise amplitudes depend on the MTF's of pinhole and framing cameras and have contributions from both the photon statistical noise of the

backlighter x rays and framing camera noise. It will be shown later in this section that the amplitude of framing camera noise is proportional to the output intensity. This means that in optical-depth space the framing camera noise is independent of the intensity (because the optical depth is the logarithm of the intensity), and it is expected to be the same in the areas through and around the strip. In optical-depth space, the photon noise of backlighter x rays is inversely proportional to the square root of the number of photons.[12] There is more photon noise in the region of the strip with fewer x-ray photons than in the region out of the strip [shown in Fig. 84.40(a)]. The noise falls even more with decreasing amount of filtration reaching the film noise level. This indicates that photon noise is dominant in the low-spatial-frequency region of the data shown in Figs. 84.36 and 84.40.

Figure 84.41 shows spectra of digitizing noise and the film noise in optical density versus spatial frequency. The digitizing noise [Fig. 84.41(a)] has been measured by digitizing uniform light exposures (with no film) using six different filters with transmissions of 0.5, 1.1, 1.5, 1.9, 2.4, and 2.9 optical density. To measure the film noise, the film was exposed to uniform irradiation at five different exposure levels of 0.5, 1.1, 1.7, 2.9, and 3.8 optical density [Fig. 84.41(b)]. A 5-μm-square digitizing aperture was used, and the analysis box size was the same as for all other images in this article: 1.4 mm square in image plane. The digitizing noise spectra are flat functions of spatial frequency, as expected, because the digitizing noise is added to the measurement after the effect of the system resolution. The noise amplitudes increase at higher optical-density levels when light transmission through the filter decreases. The film noise, which is about ten times higher than the digitizing noise (as evident from Fig. 84.41), also depends weakly on the exposure level. At high spatial frequencies its amplitude decreases gradually, as expected, since they are multiplied by the 5-μm-square digitizing aperture MTF given by Eq. (14).

E10281b

Figure 84.40
System noise. The measured noise spectra in areas through (dotted lines) and around (solid lines) the 25-μm-CH_2 strip target taken with (a) 20-μm-Be and 12-μm-Al filters, and (b) a 9-μm-Al filter.

Framing camera noise could be measured once the film was replaced by the CCD camera,[10] which allowed lower noise amplitudes to be detected. Figure 84.42(a) shows noise spectra of framing camera outputs taken with film and with the CCD. The framing camera was uniformly illuminated by x rays during two similar flat-field exposures (one exposure was taken with film, the other with a CCD). The incident x-ray flux was kept high to minimize the photon noise of incident x rays. The film exposure was converted to intensity in order to compare it with CCD data, which measures intensity, not optical density. Film data were digitized with a 10-μm-square digitizing aperture; the CCD's pixels were 9 μm. Film noise dominates framing camera noise at high spatial frequencies, and both noise levels are comparable at low spatial frequencies. The spectral shape of the framing camera noise follows the MTF (shown in Fig. 84.37).

Figure 84.42(b) shows the dependence of the framing camera noise on output intensity. By varying the gain of the framing camera, three different areas (with a typical square box of 1.4 mm) had average exposure levels of 200, 650, and 3600 counts measured with the CCD during one of the flat-field exposures. The noise spectra corresponding to these data are shown by three lines in Fig. 84.42(b). The noise levels scale as the average exposure levels on the CCD, indicating that the framing camera noise is proportional to the output intensity. This noise is dominated by the gain variations inside the MCP, which are reproducible from shot to shot. Figure 84.43 shows two images of the same area of the framing camera outputs taken during two different flat-field exposures. Images are virtually identical. Since this noise is reproducible, it can be removed from the images by subtracting two images. In Fig. 84.44 the noise spectra of these two images is shown by thick and thin solid lines. The dashed line represents the noise from the difference of two images. The framing camera noise is reduced by a factor of 4 at low spatial frequencies. Such noise

reduction can be useful in image processing when the framing camera noise is dominant (with the CCD).

In summary, the photon statistics of x rays are the dominant source of noise in our measurements. By increasing the inci-
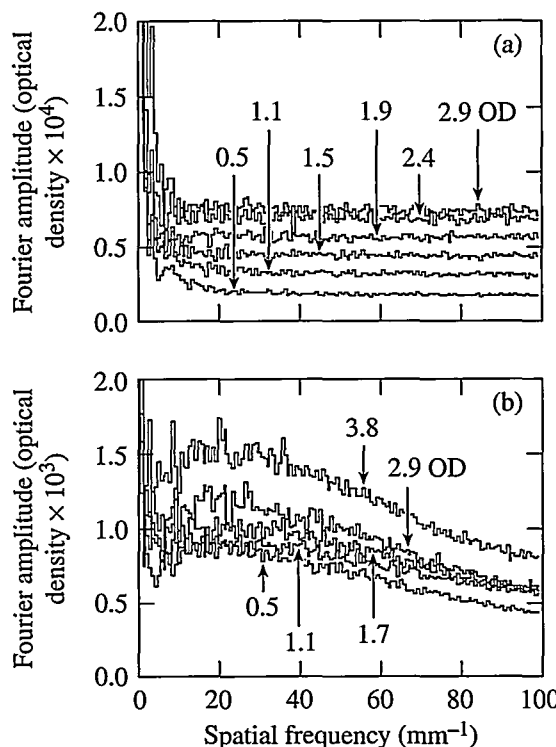
Figure 84.41
Fourier spectra of digitizing and film noise versus spatial frequency. (a) The digitizing noise measured by digitizing uniform light exposures (with no film) using six different filters with transmissions of 0.5, 1.1, 1.5, 1.9, 2.4, and 2.9 optical density. (b) The film noise measured by digitizing uniform film exposures at five different exposure levels of 0.5, 1.1, 1.7, 2.9, and 3.8 optical density.
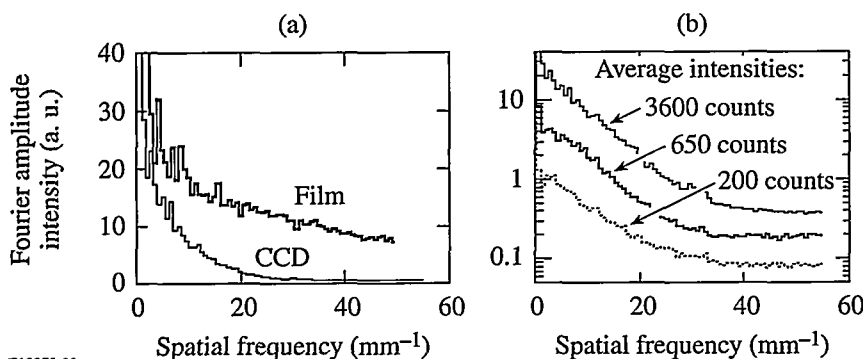
Figure 84.42
The framing camera noise. (a) The comparison of framing camera noise spectra taken with film and with a CCD. (b) The framing camera noise at different output intensities of 200, 650, and 3600 counts taken during a flat-field exposure with a CCD.

dent photon flux it was possible to reduce the noise to the levels where the framing camera and film noise became important. In this situation, an additional noise reduction was possible when the film was replaced by the CCD camera, and the framing camera noise was reduced by removing the shot-to-shot repeatable structure in the framing camera output.

Wiener Filtering

Using the measured system resolution and noise, it is possible not only to distinguish signal from noise in Fig. 84.36 but also to reduce it and deconvolve the resolution from the data detected above the noise. Such image processing is

Shot 17110   Shot 17112

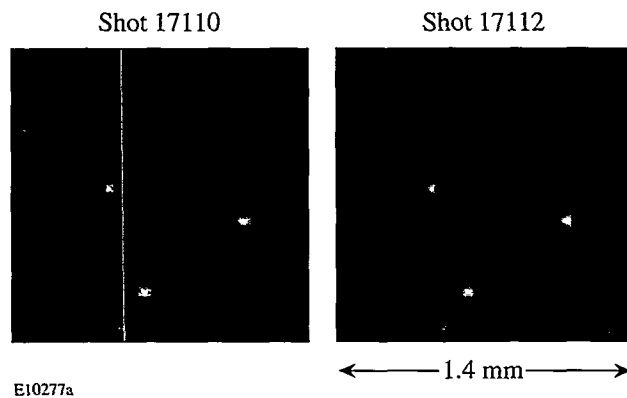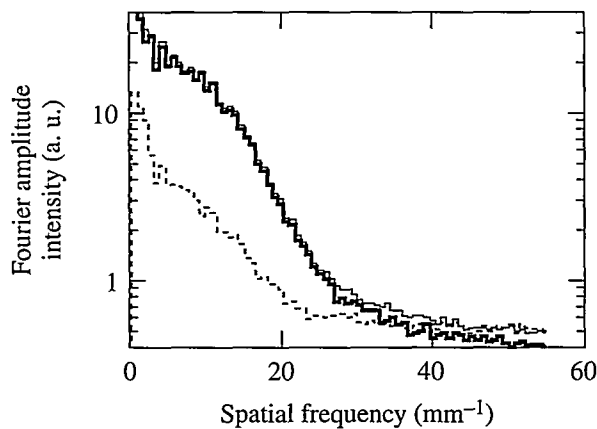$\longleftarrow$ 1.4 mm $\longrightarrow$

E10277a

Figure 84.43
Two images of the same area of the framing camera outputs taken during two different flat-field exposures with a CCD. The images are nearly identical.


E10277b

Figure 84.44
Reduction of the framing camera noise. The noise spectra of two images from Fig. 84.43 shown by thick and thin solid lines. The dashed line represents noise from the difference of two images showing that framing camera noise can be reduced by a factor of 4 at low spatial frequencies.

possible with Wiener filtering in spatial-frequency space. If $C(f)$ is the signal plus noise measured by the system (thin solid line in Fig. 84.36), $C(f) = S(f) + N(f)$, then the restored signal $R(f)$ is[14]

$$R(f) = \frac{C(f)}{M_{sys}(f)} \cdot \frac{|S(f)|^2}{|S(f)|^2 + |N_{avg}(f)|^2}, \qquad (17)$$

where $M_{sys}(f)$ is total system MTF, which is the product of the 6-μm pinhole camera MTF (Fig. 84.38), the framing camera MTF [Fig. 84.37(b) and Eq. (15)], and the 20-μm-square digitizing aperture MTF [Eq. (14)]. The last two MTF's are applied assuming a system magnification of 12. The term $|N_{avg}(f)|$ is the average noise spectrum (the dashed line in Fig. 84.36). During Wiener filtering the amplitudes that have $|C(f)| < 1.5 |N_{avg}(f)|$ plus all amplitudes with spatial frequencies >50 mm^{-1} (this corresponds to wavelengths shorter than 20 μm) were filtered because the noise is dominant there. For the rest of the spectrum, it was assumed that the unknown variable $S(f)$ can be obtained by subtracting the noise in quadrature from the measured signal plus noise, $|S(f)|^2 = |C(f)|^2 - |N_{avg}(f)|^2$.

Figure 84.45 shows the result of such image processing, the image of the shell's optical-depth modulations. The level of shell modulations is similar to the time-integrated measurements,[4] which have detected ~20% perturbations in cold-shell areal density. The errors in determining these modulations, besides the system noise, include the uncertainty in the system

115 μm
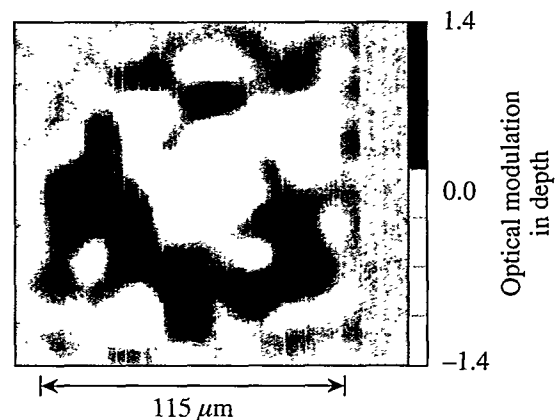
Shot 19669
E10417

Figure 84.45
The Wiener-filtered image of the shell's optical-depth modulations.

212

MTF (which was about 5%) and the uncertainty in linearization of the nonlinear imaging system. This error was estimated by calculating the deviation of the sinusoidal shell modulation with an amplitude of 0.5 OD imaged by the system using Eqs. (2)–(7) without approximation and by using a linear approximation [Eq. (13)]. This calculated deviation is of the order of ~6%.

Conclusions

An imaging system based on the pinhole camera, framing camera, film, and digitization was characterized. This system has been used in spherical implosion experiments to measure shell integrity. Hot-core emission, which was used as a backlighter for the cold shell, was imaged at x-ray energies above and below the Ti K edge. The difference between the two images was related to perturbations in the cold, or absorbing, part of the shell. Based on the measured resolution and noise, a Wiener filter has been formulated that reduces noise, compensates for detector resolution, and facilitates measurement of shell nonuniformities.

ACKNOWLEDGMENT

REFERENCES

1. D. K. Bradley, J. A. Delettrez, R. Epstein, R. P. J. Town, C. P. Verdon, B. Yaakobi, S. Regan, F. J. Marshall, T. R. Boehly, J. P. Knauer, D. D. Meyerhofer, V. A. Smalyuk, W. Seka, D. A. Haynes, Jr., M. Gunderson, G. Junkel, C. F. Hooper, Jr., P. M. Bell, T. J. Ognibene, and R. A. Lerche, Phys. Plasmas 5, 1870 (1998).

2. B. Yaakobi, V. A. Smalyuk, J. A. Delettrez, R. P. J. Town, F. J. Marshall, V. Yu. Glebov, R. D. Petrasso, J. M. Soures, D. D. Meyerhofer, and W. Seka, in *Inertial Fusion Sciences and Applications 99*, edited by C. Labaune, W. J. Hogan, and K. A. Tanaka (Elsevier, Paris, 2000), pp. 115–121.

3. B. Yaakobi, V. A. Smalyuk, J. A. Delettrez, F. J. Marshall, D. D. Meyerhofer, and W. Seka, Phys. Plasmas 7, 3727 (2000).

4. V. A. Smalyuk, B. Yaakobi, F. J. Marshall, and D. D. Meyerhofer, in *Atomic Processes in Plasmas: Twelfth Topical Conference*, edited by R. C. Mancini and R. A. Phaneuf (American Institute of Physics, New York, 2000), pp. 15–24.

5. T. R. Boehly, D. L. Brown, R. S. Craxton, R. L. Keck, J. P. Knauer, J. H. Kelly, T. J. Kessler, S. A. Kumpan, S. J. Loucks, S. A. Letzring, F. J. Marshall, R. L. McCrory, S. F. B. Morse, W. Seka, J. M. Soures, and C. P. Verdon, Opt. Commun. 133, 495 (1997).

6. Y. Lin, T. J. Kessler, and G. N. Lawrence, Opt. Lett. 20, 764 (1995).

7. S. Skupsky, R. W. Short, T. Kessler, R. S. Craxton, S. Letzring, and J. M. Soures, J. Appl. Phys. 66, 3456 (1989).

8. D. K. Bradley, P. M. Bell, O. L. Landen, J. D. Kilkenny, and J. Oertel, Rev. Sci. Instrum. 66, 716 (1995).

9. G. O. Reynolds *et al.*, *The New Physical Optics Notebook: Tutorials in Fourier Optics* (SPIE Optical Engineering Press, Bellingham, WA, 1989).

10. R. E. Turner *et al.*, "Comparison of CCD versus Film Readouts for Gated MCP Cameras," to be published in the Review of Scientific Instruments.

11. H. F. Robey, K. S. Budil, and B. A. Remington, Rev. Sci. Instrum. 68, 792 (1997).

12. V. A. Smalyuk, T. R. Boehly, D. K. Bradley, J. P. Knauer, and D. D. Meyerhofer, Rev. Sci. Instrum. 70, 647 (1999).

13. J. D. Wiedwald *et al.*, in *Ultrahigh- and High-Speed Photography, Videography, Photonics, and Velocimetry '90*, edited by L. L. Shaw, P. A. Jaanimagi, and B. T. Neyer (SPIE, Bellingham, WA, 1990), Vol. 1346, pp. 449–455.

14. W. H. Press *et al.*, *Numerical Recipes in FORTRAN: The Art of Scientific Computing*, 2nd ed. (Cambridge University Press, Cambridge, England, 1992), pp. 701–715.

LLE's Summer High School Research Program

During the summer of 2000, 14 students from Rochester-area high schools participated in the Laboratory for Laser Energetics' Summer High School Research Program. The goal of this program is to excite a group of high school students about careers in the areas of science and technology by exposing them to research in a state-of-the-art environment. Too often, students are exposed to "research" only through classroom laboratories, which have prescribed procedures and predictable results. In LLE's summer program, the students experience many of the trials, tribulations, and rewards of scientific research. By participating in research in a real environment, the students often become more excited about careers in science and technology. In addition, LLE gains from the contributions of the many highly talented students who are attracted to the program.

The students spent most of their time working on their individual research projects with members of LLE's technical staff. The projects were related to current research activities at LLE and covered a broad range of areas of interest including laser modeling and characterization, diagnostic development, hydrodynamics modeling, liquid crystal chemistry, superconductors, optical coatings, laser damage, and the development of a novel laser glass (see Table 84.V).

The students attended weekly seminars on technical topics associated with LLE's research. Topics this year included lasers, fusion, holography, optical materials, nonlinear optics, the OMEGA Cryogenic Target System, and scientific ethics. The students also received safety training, learned how to give scientific presentations, and were introduced to LLE's resources, especially the computational facilities.

The program culminated with the High School Student Summer Research Symposium on 23 August at which the students presented the results of their research to an audience including parents, teachers, and LLE staff. The students' written reports will be bound into a permanent record of their work that can be cited in scientific publications. These reports are available by contacting LLE.

One hundred and seventeen high school students have now participated in the program since it began in 1989. The students this year were selected from approximately 70 applicants.

In 1997, LLE added a new component to its high school outreach activities: an annual award to an Inspirational Science Teacher. This award honors teachers who have inspired High School Program participants in the areas of science, mathematics, and technology and includes a $1000 cash prize. Teachers are nominated by alumni of the High School Program. Mr. James Shannon of Pittsford Mendon High School was the recipient of LLE's 2000 William D. Ryan Inspirational Teacher Award. Mr. Shannon, a chemistry teacher, was nominated by three alumni of the Research Program—Mr. Chen-Lin Lee (participant 1994), Mr. Steven Corsello (participant 1998), and Ms. Leslie Lai (participant 1998). Mr. Lee writes, "One person (Mr. Shannon) stands out most in providing me encouragement and confidence to further my studies in engineering." He adds, "He loves interacting with students, he loves teaching, and he loves chemistry." Mr. Corsello writes, "Mr. Shannon's unique teaching style enables his students to better understand chemistry." Ms. Lai writes, "He devoted his time to each student and made it easier for everyone to learn the material," and "He is one of the most encouraging people I have ever met." Ms. Kathleen Walling, principal of Pittsford Mendon High School, adds, "Jim is one of the most talented and dedicated teachers at this high school and has long been a favorite of students and parents," and "Jim has gone far above and beyond the requirements of his job description time and time again."

Table 84.V: High School Students and Projects—Summer 2000.

Name	High School	Supervisor	Brief Project Title
Andrew Campanella	Webster	P. Jaanimagi	Large-Area, Low-Voltage X-Ray Source
Jill Daum	Rushville	D. Smith/J. Taniguchi	Experimental Simulation of Damage in Spatial-Filter Lenses
Abraham Fetterman	Pittsford Mendon	M. Skeldon	Modeling Pulse Shape Distortions in the OMEGA Laser
Ming-fai Fong	Pittsford Sutherland	S. Regan	Experimental Investigation of Smoothing by Spectral Dispersion (SSD) with Apertured Near Fields
Robert Forties	Irondequoit	F. Marshall	X-Ray Sensitivity Measurements of Charge Injection Devices
Binghai Ling	Brighton	R. Epstein	Simulation of Plasma Spectra and Images of Foil Targets Using the Prism SPECT3D Radiation-Transport Post-Processor
Anne Marino	Hilton	S. Jacobs	Developing a Durable Phosphate Glass with a Low Glass Transition Temperature
Elizabeth McDonald	Harley	J. Zuegel	Adapting ASBO/VISAR for Foam Targets
Ronen Mukamel	Brighton	S. Craxton	Modeling the Spectra of Frequency-Converted Broadband Laser Beams on OMEGA
Gloria Olivier	Honeoye Falls-Lima	K. Marshall	Improving the Visible Selective Reflection in Lyotropic Cellulose Urethane Liquid Crystals
Colin Parker	Brighton	J. Marozas	Dynamic Focal Spot Size Using a Static Phase Plate
Priya Rajasethupathy	Brockport	J. Delettrez	Improving Equation-of-State Tables
John Savidis	Gates-Chili	R. Sobolewski	Characterization of Ultrafast Superconducting Optoelectronic Devices
Stephanie Wolfe	Spencerport	D. Smith/J. Oliver	Coatings for Ultraviolet Lithography

FY00 Laser Facility Report

The three primary priorities on OMEGA in FY00 in addition to executing target shots (see Table 84.VI) were (1) activate and test the full suite of Cryogenic Target Handling System (CTHS) equipment, (2) improve single-beam uniformity by activating the first terahertz (THz)-bandwidth-capable SSD system, and (3) improve overall on-target uniformity by balancing the beam-to-beam power fluctuations.

The following system improvements and modifications were realized during FY00:

- Demonstration of all Cryogenic Target Handling System (CTHS) subsystems and integrated testing including shooting cryogenic DD test shots; demonstrated capability of up to three cryogenic target shots per week.

- Installation of 1-THz smoothing by spectral dispersion (SSD), characterization of improved beam smoothing, and utilization of THz SSD on many experimental campaigns.

- Installation of 60 modified frequency-conversion-crystal (FCC) assemblies for broad-bandwidth (THz) capability as well as refurbished and environmentally protected optical surfaces (three KDP crystals per beamline). This project virtually eliminated a scatter loss of up to 20% at the end of the beamlines.

- Installation of 60 distributed polarization rotators (DPR's) on the full-aperture UV system for time instantaneous beam smoothing on target.

- Consistent 3% rms energy balance achieved on-target by balancing gain stages to compensate for small-signal-gain variations.

- Installation of a P510 streak camera, which increased system coverage from 20 beams to 50 beams. In addition, the new cameras have higher dynamic range and better frequency response than the original two cameras.

- Improved beamline laser transport by fixing spatial-filter-lens coating degradation. Sequentially removed, repaired, and replaced 231 lenses in the laser chain. By replacing all sol-gel antireflective coatings with hard oxide coatings, the long-term transmission of the lenses will remain high.

- The OMEGA wavefront sensor was relocated to a new platform on top of the south-end mirror structure of the Target Bay and re-engineered for multiplexed diagnostic functions as well as the capability to capture any of five OMEGA beamlines.

- In March 2000 the pulse shaping system was replaced by integrated, electronically synchronized hardware. This 1aperture-coupled-stripline (ACSL) system has improved performance and increased reliability over the previous pulse shaping system.

Table 84.VI: The OMEGA shot summary for FY00.

LLE-ISE	320
LLE-RTI	195
LLE-LPI	43
LLE-other	24
LLNL	284
LANL	131
NLUF	124
CEA	21
SNL	11
Total	1153

National Laser Users' Facility News

During FY00 external use of OMEGA increased by 12% and accounted for 50% of the total target shots carried out on the facility. The external users included six teams carrying out work under the National Laser Users' Facility (NLUF) program as well numerous other scientific teams from Lawrence Livermore National Laboratory (LLNL), Los Alamos National Laboratory (LANL), Sandia National Laboratory (SNL), the Nuclear Weapons Effects Testing (NWET) program, and Commissariat à l'Énergie Atomique (CEA) of France.

FY00 NLUF Experiments

The seven NLUF experimental campaigns totaling 124 OMEGA target shots carried out in FY00 included the following:

High-Spatial-Resolution Imaging of Inertial Fusion Target Plasmas Using Bubble Neutron Detectors.
Principal Investigator: Raymond K. Fisher (General Atomics) and collaborators from the University of Rochester (LLE), CEA, and LLNL.

In this experiment, bubble neutron detectors were successfully used for the first time to record neutron images of ICF implosions in OMEGA experiments. The gel bubble detectors were attached to the back of a 10-in. manipulator (TIM) containing a neutron penumbral aperture designed and constructed by a team from the CEA. Figure 84.46(a) shows a photograph of the light transmitted through one of the detectors. Detailed analysis of the bubble density distribution yields the coded image shown in Fig. 84.46(b). The target plane neutron source distribution, obtained from a mathematical inversion of this image, is shown in Fig. 84.46(c). As expected, the counting statistics (resulting from the low neutron detection efficiency of the gel bubble detectors) limit the spatial resolution of this image to ~250 μm. There was no evidence of any background due to x rays or gamma rays. Development of a liquid bubble chamber detector should result in higher neutron detection efficiency and resolution of ~10 to 50 μm.

(a)
Photo of detector

(b)
Coded image (binned)

(c)
Unfolded image (source)

Max

0.5

250 μm

0.0

8.3 cm

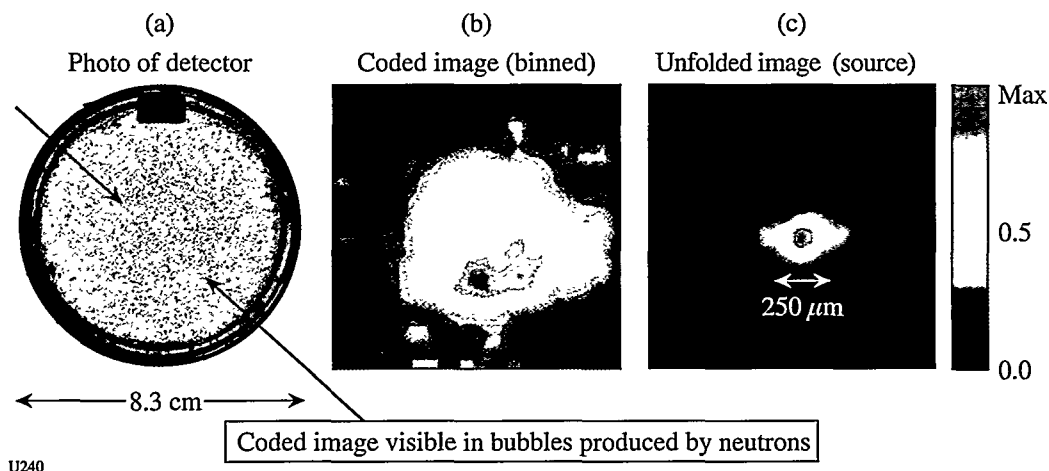Coded image visible in bubbles produced by neutrons

U240

Figure 84.46
(a) Photograph of gel bubble detector after exposure to an OMEGA shot producing 6 × 10^{13} DT neutrons. The coded image is visible as a circular pattern of bubbles in the center of the detector. (b) Raw digitized coded image. (c) Unfolded neutron image.

Continuing Studies of Dynamic Properties of Shock-Compressed Solids by In-situ *Transient X-Ray Diffraction.*
Principal Investigators: Marc Andre Meyers (University of California at San Diego) and Dan Kalantar (LLNL) and collaborators from LLNL, LLE, Oxford University, California Institute of Technology, and LANL.

This work continued a program of studies to investigate the response of crystals to shock compression in regions of strain rates previously unexplored. A series of experiments were conducted to demonstrate the time-dependent compression of a single-crystal Cu sample compressed by direct laser irradiation. Time-resolved streak records of the diffraction from two orthogonal lattice planes in Cu were obtained. Compressions of up to about 3% were observed in both directions at a shock pressure of approximately 200 kbar, confirming that the lattice responds plastically on a nanosecond time scale. A number of different thin-crystal target configurations were tested to identify and resolve issues of x-ray preheat due to the laser drive, and a mixed backlighter was tested to measure the compression of different parallel lattice planes. In addition, simultaneous

shock compression and post-shock recovery experiments were conducted with single-crystal Cu to relate the residual damage to the *in-situ* diffraction measurements (Fig. 84.47). A series of nine 1-mm-thick Cu samples were shocked and recovered for post-shot TEM analysis.

Supernova Hydrodynamics on the OMEGA Laser.
Principal Investigators: Paul Drake (University of Michigan) and Bruce Remington and Harry Robey (LLNL) and collaborators from LLNL, LLE, CEA, Osaka University, University of Arizona, University of Chicago, Eastern Michigan University, State University of New York–Stony Brook, and West Point Military Academy.

Supernovae are not well understood. Recent observations have clarified the depth of our ignorance by producing observed phenomena that current theory and computer simulations cannot reproduce. Such theories and simulations involve, however, a number of physical mechanisms that have never been studied in isolation. In this project, which this year involved 22 co-investigators from 11 institutions, well-scaled
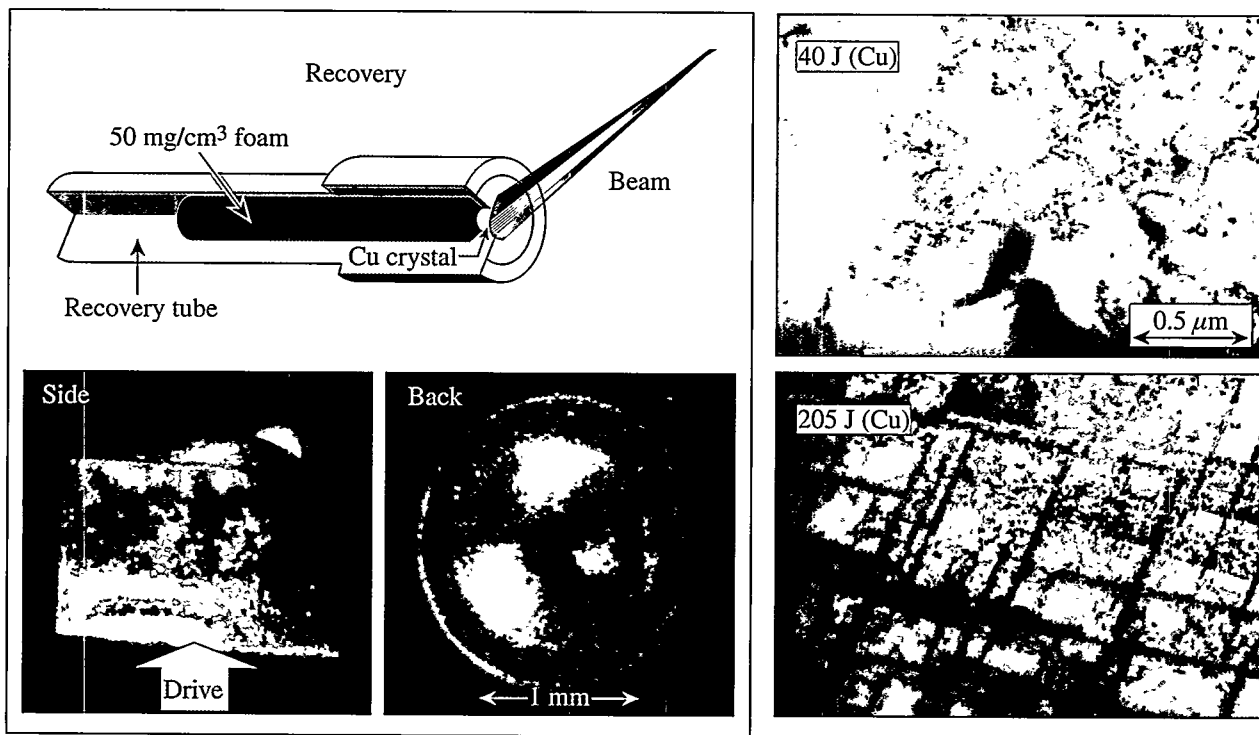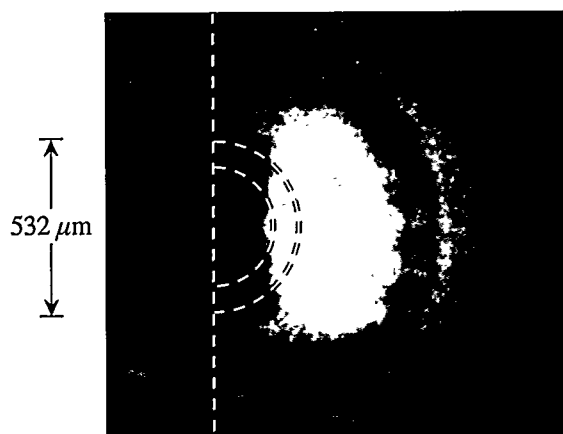

U241

Figure 84.47
Illustration of crystal recovery experiments. Top left: the experimental configuration. Bottom left: photographs of a recovered Cu sample. Right: post-shot TEM photographs of shocked Cu samples shocked with a 40-J laser pulse (top) and a 205-J laser pulse (bottom). These samples were compressed at extreme strain rates, but they show similar residual dislocation and other microstructure as crystals shocked in lower-strain-rate gas-gun experiments.

experiments conducted on OMEGA investigated such mechanisms. Such experiments also provide clear tests of the codes used to simulate astrophysical phenomena. This past year's experiments were also used to observe interface coupling. In this case a shock wave was perturbed by structure at a Cu/plastic interface, and it in turn caused structure to evolve at a plastic/foam interface. Experiments were also conducted to study hydrodynamic instability growth at a spherically diverging interface (see Fig. 84.48). In addition, experiments were initiated to compare instability growth in 3-D versus 2-D, to examine the growth of multimode perturbations, and to produce and diagnose a radiative precursor shock.

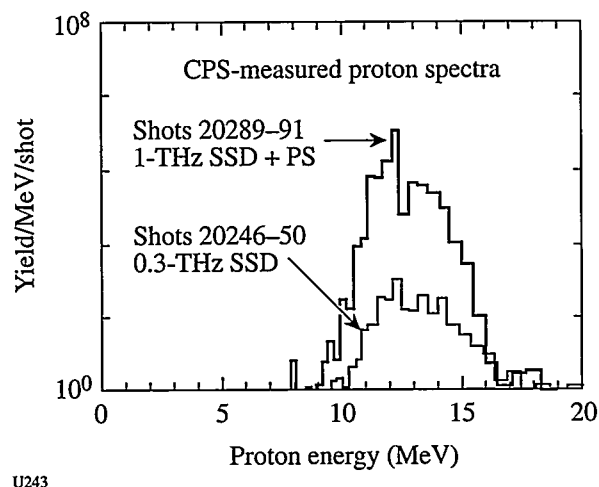of the best means for studying high-density cryogenic capsule implosions.

Figure 84.49

Comparison of multishot-averaged secondary proton spectra obtained with the CPS 2. Shots 20289 to 20291 were carried out with improved uniformity (1-THz, 2-D SSD and polarization smoothing), while shots 20246 to 20250 were carried out with 0.3-THz, 2-D SSD and no polarization smoothing. Note the higher secondary proton yields and increased energy downshift (indicating higher shell areal density) for the improved uniformity implosions.

Figure 84.48

X-ray radiograph showing modulations on a spherical capsule that has expanded into resorcinol foam of density ~100 mg/cm^3. The initial outside diameter of the Br-doped CH capsule was 532 μm and the wall thickness was 97 μm. Initial perturbation wavelength and amplitude were 70 μm and 10 μm, respectively. Hydrodynamic instabilities, like those present in supernovae, caused the observed modulations to develop from the small initial perturbations.

Charged-Particle Spectroscopy on OMEGA:
Recent Results, Next Steps.
Principal Investigator: Richard Petrasso (Massachusetts Institute of Technology) and collaborators from LLNL, LLE, and SUNY Geneseo.

The focus of this year's work has been the acquisition and interpretation of high-resolution secondary proton spectra [Fig. 84.49; see also LLE Review **83**, 130 (2000)]. These results are important not only for the information obtained for the current gas-filled capsule implosion experiments but also in demonstrating the potential to characterize cryogenic-target implosions. Secondary-proton spectroscopy may provide one

Development of X-Ray Tracer Diagnostics for Radiatively Driven NIF Ignition Capsule Ablators.
Principal Investigator: David Cohen (Prism Computational Sciences) and collaborators from the University of Wisconsin, LLE, LANL, SNL, and LLNL.

This program continued a series of x-ray spectroscopic measurements to explore the physics of radiation-driven, NIF-type ablators. The FY00 campaign included two days of shots in which time-dependent backlit absorption spectra were measured from thin tracer layers buried inside capsule ablator samples that were mounted on halfraums (see Fig. 84.50). A significant signal was observed from NaCl tracers (Cl K$_\alpha$) in both germanium-doped and undoped plastic ablator samples. The onset of the signal was seen to be delayed in the doped sample as compared to the undoped sample. Furthermore, especially in the doped sample, the progressive heating of the tracer can be seen as the dominant ionization state moves from Be-like to He-like over an interval of ~100 ps (Fig. 84.51). These data demonstrate the effects of ablator dopants on the radiation wave characteristics. Among other innovations in this year's campaign, we were able to construct targets and mount diagnostics in such a way as to do simultaneous spectroscopy of two samples on a single halfraum using two

different time-resolved spectrometers. These experiments are relevant for ablator characterization and target design efforts for NIF ICF targets.
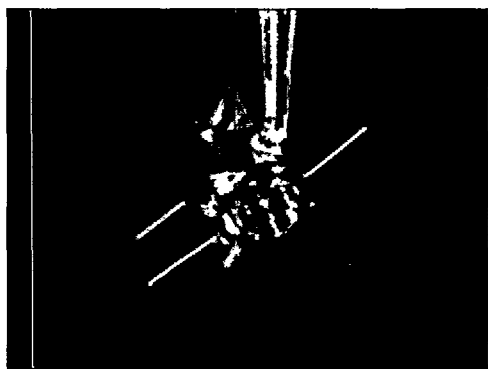

U244

Figure 84.50
A Powell-scope image of a halfraum target, seen from the laser entrance hole (LEH) side. The rectangular object in front of the LEH is a bismuth backlighter foil. The positioning stalk can be seen at the top of the barrel of the halfraum, and various positioning fibers and shields are also visible. The ablator sample (in the form of a witness plate) is on the back end of the cylinder.

Investigation of Solid-State Detection of Charged-Particle Spectrometry.
Principal Investigator: Kurtis Fletcher (State University of New York at Geneseo) and collaborators from MIT, LLE, and LLNL.

In this collaboration, electronic detection of charged particles was demonstrated using the charged-particle spectrometer (CPS1) on OMEGA. A 250-μm-thick pin diode was mounted in the spectrometer focal plane at the position corresponding to ~15-MeV protons. In a series of shots with D^3He-filled CH shells, high-energy protons passed through a collimator, an Al filter, and a CR-39 track detector before stopping in the diode. Each proton deposited about 3.5 MeV of energy in the diode. The resulting voltage signal of the diode was recorded on an oscilloscope [see Fig. 84.52(a)]. The CR-39 detector for each shot was later etched and the number of protons counted to provide a benchmark for the electronic detection system. As expected, the area of the proton peaks was proportional to the number of protons [see Fig. 84.52(b)]. This project demonstrated proof-of-principle that electronic detection of charged particles generated in the ICF environment is possible under appropriate conditions.
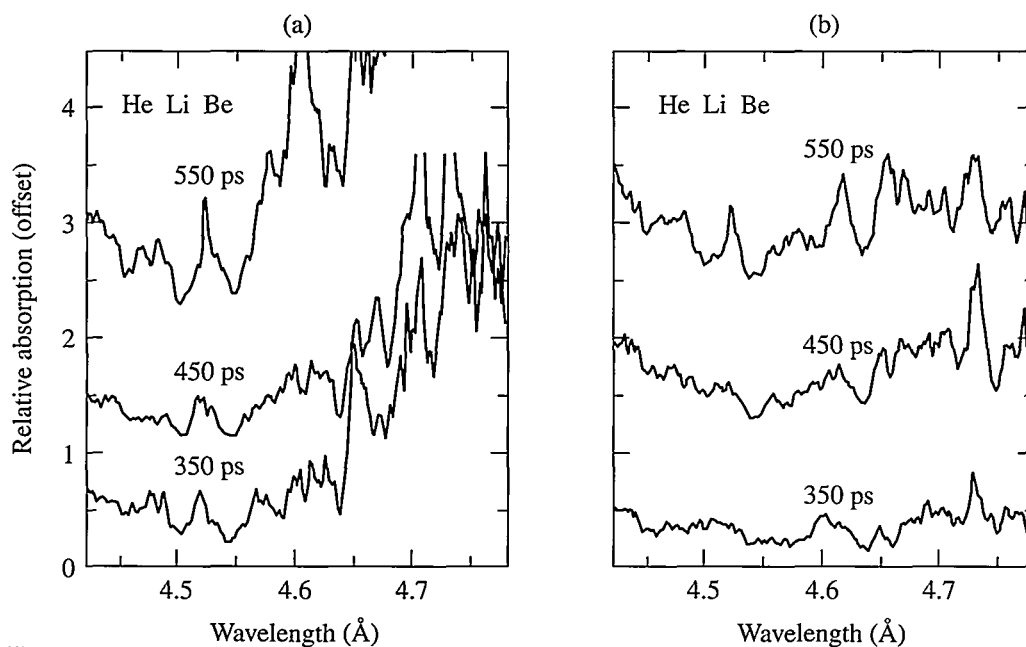
U245

Figure 84.51
Time-resolved absorption spectra of chlorine features from (a) an undoped sample and (b) a doped sample. The three prominent tracer absorption features are marked on each figure. The three lineouts shown in each figure are time-averaged over 100 ps.
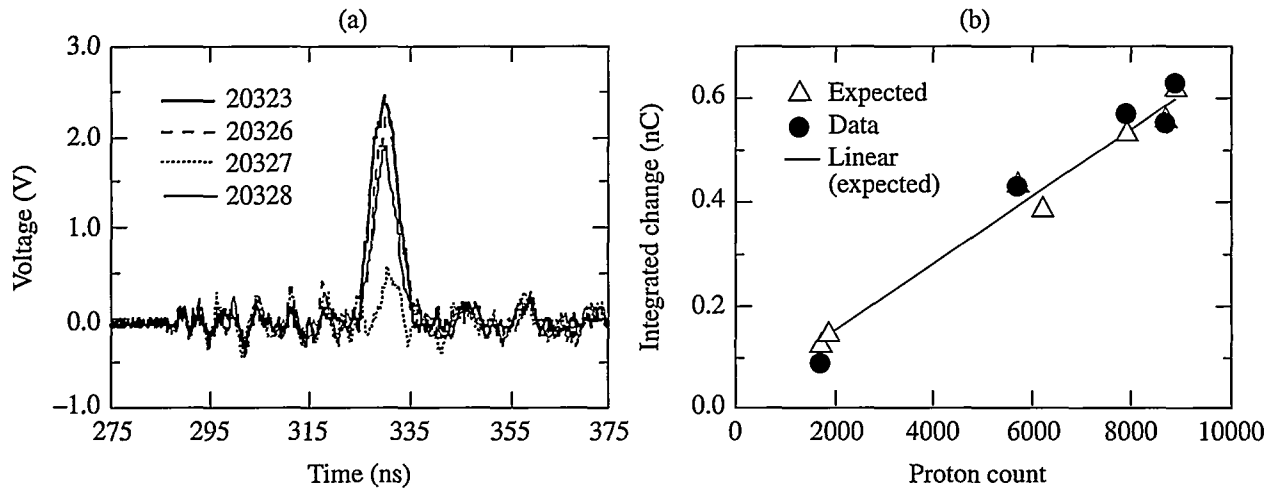
Figure 84.52

(a) Solid-state (PIN)-detector primary proton signals obtained on four shots (20323, 20326, 20327, and 20328) on D³He-filled CH shells.
(b) Integrated charge on solid-state detector versus the proton count as measured with a CR-39 track placed ahead of detector.

Optical Mixing of Controlled Stimulated Scattering Instabilities (OMC SSI) on OMEGA II.
Principal Investigator: Bedros Afeyan (Polymath Research Inc.) and collaborators from LLNL, LANL, and LLE.

In this collaboration, experiments continued to investigate optical-mixing-controlled stimulated scattering instabilities in NIF-like, long-scale-length plasmas. This year, the OMC SSI experiments concentrated on extending the previous results showing stimulated Raman scattering (SRS) back-scattering reduction of an interaction or pump beam in the presence of an overlapping (probe) laser beam at the Mach = −1 surface. The interaction of the two beams is expected to produce a spatially localized, large-amplitude ion-acoustic wave (IAW). This IAW in turn dephases the SRS instability by producing IAW turbulence. The dependence of the nonlinear interaction processes on pump and probe beam intensity, probe beam spot size, and crossing region location were investigated in the FY00 experiments. Some of the results of these experiments are shown in Fig. 84.53.

FY01 NLUF Proposals

A record 17 proposals with funding requests totaling $3,685,742 (total for FY01 and FY02) and with shot requests of 360 and 370 shots, respectively, in FY01 and FY02 were submitted to NLUF this year. For the first time, the successful proposals will be approved for a two-year period of performance (FY01 and FY02).
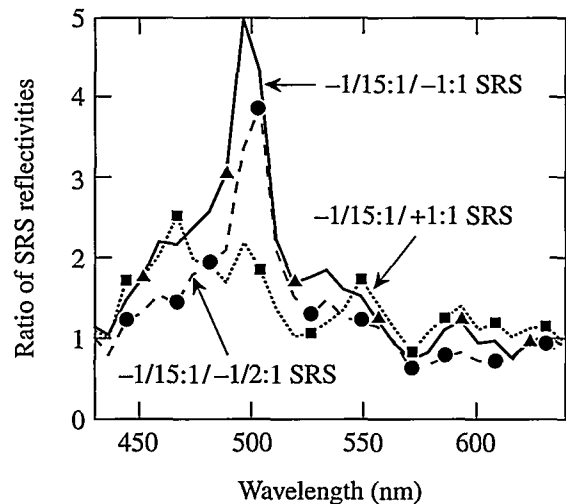
Figure 84.53

Ratio of stimulated Raman backscattering (SRBS) reflectivities plotted versus wavelength integrated over time. The plot shows weak-probe SRBS reflectivities where the intensity ratio between probe and pump beams is 15:1, divided by strong-probe SRBS reflectivities where the intensity ratio between probe and pump is 1:1 (solid curve) and 1/2:1 (dashed curve) and the probe beam is focused where the flow velocity is Mach = −1. The dotted curve is the control; the intensity ratio of pump to probe is 1:1 but the beams are focused where the flow is Mach = +1, where no resonant ion wave can be driven by the interaction of pump and probe. The dotted curve is not flat at M = +1 because even at that focus some of the light does get to Mach = −1, giving a slight reduction of the SRBS.

A DOE technical evaluation panel including Dr. David Bradley (LLNL), Dr. David Montgomery (LANL), Dr. Richard Olson (SNL), and Dr. Ned Sautoff (Princeton Plasma Physics Laboratory) reviewed the proposals on 19 May 2000. The NLUF Manager (non-voting) chaired the panel. The committee recommended approval of eight of the proposals (see Table 84.VII) with reduced funding and shot allocation to fit within the budget of $700,000 per year and NLUF shot allocation of 120 shots per year. A ninth proposal was conditionally approved pending additional funds from DOE.

FY00 National Laboratory, NWET, and CEA Programs

When Nova operations ended in FY99, national laboratory and other use of OMEGA continued to increase. Programs of the three national laboratories (LLNL, LANL, and SNL), NWET, and CEA accounted for over 38% of OMEGA use during this fiscal year. The following is a brief summary of some of the work carried out by the national laboratories, NWET, and CEA:

1. LLNL and NWET Campaigns

In FY00 LLNL had 320 shot opportunities at the OMEGA facility, divided as follows: 100 shots for target ignition physics (TIP), 200 shots for high-energy-density science (HEDS), and 20 shots for nuclear weapons effects testing (NWET). A total of 284 target shots were taken. These shots involved 15 Principal Investigators (including shots with collaborators from SNL and LANL) and spanned the 21 different mini-campaigns listed in Table 84.VIII.

Highlights of LLNL experiments include the following:

Conversion Efficiency: An initial OMEGA campaign was carried out to investigate the x-ray drive energetics in roughened hohlraums. Roughened hohlraums are required for infrared augmented β-layering on NIF, and the initial OMEGA results indicate that the rough hohlraums appear brighter than the smooth ones, contrary to expectations.

Cocktail Hohlraums: Experiments were initiated on OMEGA to investigate the soft x-ray emission of "cocktail" materials—i.e., mixtures of elements rather than the conventional Au-lined hohlraum. The initial results are in agreement with *LASNEX* simulations, and experiments will continue to confirm the expectations of higher drive with cocktail materials.

NIF Foot Symmetry: NIF-scale, 90-eV hohlraum symmetry experiments were carried out on OMEGA with a novel point-projection backlighting technique to assess the symmetry of drive in the foot of the NIF pulse. The results of these experiments indicate that the technique is capable of 1% accuracy in detecting asymmetry modes in NIF-scale targets.

Table 84.VII: Approved NLUF Proposals for FY01/02

Principal Investigator	Affiliation	Title of Proposal
C. F. Hooper, Jr.	University of Florida	Atomic Physics of Hot, Ultradense Plasmas
R. Mancini	University of Nevada, Reno	Determination of Temperature and Density Gradients in Imploded Cores of OMEGA Targets
R. Petrasso	Massachusetts Institute of Technology	Studies of Fundamental Properties of High-Energy-Density Plasmas
H. Baldis	University of California - Davis	Studies of Dynamic Properties of Shock-Compressed FCC Crystals
R. K. Fisher	General Atomics	High-Spatial-Resolution Neutron Imaging of Inertial Fusion Target Plasmas Using Bubble Neutron Detectors
R. B. Stephens	General Atomics	Asymmetric Fast Ignition Target Compression
P. Drake	University of Michigan	Supernova Hydrodynamics on the OMEGA Laser
B. B. Afeyan	Polymath Research, Inc.	Optical-Mixing-Controlled Stimulated Scattering Instability Experiments on OMEGA III and IV: Suppressing Backscattering Instabilities by the Externally Controlled Generation of Ion Acoustic Wave or Electron Plasma Wave Turbulence

High-Convergence Implosions: The multicone capability of OMEGA was used to conduct hohlraum-driven implosion experiments with an inferred convergence ratio up to 20. The resulting neutron yield on these implosions was significantly improved compared to the previous Nova results with a single cone of beams (see Fig. 84.54).

Shock Timing: Using a shock optical pyrometer (SOP), the UV emission of shock breakout was measured and used to infer shock velocity in radiation-driven ablators. Shock propagation data were obtained for Al, polyimide, and Be+0.9% Cu samples. These experiments were carried out in a collaboration involving SNL, LANL, LLNL, and UR/LLE.

Ablator Burnthrough: SNL led a team of LLNL, LANL, and LLE scientists in conducting an experiment to investigate burnthrough in a radiation-driven capsule. The experiment

was designed to provide verification of ICF ablator burnthrough timing. Indirect-drive burnthrough data were obtained for polyimide and beryllium samples using the half-hohlraum (halfraum) geometry shown in Fig. 84.55(a). Spatially resolved streak camera imaging was used in conjunction with timing fiducials provided by two of OMEGA's beams to provide this data [see Fig. 84.55(b)].

Convergent Ablator Burnthrough: X-ray-backlit implosions were used to determine the ablation rate and payload trajectory in spherical geometry in the hohlraum drive. Some of the results from these experiments are shown in Fig. 84.56.

Planar RT: Polyimide ablator Rayleigh–Taylor growth measurements were conducted on radiation-driven planar targets on OMEGA. The initial OMEGA experiments show acceptable agreement with code predictions for all wavelengths (see Fig. 84.57).

Table 84.VIII: LLNL Campaigns on OMEGA in FY00.

| Campaign	Sub-Element	Experiment	Target Shot Allocation
Target Ignition Physics	WBS 1 – Energetics	Conversion efficiency	15
		Laser–plasma interaction	10
		Cocktail hohlraums	5
	WBS 2 – Symmetry	NIF foot symmetry	20
		High-convergence implosions	5
	WBS 3 – Ablator Physics	Shock timing	15
		Ablator burnthrough	10
		Convergent ablator burnthrough	10
		Planar RT	10
High-Energy-Density Sciences	Solid-State Hydro		15
	Implosion Mix	Pushered shells	15
	Hydro I	Richtmyer–Meshkov	40
	Hydro II	Features	20
	Hydro III	Jets	20
	Radiation Transport	Low T_r drive	5
		Radiation transport in foams	30
	Equation of State (EOS)	Low- and high-Z EOS	35
	Capability Development	Backlighter development	15
		Fluorescence mix	5
Nuclear Weapons Effects Testing (NWET)	Source Development	Gas-filled-Be-can sources	10
		Hot-electron sources	10
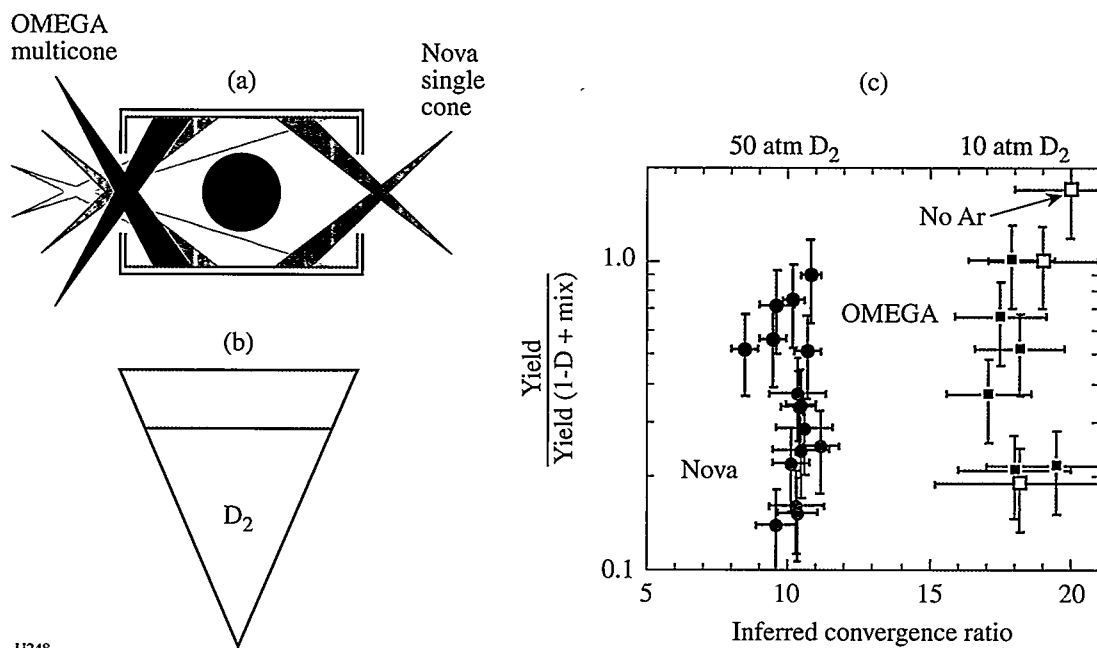
Figure 84.54

(a) Schematic illustrating the beam configuration for OMEGA compared to Nova. (b) Typical capsules used in these experiments were D_2-filled, Ge-doped CH shells. (c) Plot of the ratio of the measured neutron yield over the calculated 1-D yield including mix as a function of the inferred convergence ratio. The low-convergence-ratio targets contained 50 atm of deuterium (data points are circles), while the higher-convergence-ratio targets contained 10 atm (square data points). The open data points contained no Ar doping in the fuel. The Nova points are gray and the OMEGA data are black.
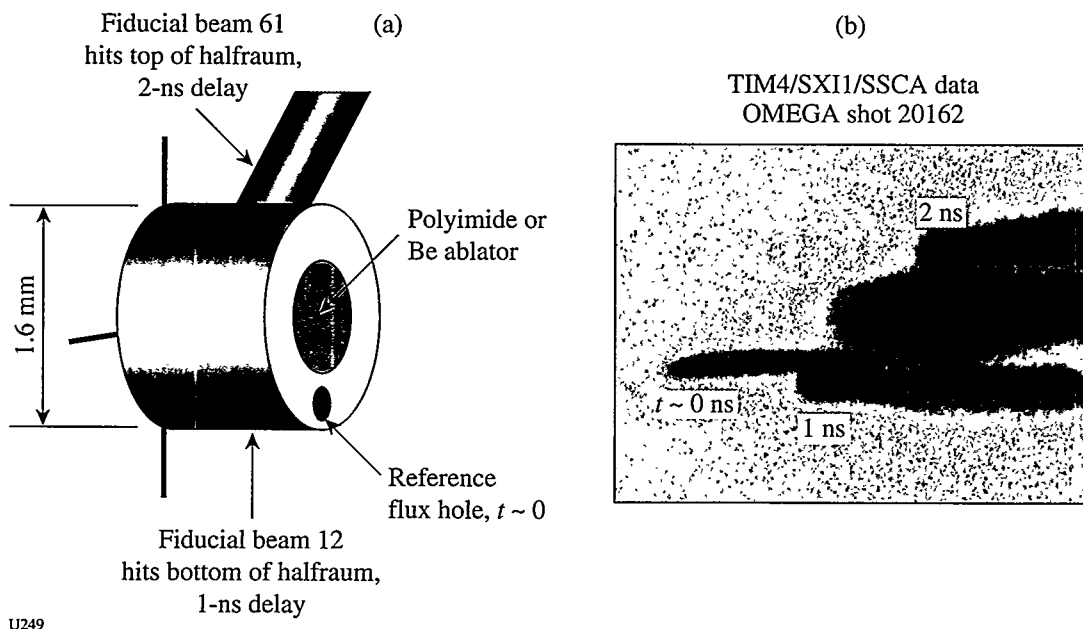

Figure 84.55

(a) Schematic of burnthrough experiment. Fifteen drive beams are brought into the halfraum in two cones, while two beams irradiate the top and bottom of the exterior of the halfraum to provide timing fiducials. A hole in the halfraum provides a time history of the x-ray flux in the halfraum. (b) Streak camera record of x-ray emission showing the reference flux hole emission ($t \sim 0$) and delays ($t \sim 1$ and 2 ns) along with the central delayed feature signaling burnthrough to the ablator being used in this experiment.
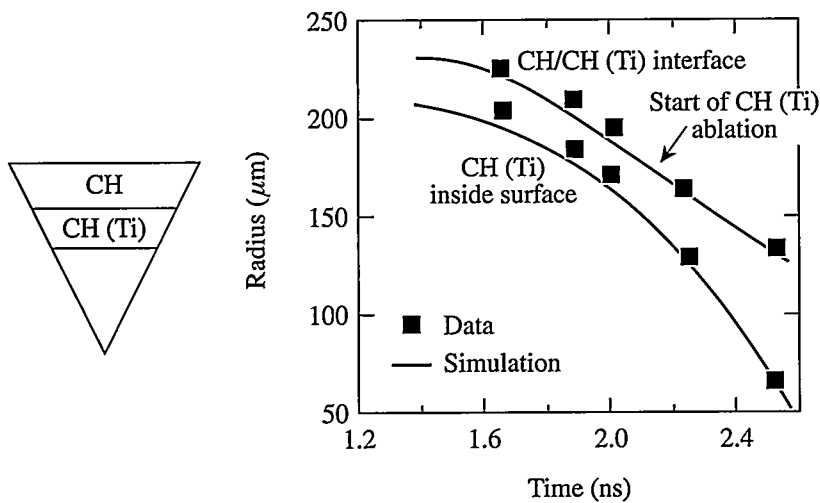
Figure 84.56
Measurement of ablation rate and payload trajectory in a hohlraum-driven spherical implosion experiment. The ablator for this experiment was CH, and an inner layer of Ti-doped CH served as the signature of ablator burn-through. Time-gated radiography with 5.2-keV x rays was used to make this measurement.
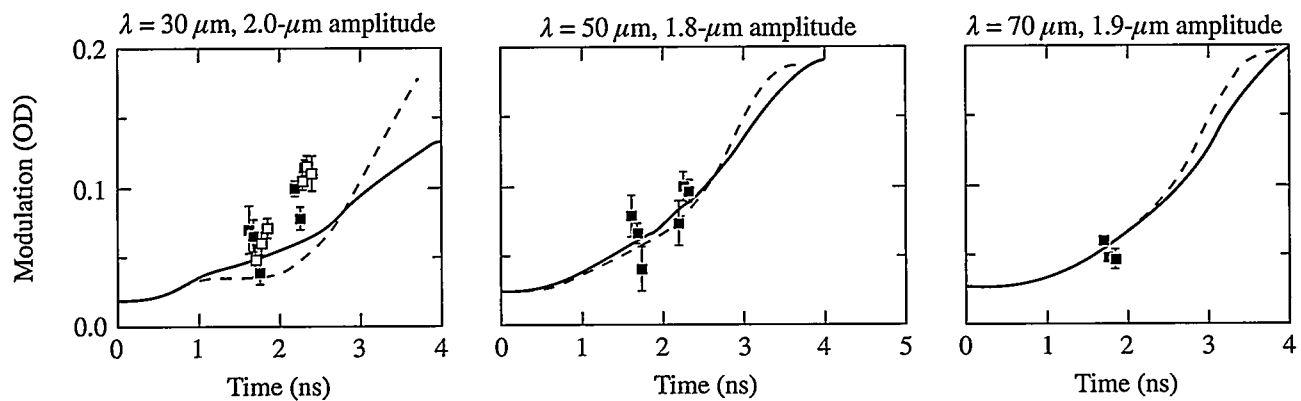

Figure 84.57
Results of Rayleigh–Taylor growth measurements on radiation-driven polyimide foils. These three plots show the measured modulation (OD) as a function of time for three radiation-driven planar targets with different initial wavelengths and amplitudes. The dashed lines represent simulations using a Planckian spectrum, while the solid lines represent the simulations using Dante-derived drive and calculated spectrum.

Pushered Shells: Experiments were conducted on a hohlraum-driven, single-shell target design consisting of a DT-filled glass shell overcoated with Ge-doped CH. The neutron burn history, neutron yield (20% of clean yield), radiation drive, and absorption imaging of the CH/SiO_2 trajectory were compared to hydrodynamics simulations.

Hydrodynamics: Several important hydrodynamics campaigns were carried out on OMEGA in FY00. A new shock-driven hydrodynamics geometry was successfully tested, and VISAR measurements of shock velocity were carried out. Simultaneous side-on and face-on data were obtained and 3-D features clearly observed on the interaction of a shock and a sphere. A collaborative experiment between the AWE (United Kingdom), LANL, and LLNL investigated the interaction of a

supersonic jet with a counter-propagating shock. These experiments were simulated using the *RAGE* code at LANL, the *CALE* code at LLNL, and the *NYM-PETRA* code at AWE.

Long, Low T_r Drive: X-ray diffraction was used to measure melt and 1-D to 3-D lattice transitions on OMEGA. Simultaneous measurements of Bragg and Laue patterns on Cu showed 3-D compression of the crystal lattice.

Radiation Transport in Foams: The importance of wall structure and wall losses was demonstrated in experiments on foam-filled hohlraums.

Low- and High-Z EOS: Equation of state of relevant materials was measured at high pressures (1 to 50 Mbar) on OMEGA.

These experiments were conducted in both direct- and indirect-drive mode and showed that preheat is an issue for both approaches for these measurements.

Backlighter Development: A new backlighting capability was validated that will be used on NIF hydro experiments. This technique is pinhole-assisted point projection backlighting. Ultrahigh (100×)-magnification x-ray imaging was carried out to measure the core of OMEGA hohlraum-driven target implosions. This approach has the capability of providing 3-μm resolution at an x-ray energy of 6 keV.

Gas-Filled-Be-Can X-Ray Sources: Experiments were carried out on OMEGA to investigate the x-ray production of internally irradiated gas- and foam-filled Be cans. High conversion efficiency (~10%) to Ar K-shell and Xe L-shell radiation was measured for Ar- and Xe-filled Be cans. Foam-filled (6 mg/cm^2 SiO$_2$) cans demonstrated 30× enhancement of 50-keV x rays compared to previous measurements with 1% of critical density (n_c) C$_6$H$_{12}$ gas-filled cans.

2. LANL Campaigns

Los Alamos National Laboratory conducted several experimental campaigns at OMEGA during FY00 as part of Campaign 10 Major Technical Efforts in Indirect-Drive Ignition and Support for Stockpile Stewardship. These campaigns included the following:

Double Shells: These experiments showed that the performance of the reduced M-band absorption (imaging) double-shell target exceeds that of all others at convergence ratio (CR) ~38 (see Fig. 84.58).
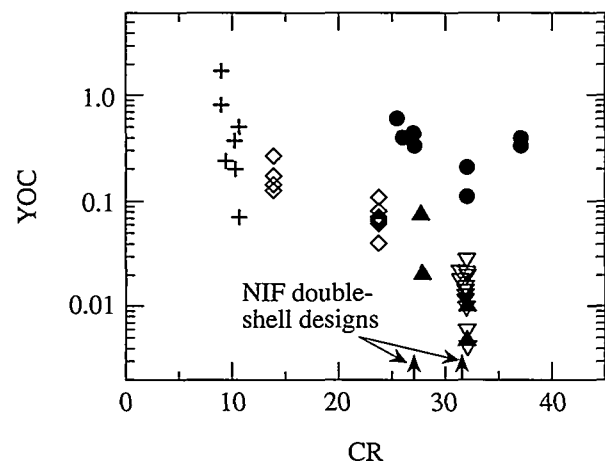
Classified Experiments: Classified experiments with important results were successfully hosted by LLE.

Direct-Drive Cylinder Experiments (DDCYL): DDCYLMIX experiments achieved good "low-mix/high-mix" comparison with well-characterized conditions for compressible plasmas in convergent geometry (see Fig. 84.59). Static targets better characterized the details of image analysis and careful comparison to theoretically simulated radiographs.

Backlighter Studies: Energy and intensity-dependent scaling for K-shell backlighters were determined for NIF-relevant backlighters. A series of experiments (Fig. 84.60) were carried out using Fe, Zn, and Ge backlighter targets driven at relatively high laser intensity (1×10^{16} W/cm^2).

High-Convergence Implosions: X-ray imaging of single-shell implosions showed transition from a limb-brightened image to a centrally peaked image at CR~23, indicative of mix.

Spike Dissipation: Laser-based experiments have shown that Rayleigh–Taylor growth in thin, perturbed copper foils leads to a phase dominated by narrow spikes between thin bubbles. These experiments are well modeled and measured until this "spike" phase, but not into the spike phase. Experiments were designed and carried out on OMEGA to explore the late-time spike phase. The OMEGA experiment used side-on radiography with a 6.7-keV Fe backlighter source. A gated x-ray imager time-resolved the x-ray transmission image from which the temporal development could be obtained (Fig. 84.61).

Figure 84.58
Ratio of measured neutron yield over the calculated clean yield (YOC) plotted as a function of calculated convergence ratio for indirect-drive Nova and OMEGA experiments. The diamonds indicate Nova cylindrical-hohlraum single-shell shots (1.4-ns square pulse shots). The crosses are data from tetrahedral-hohlraum single-shell-capsule experiments on OMEGA (1-ns square pulse). The inverted triangles represent standard double-shell data taken on OMEGA. The upright triangles represent suppressed M-band hohlraum double-shell-target data, and the solid circles represent reduced M-band absorption double-shell-capsule data taken on OMEGA. The arrows indicate NIF double-shell ignition designs with foams of 0.15 g/cc and 0.1 g/cc at convergence ratios 24 and 33, respectively.
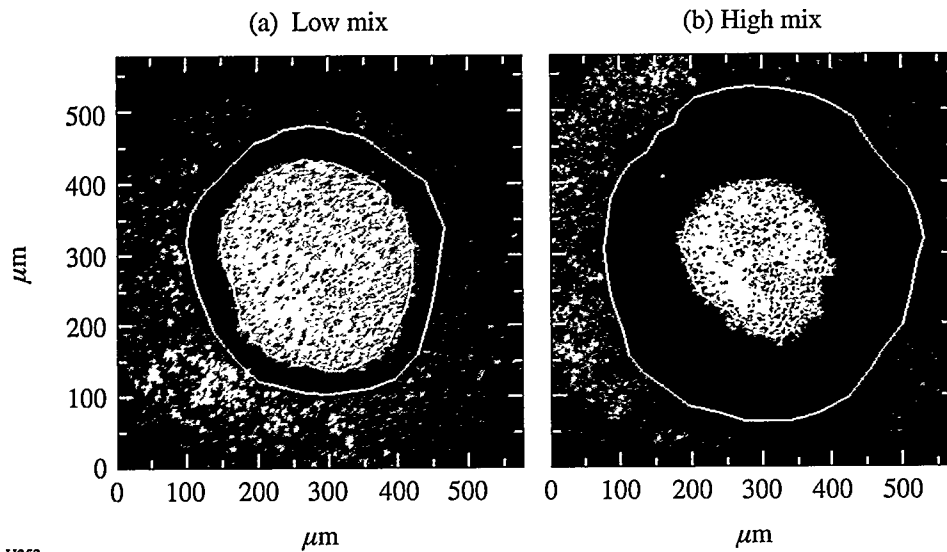
(a) Low mix

(b) High mix

Figure 84.59

X-ray radiographs taken along the cylinder axis of directly driven cylindrical target implosions. (a) Shot 18689 (19.1 kJ with Fe backlighter) low-mix target with dichloroprolystyrene marker layer (initial Atwood number = 0.15); (b) (Shot 18687 (19.9 kJ with Ti backlighter) high-mix target with Au marker layer (initial Atwood number = 0.95). Both images are taken 4.75 ns after t_0 in mass-matched implosions.

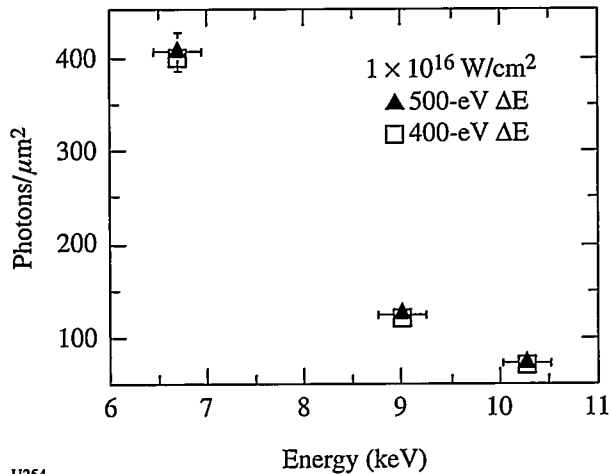1×10^{16} W/cm^2
▲ 500-eV ΔE
□ 400-eV ΔE

Figure 84.60

X-ray fluence in photons per square micron plotted as a function of x-ray energy for Fe (6.7 keV), Zn (9.0 keV), and Ge (10.3 keV) K-shell x-ray emitters. The triangles represent 500-eV energy bandwidth, and squares represent 400-eV bandwidth. The experiments were carried out at an on-target intensity of 10^{16} W/cm^2.

Figure 84.61

Typical radiograph obtained on spike evolution experiment. The Cu target in this case was milled to generate a series of 10- to 20-μm-thin, 200-μm-long, 30-μm-high ridges 150 μm apart, leaving a thin, flat Cu backing. The target was placed on the side of a scale-1.2 OMEGA hohlraum with the ridges pointing into the hohlraum. A laser drive consisting of 1-ns square pulses heated the hohlraum to 190 eV to drive the target. The image shows the growth of the spikes and mushroom-like feet on the tips of the spikes.

High-Yield Neutron Shots for Diagnostic Development: NIF Phase 2 (Advanced) neutron diagnostics for burn history and neutron imaging were fielded, with first observations made of fusion gammas from an ICF target. The signal shown in Fig. 84.62 is from a Gas Cerenkov burn history diagnostic implemented on OMEGA.
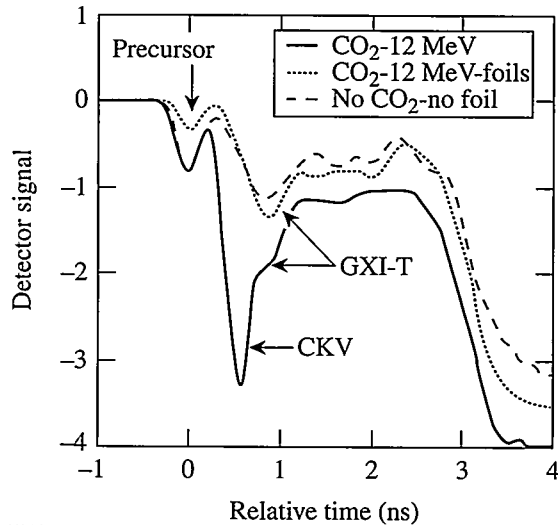

Figure 84.62

Typical Gas Cerenkov counter detector response for a high-neutron-yield, DT-filled-capsule shot (solid line). The Cerenkov signal is the peak at ~0.6 ns (marked CKV). The plot also shows the signals from two other shots where the Cerenkov signal was blocked (dashed line) and where there was no CO_2 gas in the counter (dotted line). The small hump in the back of the Cerenkov signal is apparently due to gamma rays generated by interaction of the neutrons generated in the implosion and the GXI diagnostic.

Los Alamos also supported several other campaigns at OMEGA:

Sandia WBS 3 ablator characterization, NLUF laser–plasma instability work, AWE Jet experiment, and transient x-ray diffraction materials work.

3. CEA Activities

In FY00, CEA (France) activities on OMEGA included the installation and activation of two diagnostics—a penumbral neutron imaging system (NIS) and an absolutely calibrated time-resolved broadband x-ray spectrometer (DMX)—and x-ray conversion efficiency experiments in spherical geometry.

Time-Resolved Broadband X-Ray Spectrometer (DMX): DMX (see Fig. 84.63) is a broad-bandwidth, absolutely calibrated x-ray spectrometer that uses new coaxial x-ray detectors (CXRD) to provide an overall ~100-ps temporal resolution in a compact 20-channel instrument. Spectral resolution is obtained by a combination of mirrors, filters, and detector spectral response. The current configuration covers a range of 50 eV to 20,000 eV. DMX was successfully activated and compared with a similar instrument (LLNL's Dante) on OMEGA shots in both direct and indirect drive. A satisfactory agreement was found between the two diagnostics on spectral shape and x-ray emission time history under various conditions (Fig 84.64), but a discrepancy was observed on absolute levels between the two diagnostics.[1] Further work is in progress to understand the origin of this discrepancy.

X-Ray Conversion Experiments: X-ray conversion experiments on disks are sensitive to 2-D effects. The OMEGA configuration delivers a very uniform laser irradiation pattern, enabling a quasi 1-D experiment in spherical geometry very suitable for the validation of numerical simulations. A set of experiments were carried out to study x-ray conversion on gold-coated, 950-μm-diam CH spheres (2.5 to 3 μm gold thickness) at laser intensities ranging from 3×10^{13} up to 8×10^{14} W/cm^{-2}. X-ray conversion history at different energies, x-ray imaging of plasma, and spectral measurements were used as benchmark simulations.

Neutron Imaging of an Imploding DT Target: Recently, CEA installed a new 14-MeV neutron imaging system (NIS) on OMEGA. This diagnostic measures the size of the neutron-emission area of a direct-drive implosion. A neutron image resolution better than 10 μm is required on future laser facilities such as LMJ and NIF. In June a prototype NIS was tested on OMEGA, using the technique of penumbral imaging, which has an ultimate resolution of 30 μm. The aperture is a massive cylinder (50 mm thick) of tungsten alloy, inside which an aperture with a biconical shape is drilled. The shape of this aperture is defined by entrance, middle, and output diameters of 600 μm, 760 μm, and 1070 μm, respectively. The entrance side of the aperture is set at 55 mm from the target with an aperture manipulator installed into a TIM. The aperture is positioned by a four-stage piezoelectric vacuum compatible actuator, which was tested in a high neutron flux environment. The image is recorded on a detector installed on the Target Bay floor at 8 m from the target chamber center (TCC). The detector is composed of 8000 plastic scintillating fibers. The light is generated mainly by the slowing of a proton produced by elastic scattering of a neutron on hydrogen. The resulting optical image is then amplified by a gated microchannel plate and recorded on the CCD. The CCD is protected from the direct interaction of the neutron by a shield made with polyethylene

228

and lead. The coded image [see Fig. 84.65(a)] is then unfolded by a filtered autocorrelation technique to produce the image shown in Fig. 84.65(b). The source is observed to be 120 μm in diameter on this shot and can be compared with the 3-keV x-ray image obtained on the same shot.

REFERENCES

1. See J. L. Bourgade *et al.*, "DMX: An Absolutely Calibrated Time-Resolved Broadband Soft X-Ray Spectrometer Designed for MJ Class Laser-Produced Plasmas," to be published in the Review of Scientific Instruments.
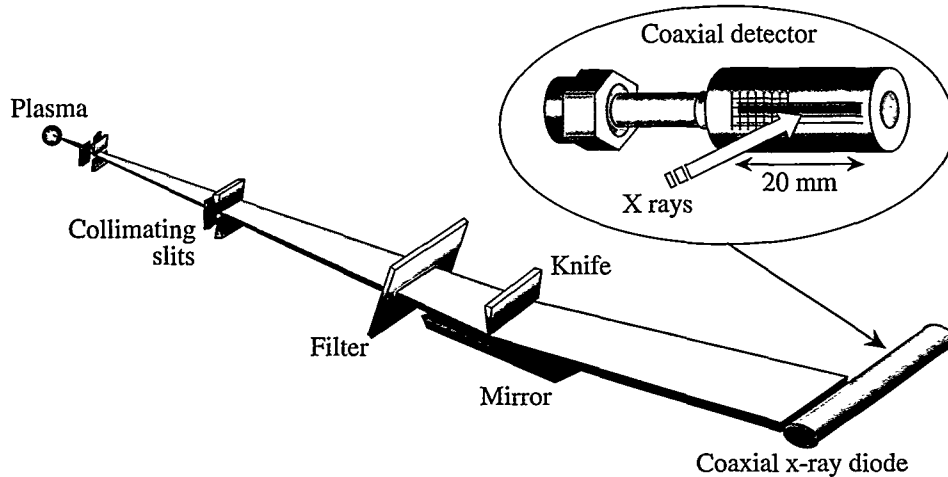
Figure 84.63
Illustration of a DMX diagnostic.

U257
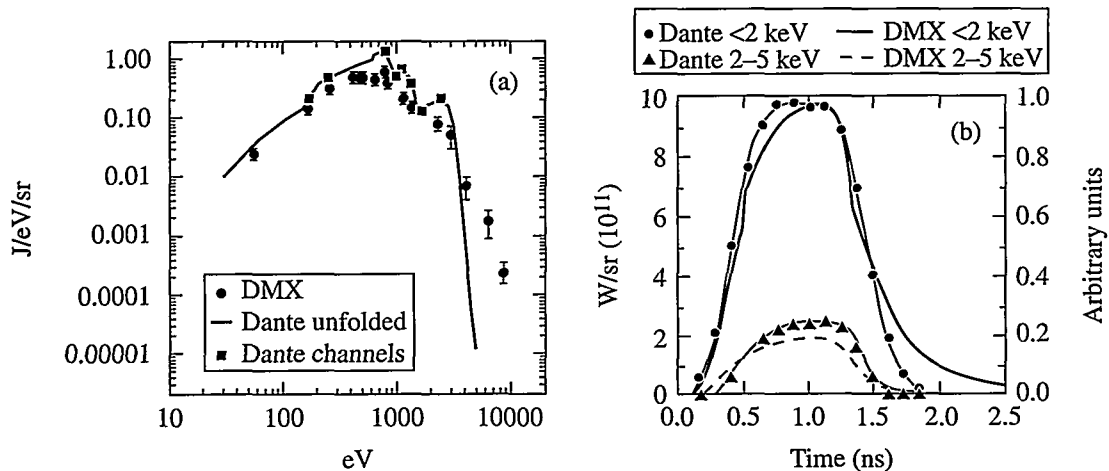
U258

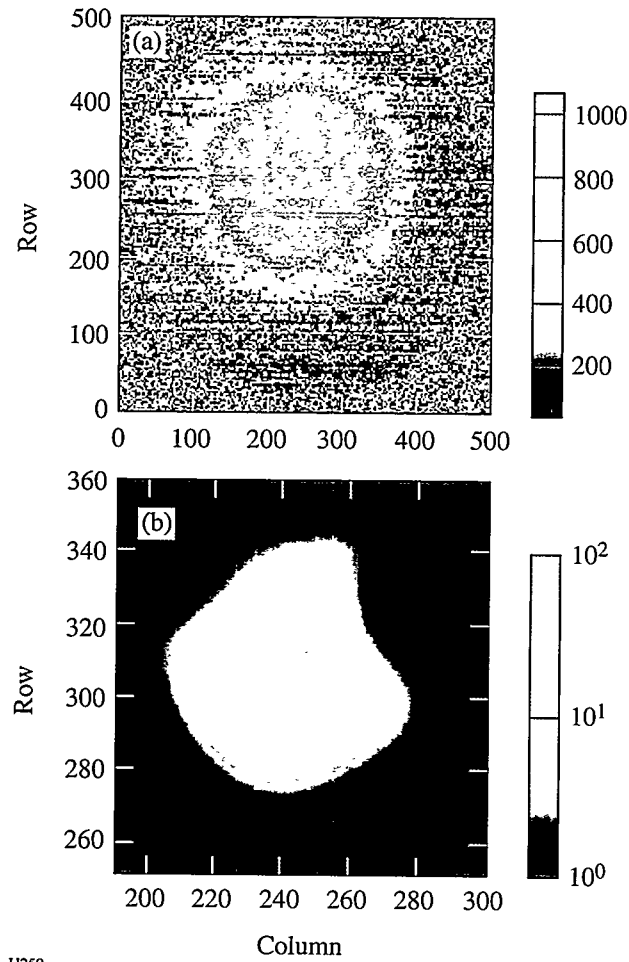Figure 84.64
DMX/Dante experimental results comparison. (a) Time-integrated spectrum inferred from Dante (solid line and squares) and DMX (circles) on OMEGA Shot 18326. Symbols denote the mean energies of the channels for both diagnostics. (b) Spectrally integrated intensity as a function of time for $h\nu < 2$ keV and $2 < h\nu < 5$ keV. DMX data were rescaled with the same factor for both plots.

Figure 84.65

(a) Penumbral image of an imploded DT target. The central disk is the image of the neutrons passing through the entrance of the aperture. The neutron source size information is in the area surrounding the central disk. (b) Processed neutron image of a DT imploded target (Shot 20290). Ten pixels represent 28 μm on this image.

Publications and Conference Presentations

Publications

E. L. Alfonso, I. Anteby, and D. R. Harding, "Temperature Profiles and $\ell = 1$ Nonuniformity Within Cryogenic ICF Targets," Fusion Technol. **38**, 149 (2000).

A. Babushkin, M. J. Guardalben, R. S. Craxton, P. Adamson, H. Ammenheuser, R. L. Keck, and W. Seka, "Characterization of Frequency-Conversion Crystals for the Implementation of a 1-THz Bandwidth on the OMEGA Laser," in *Conference on Lasers and Electro-Optics*, 2000 Technical Digest Series (Optical Society of America, Washington, DC, 2000), pp. 290–291.

T. R. Boehly, D. D. Meyerhofer, Y. Fisher, W. Seka, and D. K. Bradley, "Measurements of the Optical Contrast on OMEGA: a 60-Beam, 30-kJ UV Fusion Laser," in *Conference on Lasers and Electro-Optics*, 2000 Technical Digest Series (Optical Society of America, Washington, DC, 2000), p. 539.

H. P. Chen, D. Katsis, J. C. Mastrangelo, S. H. Chen, S. D. Jacobs, and P. J. Hood, "Glassy Liquid-Crystal Films with Opposite Chirality as High-Performance Optical Notch Filters and Reflectors," Adv. Mat. **12**, 1283 (2000).

H. P. Chen, D. Katsis, J. C. Mastrangelo, K. L. Marshall, S. H. Chen, and T. H. Mourey, "Thermotropic Chiral–Nematic Poly(p-phenylene)s as a Paradigm of Helically Stacked π-Conjugated Systems," Chem. Mater. **12**, 2275 (2000).

F. Y. Fan, J. C. Mastrangelo, D. Katsis, and S. H. Chen, "Novel Glass-Forming Liquid Crystals: V. Nematic and Chiral-Nematic Systems with an Elevated Glass Transition Temperature," Liq. Cryst. **27**, 1239 (2000).

M. J. Guardalben and N. Jain, "Phase-Shift Error as a Result of Molecular Alignment Distortions in a Liquid-Crystal Point-Diffraction Interferometer," Opt. Lett. **25**, 1171 (2000).

S. D. Jacobs, "Take-Home Demo Excites Young People About Careers in Technology," Opt. Photonics News, 16 (July 2000).

S. D. Jacobs and A. B. Shorey, "Magnetorheological Finishing: New Fluids for New Materials," in *Optical Fabrication and Testing*, OSA Technical Digest (Optical Society of America, Washington, DC, 2000), pp. 142–144 (invited).

I. Kozhinova, S. Jacobs, S. Arrasmith, and L. Gregg, "Corrosion in Aqueous Cerium Oxide Magnetorheological Fluids," in *Optical Fabrication and Testing*, OSA Technical Digest (Optical Society of America, Washington, DC, 2000), pp. 151–153.

P. W. McKenty, M. D. Wittman, and V. N. Goncharov, "Characterization of Thick Cryogenic Fuel Layers Using Convergent-Beam Interferometry: a Numerical Investigation," J. Appl. Phys. **88**, 2928 (2000).

A. V. Okishev, R. Boni, M. Millecchia, B. Kubera, P. A. Jaanimagi, W. R. Donaldson, R. L. Keck, W. Seka, K. V. Dukelsky, M. A. Eronyan, G. A. Shevandin, and G. A. Ermolaev, "A Unique High-Bandwidth, Multimode UV Optical Fiber: Manufacturing, Testing, and Laser-Fusion Applications," in *Conference on Lasers and Electro-Optics*, 2000 Technical Digest Series (Optical Society of America, Washington, DC, 2000), pp. 292–293.

J. D. Schnittman and R. S. Craxton, "Three-Dimensional Modeling of Capsule Implosions in OMEGA Tetrahedral Hohlraums," Phys. Plasmas **7**, 2964 (2000).

A. B. Shorey and S. D. Jacobs, "Nanohardness of Abrasive Particles Used in Magnetorheological Finishing (MRF)," in *Optical Fabrication and Testing*, OSA Technical Digest (Optical Society of America, Washington, DC, 2000), pp. 145–147.

M. D. Skeldon, "A High-Bandwidth Electrical Waveform Generator Based on an Aperture-Coupled Stripline," Rev. Sci. Instrum. **71**, 3559 (2000).

R. Sobolewski, "Time-Resolved Nonequilibrium Phenomena in High-Temperature Superconductors," in *Superconductivity, Magneto-Resistive Materials, and Strongly Correlated Quantum Systems*, Recountres du Vietnam, edited by N. Van Hieu, T. Thanh Van, and G. Xiao (Vietnam National University Press, Hanoi, 2000), pp. 55–66 (invited).

F.-Y. Tsai, E. L. Alfonso, S. H. Chen, and D. R. Harding, "Mechanical Properties and Gas Permeability of Polyimide Shells Fabricated by the Vapor Deposition Method," Fusion Technol. **38**, 83 (2000).

B. Yaakobi, V. A. Smalyuk, J. A. Delettrez, F. J. Marshall, D. D. Meyerhofer, and W. Seka, "Measurement of Areal Density Modulation of Laser-Imploded Shells Through K-Edge Imaging," Phys. Plasmas **7**, 3727 (2000).

B. Yaakobi, C. Stoeckl, T. Boehly, D. D. Meyerhofer, and W. Seka, "Measurement of Preheat Due to Fast Electrons in Laser Implosions," Phys. Plasmas. **7**, 3714 (2000).

--- **Forthcoming Publications** ---

S. R. Arrasmith, S. D. Jacobs, I. A. Kozhinova, A. B. Shorey, D. Golini, W. I. Kordonski, S. Hogan, and P. Dumas, "Development and Characterization of Magnetorheological Fluids for Optical Finishing," to be published in the Proceedings of Fine Powder Processing '99, University Park, PA, 20–22 September 1999.

A. Babushkin, M. J. Harvey, and M. D. Skeldon, "The Output Signal-to-Noise Ratio of a Nd:YLF Regenerative Amplifier," to be published in Applied Optics.

R. Betti and J. P. Freidberg, "Low-β, Magnetohydrodynamic Tokamak Equilibria with Poloidal Transonic Flow," to be published in Physical Review Letters.

T. R. Boehly, A. Babushkin, D. K. Bradley, R. S. Craxton, J. A. Delettrez, R. Epstein, T. J. Kessler, J. P. Knauer, R. L. McCrory, P. W. McKenty, D. D. Meyerhofer, S. Regan, W. Seka, S. Skupsky, V. A. Smalyuk, R. P. J. Town, and B. Yaakobi, "Laser-Uniformity and Hydrodynamic-Stability Experiments at the OMEGA Laser Facility," to be published in Laser and Particle Beams.

T. R. Boehly, J. A. Delettrez, J. P. Knaurer, D. D. Meyerhofer, B. Yaakobi, R. P. J. Town, and D. Hoarty, "The Effect of Target Isentrope on the Stability of Laser-Driven Targets," to be published in Physical Review Letters.

T. R. Boehly, Y. Fisher, D. D. Meyerhofer, W. Seka, J. M. Soures, and D. K. Bradley, "The Effect of Optical Prepulse on Direct-Drive Inertial Confinement Fusion Target Performance," to be published in Physics of Plasmas.

T. R. Boehly, V. N. Goncharov, O. Gotchev, J. P. Knauer, D. D. Meyerhofer, D. Oron, S. P. Regan, Y. Srebro, W. Seka, D. Shvarts, S. Skupsky, and V. A. Smalyuk, "The Effect of Plasma Formation Rate and Beam Smoothing on Laser Imprinting," to be published in Physical Review Letters.

B. Buerke and D. D. Meyerhofer, "Accurate Measurement of Hydrogenic Tunneling Rates in a High-Intensity Laser Focus," to be published in Physical Review Letters.

D. P. Butler, Z. Celik-Butler, and R. Sobolewski, "Y-Ba-Cu-O as an Infrared Radiation Sensing Material," to be published in the Handbook of Advanced Electronic and Photonic Materials (Academic Press, NY).

J. A. Frenje, D. G. Hicks, C. K. Li, F. H. Séguin, R. D. Petrasso, K. Fletcher, H. Olliver, S. Padalino, S. Thompson, J. M. Soures, S. Roberts, C. Sorce, T. C. Sangster, and T. W. Phillips, "CR-39 Tract Detector Response to Charged Particles and Neutrons," to be published in the Review of Scientific Instruments.

V. Yu. Glebov, D. D. Meyerhofer, C. Stoeckl, and J. D. Zuegel, "Secondary Neutron Yield Measurements by Current Mode Detectors," to be published in the Review of Scientific Instruments.

W. Göb, W. Liebich, W. Lang, I. Puica, R. Sobolewski, R. Rossler, J. D. Pedarnig, and D. Bauerle, "Double Sign Reversal of the Vortex Hall Effect in $YBa_2Cu_3O_{7-\delta}$ Thin Films in the Strong Pinning Limit of Low Magnetic Fields," to be published in Physical Review B.

G. N. Gol'tsman, O. Okunev, G. Chulkova, A. Dzardanov, A. Lipatov, A. Semenov, K. Smirnov, B. Voronov, G. Chulkova, C. Williams, and R. Sobolewski, "Picosecond Superconducting Single-Photon Optical Detector," to be published in Applied Physics Letters.

V. N. Goncharov, P. W. McKenty, S. Skupsky, R. P. J. Town, R. Betti, and C. Cherfils-Clérouin, "Modeling Hydrodynamic Instabilities in Inertial Confinement Fusion Targets," to be published in Physics of Plasmas.

K. Green and R. Sobolewski, "Extending Scattering Parameter Approach to Characterization of Linear Time-Varying Microwave Devices," to be published in IEEE Transactions on Microwave Theory and Techniques.

P. A. Jaanimagi, R. Boni, and R. L. Keck, "Neutron-Induced Background in CCD Detectors," to be published in the Review of Scientific Instruments.

D. Katsis, H. P. Chen, S. H. Chen, L. J. Rothberg, and T. Tsutsui, "Polarized Photoluminescence from Solid Films of Nematic and Chiral-Nematic Poly(p-phenylene)s," to be published in Applied Physics Letters.

C. K. Li, D. G. Hicks, F. H. Séguin, J. Frenje, R. D. Petrasso, J. M. Soures, P. B. Radha, V. Yu. Glebov, C. Stoeckl, J. P. Knauer, F. J. Marshall, D. D. Meyerhofer, S. Skupsky, S. Roberts, C. Sorce, T. C. Sangster, T. W. Phillips, and M. D. Cable, "Measuring Fusion Yields, Areal Densities, and Ion Temperatures of Imploded Capsules at OMEGA," to be published in the Review of Scientific Instruments.

V. Lobatchev and R. Betti, "Ablative Stabilization of the Deceleration Phase Rayleigh–Taylor Instability," to be published in Physical Review Letters.

F. J. Marshall, T. A. Ohki, D. McInnis, Z. Ninkov, and J. Carbone, "Imaging of Laser-Plasma X-Ray Emission with Charge Injection Devices (CID)," to be published in the Review of Scientific Instruments.

A. V. Okishev, R. Boni, M. Millecchia, P. A. Jaanimagi, W. R. Donaldson, R. L. Keck, W. Seka, K. V. Dukelsky, M. A. Eronyan, V. S. Shevandin, G. A. Ermolaeva, G. Nikolaev, and V. B. Shilov, "Unique High-Bandwidth, UV Fiber Delivery System for the OMEGA Diagnostic Applications," to be published in the IEEE Journal on Selected Topics in Quantum Electronics.

A. V. Okishev, M. D. Skeldon, R. L. Keck, and W. Seka, "A New High-Bandwidth, All Solid-State Pulse-Shaping System for the OMEGA Laser Facility," to be published in SPIE's Proceedings of Laser Optics 2000.

S. P. Regan, J. A. Marozas, J. H. Kelly, T. R. Boehly, W. R. Donaldson, P. A. Jaanimagi, R. L. Keck, T. J. Kessler, D. D. Meyerhofer, W. Seka, S. Skupsky, and V. A. Smalyuk, "Experimental Investigation of Smoothing by Spectral Dispersion," to be published in the Journal of the Optical Society of America B.

F. H. Séguin, C. K. Li, D. G. Hicks, J. A. Frenje, R. D. Petrasso, J. M. Soures, V. Yu. Glebov, C. Stoeckl, P. B. Radha, D. D. Meyerhofer, S. Roberts, C. Sorce, T. C. Sangster, and M. D. Cable, "Diagnostic Use of Secondary $D-^3He$ Proton Spectra for D-D OMEGA Targets," to be published in Physics of Plasmas.

A. B. Shorey, S. D. Jacobs, W. I. Kordonski, and R. F. Gans, "Understanding the Mechanism of Glass Removal in Magnetorheological Finishing (MRF)," to be published in Applied Optics.

A. B. Shorey, K. M. Kwong, K. M. Johnson, and S. D. Jacobs, "Nanoindentation Hardness of Particles Used in Magnetorheological Finishing (MRF)," to be published in Applied Optics.

R. W. Short, "Stability of Self-Focused Filaments in Laser-Produced Plasmas," to be published in Physical Review Letters.

S. Skupsky, R. L. McCrory, R. E. Bahr, T. R. Boehly, T. J. B. Collins, R. S. Craxton, J. A. Delettrez, W. R. Donaldson, R. Epstein, V. N. Goncharov, R. Q. Gram, D. R. Harding, P. A. Jaanimagi, R. L. Keck, J. P. Knauer, S. J. Loucks, F. J. Marshall, P. W. McKenty, D. D. Meyerhofer, S. F. B. Morse, O. V. Gotchev, P. B. Radha, S. P. Regan, W. Seka, V. A. Smalyuk, J. M. Soures, C. Stoeckl, R. P. J. Town, M. D. Wittman, B. Yaakobi, J. D. Zuegel, R. D. Petrasso, D. G. Hicks, and C. K. Li, "Recent Progress in Direct-Drive ICF Research at the Laboratory for Laser Energetics," to be published in SPIE's Proceedings of the XXVI European Conference on Laser Interaction with Matter.

V. A. Smalyuk, T. R. Boehly, L. S. Iwan, T. J. Kessler, J. P. Knauer, F. J. Marshall, D. D. Meyerhofer, C. Stoeckl, B. Yaakobi, and D. K. Bradley, "Fourier-Space Image Processing for Spherical Experiments on OMEGA," to be published in the Review of Scientific Instruments.

V. A. Smalyuk, B. Yaakobi, J. A. Delettrez, F. J. Marshall, and D. D. Meyerhofer, "Compressed-Shell Integrity Measurements in Spherical Implosion Experiments," to be published in Physics of Plasmas.

V. A. Smalyuk, B. Yaakobi, F. J. Marshall, and D. D. Meyerhofer, "X-Ray Spectroscopic Measurements of Areal Density and Modulations in Areal Density of Cold Compressed Shells in Implosion Experiments on OMEGA," to be published in the Proceedings of the 12th Topical Conference on Atomic Processes in Plasmas, Reno, NV, 19–23 March 2000.

D. J. Smith, J. A. Warner, N. E. LeBarron, T. J. Kessler, and S. LaDelia, "The Development of Ion-Etched Phase Plates," to be published in Applied Optics.

C. Stoeckl, V. Yu Glebov, D. D. Meyerhofer, W. Seka, B. Yaakobi, R. P. J. Town, and J. D. Zuegel, "Hard X-Ray Detectors for OMEGA and NIF," to be published in the Review of Scientific Instruments.

F.-Y. Tsai, E. L. Alfonso, S. H. Chen, and D. R. Harding, "Mechanical Properties and Gas Permeability of Polyimide Shells Fabricated by the Vapor Deposition Method," to be published in Fusion Technology.

B. Yaakobi, C. Stoeckl, T. R. Boehly, D. D. Meyerhofer, and W. Seka, "Measurement of Preheat due to Fast Electrons in Laser Implosions," to be published in SPIE's Proceedings of the XXVI European Conference on Laser Interaction with Matter.

J. D. Zuegel and D. W. Jacobs-Perkins, "An Efficient, High-Frequency Bulk Phase Modulator," to be published in Applied Optics.

J. D. Zuegel and S. A. Letzring, "Bulk Microwave Phase Modulators for Smoothing by Spectral Dispersion," to be published in Applied Optics.

Conference Presentations

R. Sobolewski, D. P. Butler, and Z. Celik-Butler, "Cooled and Uncooled Infrared Detectors Based on Yttrium Barium Copper Oxide," SPIE Baltic States Conference on Advanced Optical Materials (ADOM-2), Vilnius, Lithuania, 16–19 August 2000 (invited).

The following presentations were made at the Applied Superconductivity Conference (ASC), Virginia Beach, VA, 17–22 September 2000:

R. Adam, C. Williams, R. Sobolewski, J. Scherbel, M. Darula, and M. Siegel, "Experiments and Simulations of Subpicosecond SFQ Pulse Propagation in Y-Ba-Cu-O Josephson Transmission Lines."

G. Gol'tsman, O. Okunev, G. Chulkova, A. Lipatov, A. Dzardanov, K. Smirnov, A. Semenov, B. Voronov, C. Williams, and R. Sobolewski, "Fabrication and Properties of an Ultrafast NbN Hot-Electron Single-Photon Detector."

R. Sobolewski and J.-R. Park, "Magneto-Optical Modulator for Superconducting Digital Output Interface."

C. Williams, R. Adam, Y. Xu, R. Sobolewski, J. Scherbel, O. Harnack, M. Darula, and F. A. Hegmann, "Ultrafast Y-Ba-Cu-O Photodetector Based on the Nonequilibrium Kinetic Inductive Effect."